RICE UNIVERSITY

Optimization of Novel Developments in Positron Emission Tomography (PET) Imaging

by

Tingting Chang

A THESIS SUBMITTED
IN PARTIAL FULFILLMENT OF THE
REQUIREMENTS FOR THE DEGREE

Doctor of Philosophy

APPROVED, THESIS COMMITTEE:

John W. Clark, Jr., Professor, Chair
Electrical and Computer Engineering

Kevin F. Kelly, Associate Professor
Electrical and Computer Engineering

Jeffrey G. Jacot, Assistant Professor
Bioengineering

Osama R. Mawlawi, Professor
Imaging Physics, The University of Texas
M.D. Anderson Cancer Center

HOUSTON, TEXAS
APR 2012

ABSTRACT

Optimization of Novel Developments in
Positron Emission Tomography (PET) Imaging

by

Tingting Chang

Positron Emission Tomography (PET) is a widely used imaging modality for diagnosing patients with cancer. Recently, there have been three novel developments in PET imaging aiming to increase PET image quality and quantification. This thesis focuses on the optimization of PET image quality on these three developments.

The first development is the fully 3D PET data acquisition and reconstruction. 3D Acquisitions are not constrained in collecting events in single 2D planes and can span across different planes. 3D acquisition provides better detection since it can accept more events. Also it can result in lower radiation dose to the patient and shorter imaging times. With the application of 3D acquisition, a fully 3D iterative reconstruction algorithm was also developed. The aim of the first project in this thesis is to evaluate the PET image and raw data quality when this fully 3D iterative reconstruction algorithm is applied.

The second development in PET imaging is the time-of-flight (TOF) PET data acquisition and reconstruction. TOF imaging has the ability to measure the difference between the detection times, thus localize the event location more accurately to increase the image quality. The second project in this thesis focuses on optimizing the TOF reconstruction parameters on a newly developed TOF PET scanner. Then the

improvement of TOF information on image quality is assessed using the derived optimal parameters. Finally the effect of scan duration is evaluated to determine whether similar image quality could be obtained between TOF and non-TOF while using less scan time for TOF.

The third development is the interest in building PET / magnetic resonance (MR) multi-modality scanner. MR imaging has the ability to show high soft tissue contrast and can assess physiological processes, which cannot be achieved on PET images. One problem in developing PET/MR system is that it is not possible with current MR acquisition schemes to translate the MR image into an attenuation map to correct for PET attenuations. The third project in this thesis proposed and assessed an approach for the attenuation correction of PET data in potential PET/MR systems to improve PET image quality and quantification.

Acknowledgements:

I would like to thank Dr. John W. Clark, a good advisor at Rice University, for introducing me into the field of biomedical imaging, for helping me understand the advances of this field, for recommending me to a hospital environment to conduct my Ph.D. research.

Thanks to Dr. Osama R. Mawlawi to be a great advisor and friend at the same time, for giving me an opportunity to conduct my research work in MD Anderson Cancer Center, for offering me great hands-on experience in various medical imaging modalities, for helping me in my research whenever I encountered difficulties.

Thanks to all the lab staff in ECE@RICE and DI@MDACC, to help me with various problems I faced in the process of this Ph.D. research work.

Content

List of Tables

List of Figures

Chapter 1

Introduction to Positron Emission Tomography (PET)

Positron emission tomography (PET) is a diagnostic imaging technique that can measure the metabolic activity in the human body. First utilized in clinical diagnosis in the early 1990s, it is often used to produce functional images of certain structures including the brain, heart, lung, liver and kidney. Functional images (figure 1.1(a)) generated from PET differ from anatomical or structural images (figure 1.1(b)) such as those generated by X-ray computed tomography (CT), in that they have the ability to reveal biochemical processes within the human body, such as blood flow, receptor density and glucose metabolism. In PET imaging, radioactivity is first attached or tagged to a radioactive material that is intrinsic to the human body (e.g. glucose, water, and ammonia). When a solution containing the radioactive substance is administered to the patient via injection, PET imaging can be used to map both normal and abnormal tissue function. More specifically, a specially designed PET scanner can be used to monitor how the body processes this radioactive material and generates the associated distributed and accumulated images. Frequently the radioactive material used is ^{18}F labeled fluro-deoxy-glucose (FDG), a 'glucose analog' that accumulates in regions having high metabolic activity such as brain, liver and malignant tumors (figure 1.1(a)). Accumulation of ^{18}F-FDG by the tissue is directly related to its metabolic activity. Hence, an abnormal increase in uptake would indicate the presence of malignant tumor cells. Usually the biologic and metabolic activities of disease precede any anatomic evidence of illness. Consequently, PET is an important technique for the diagnosis and staging of

malignant disease and increasingly it is being employed in monitoring a patient's response to cancer therapy.

In summary, PET imaging can be used to non-invasively detect functional changes in vivo with high sensitivity and specificity (*1*). It can also be used to quantify the amount of radioactivity in the human body, which is particularly important in the diagnosis, staging, and evaluation of treatment response. These advantages have enabled wide acceptance of PET imaging as a diagnostic and a research tool, with applications in oncology (*2,3*), neurology (*4*), cardiology (*5*), and pharmacology (*6*).

This chapter provides a brief introduction to the fundamentals of PET imaging, including the processes of PET data acquisition and image reconstruction. A brief

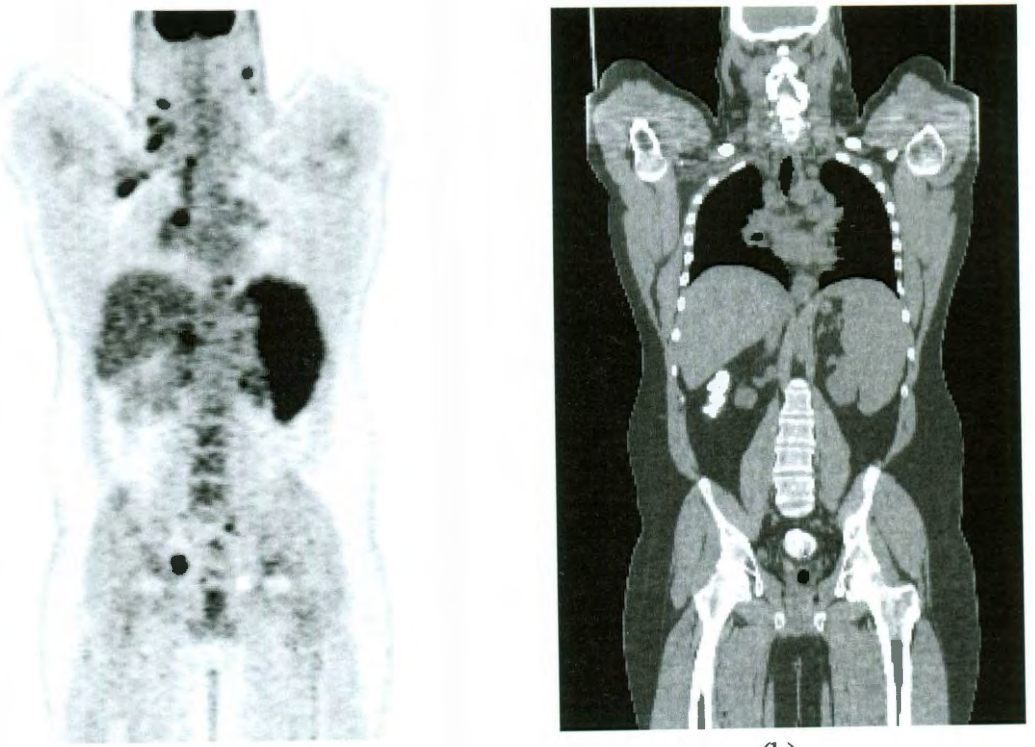

(a) (b)

Figure 1.1: Illustration of (a) PET image and (b) CT image

discussion of computed tomography (CT) imaging principles is included, as well as a discussion of combined PET/CT imaging. These modalities are complementary in the sense that CT yields anatomical information on the location of boundaries, organs and targets, whereas PET images contain information on tissue function. This chapter ends with an introduction to those characteristics of PET imaging that relate to the central topics of this dissertation.

1.1 PET Data Acquisitions

A PET imaging requires the patient to be injected with radioactive materials that are labeled with positron emitting radio-nuclides. The most commonly used nuclides are ^{18}F, ^{15}O, ^{13}N and ^{11}C, which all represent the most abundant elements in the human body. These positron-emitting nuclides can be used to label many radio-pharmaceutical compounds such as ^{11}CO, ^{13}NH3, ^{15}O-labeled water and ^{18}F-FDG. All of these radioactive labels decay by emitting positron, which is the anti-particle of electron. For example, if the radio-pharmaceutical compound is ^{18}F-FDG, the decay equation is

$$^{18}F \rightarrow {}^{18}O + \beta^{+} + \upsilon \tag{1.1}$$

where β^{+} represents the emitted positron and ν represents a neutrino. The emitted positron rapidly interacts with an electron (β^{-}) from the surrounding tissue

$$\beta^{+} + \beta^{-} \rightarrow 2\gamma \tag{1.2}$$

The mass of both particles is converted by annihilation into two gamma photons (2γ), following Einstein's mass-energy equation $E = mc^2$. According to this equation, each gamma photon from this positron electron annihilation has an energy of 511 keV, and the

two gamma photons are emitted in opposite directions due to the conservation of momentum.

A PET scanner has a ring of detectors that is capable of detecting gamma rays generated inside the human body. The principle of PET imaging is illustrated in figure 1.2. When annihilation between positron and electron occurs, two gamma photons are generated and emitted simultaneously in opposite directions, hitting two detectors within

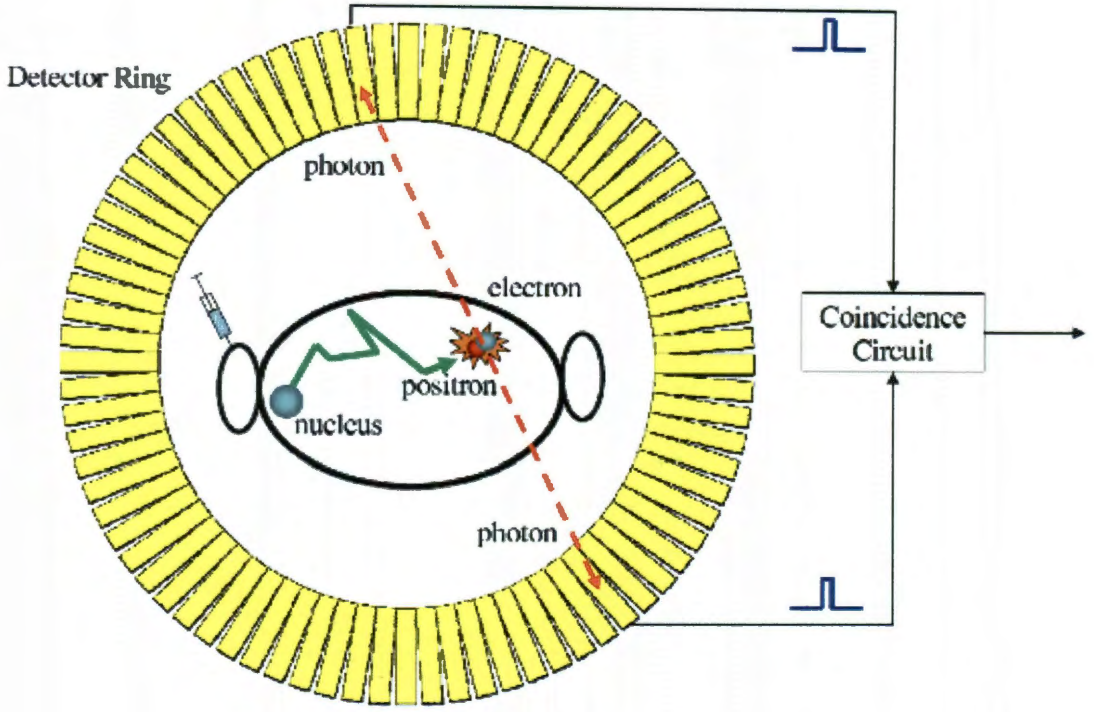

Figure 1.2: Fundamental of PET imaging

a time frame of several nanoseconds. Consequently, two detections made within such timing window are viewed as a 'coincidence event' resulting from this annihilation process. The line connecting the two detectors is recorded as line-of-response (LOR), which indicates that the annihilation occurred somewhere along this line. As the scanning

process continues, additional gamma rays emit, and a lot of coincidence events occur along each possible LOR. The system sorts the collected coincidence events into a histogram (usually called a sinogram) according to their locations (e.g., radial distance and view angle in 2-D mode as shown in figure 1.3), or stored on an event-by-event basis known as a List-Mode acquisition. During each PET scan, the total number of

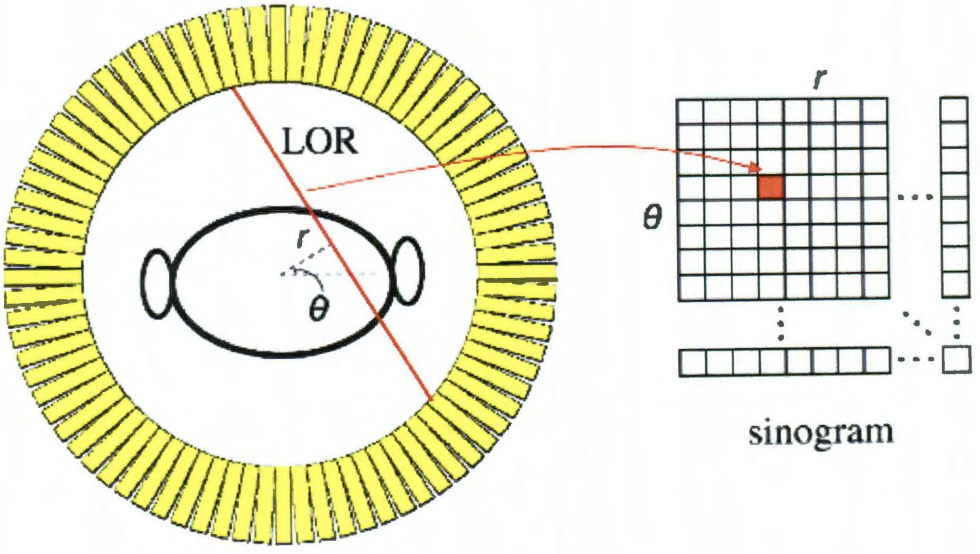

Figure 1.3: Mapping relationship between LOR and sinogram data in 2-D mode

coincidence detected along a specific LOR can be considered proportional to the line integration over the radioactivity distribution along that LOR. Therefore, the sinogram constitutes a Radon transform of the original radioactivity distribution (7), which is formulated as:

$$g(r,\theta) = \int_{-\infty}^{+\infty} \int_{-\infty}^{+\infty} g(x,y)\delta(r - x\cos\theta - y\sin\theta)dxdy \qquad (1.3)$$

where the Randon transform $g(r,\theta)$ is the line integration of the image $g(x,y)$ specified by the line parameters (r,θ), where r is the distance from the center of the field of view (FOV) to the specific line and θ is the pitch angle of the line.

1.2 PET Image Reconstruction

PET image reconstruction is an inverse problem associated with PET data acquisitions. It provides an estimate of the original object via an analysis of the acquired image data. In the early days of PET scanning, a filtered back-projection (FBP) algorithm had widespread use in image reconstruction (*8*). Using this technique, an image of the distribution of the radio-activities within the body to be formed from collected sinogram data. A fundamental assumption of the FBP technique is that sinogram data can be modeled as a Radon transform of the original image (equation 1.3). Specifically,

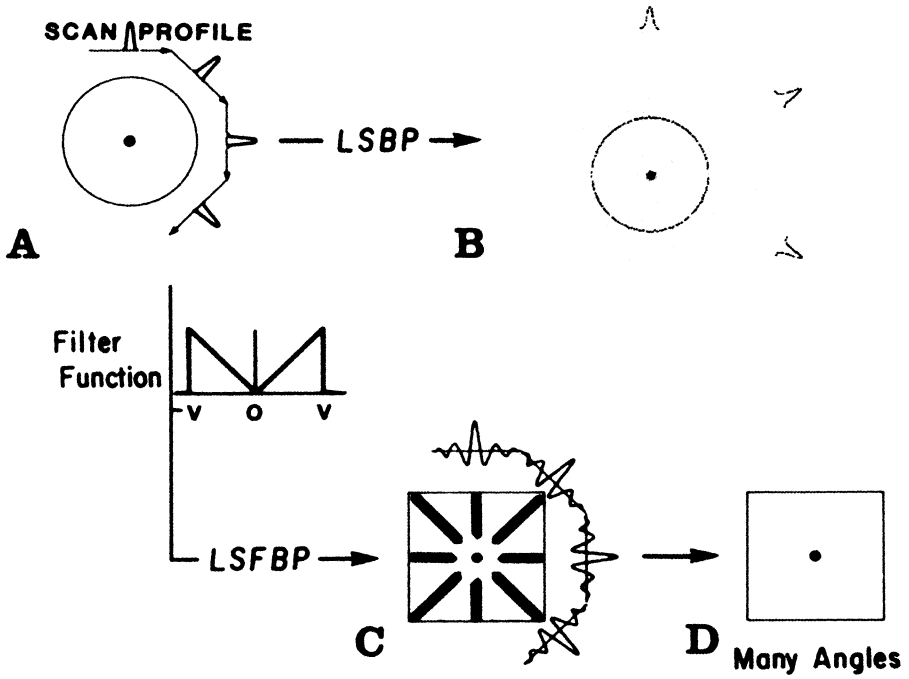

Figure 1.4: Filtered back-projection (FBP) reconstruction for PET imaging

sinogram data collected at each angle are first passed through a selective filter and then back-projected to the original image space (figure 1.4). The greater the number of angles projected, the greater the degree to which the reconstructed image represents the original object. The FBP reconstruction algorithm performs well in a noiseless image acquisition environment, but is severely degraded in the presence of noisier imaging conditions. Such a result stems from the fact that FBP model of the photon detection process is simplistic and does not account for a variety of physical processes involved in the detection process.

More recently, statistical image reconstruction techniques rather than FBP have been shown to provide more accurate system models of the photon detection process and result in much better images after reconstruction (*9-11*). In these statistical approaches, the PET imaging system is modeled as a discrete system (*12*) described by the following expectation function:

$$E\{y_n\} = \sum_{n=1}^{N} H_{nm} x_m + r_n \tag{1.4}$$

Here vector elements $\{y_n\}$ represent the sinogram data vector elements acquired by the PET scanner, whereas the vector elements x_m characterize the true patient image and specifically the amount of radioactivity inside each pixel or voxel (3-D pixel) of the model. The vector elements r_n correspond to noisy background incidents, including random and scatter coincidences which will be discussed later. Usually, r_n is usually modeled as a Poisson noise distribution due to the statistical nature of PET imaging. Matrix H is called the system matrix, whose elements H_{nm} are proportional to the probability that a photon pair originating at voxel m can be detected along the *n-th* LOR. Such design for the system matrix H facilitates the incorporation of the modeling details,

such as physical processes of positron range, non-collinearity, attenuation correction, detector efficiency normalization and depth of interaction. Integrating such physical detail into the system matrix description produces a model that can better reflect the true photon detection probability (*13,14*).

Statistical image reconstruction is generally framed as an optimization problem, whereby an objective function is introduced to relate image estimation quality to measured data. A general solution for this problem is based on the maximum likelihood (ML) technique, in which an optimal image is modeled to be the one that maximizes the probability of making a detection of the data that are actually measured:

$$X' = \arg\max_{X} P(Y \mid X) \tag{1.5}$$

Here Y and X are the sinogram and image vectors, respectively, and $P(\ )$ is the Poisson likelihood function. However, ML-based image reconstruction is an ill-conditioned problem, in that small changes in the data can cause large variations in the reconstructed image (*15*). Another characteristic of ML-based image reconstruction is that as the ML algorithm approaches high iteration numbers, the reconstructed image becomes increasingly noisy. Hence, optimization of the ML objective function is usually terminated before convergence is reached. In addition, smoothing filters are usually applied to the image during or after the optimization process to suppress image noise.

To solve the image reconstruction problem for ML approach, iterative techniques are often applied. The most frequently used iterative technique is the expectation maximization (EM) algorithm (*16*), which has the important advantage that it has a closed-form updating solution:

$$x_m^{(p+1)} = \frac{x_m^{(p)}}{\sum_i H_{ij}} \sum_i H_{ij} \frac{y_i}{\sum_j H_{ij} x_j^{(p)} + r_i} \tag{1.6}$$

Here, $x^{(p)}{}_m$ is the value of image voxel m after the *p-th* iterations. *H, r,* and *y* are the same as those in equation 1.4. A major drawback of the ML-EM algorithm, however, is its slow convergence. Therefore, evolved EM algorithm based on the concept of subsets has been developed to accelerate the optimization process (*17-19*). Each EM iteration is divided into a number of sub-iterations, and each sub-iteration only reconstructs a subset of the whole acquired data (sinogram). The resultant image from one sub-iteration is then updated by the next sub-iteration. This evolutionary set modification of the EM algorithm is called the Ordered-Subset Expectation Maximization (OSEM) algorithm (*17-19*). It performs much faster than ML-EM algorithm while achieving similar image quality; this algorithm is applied currently in most commercial PET scanners.

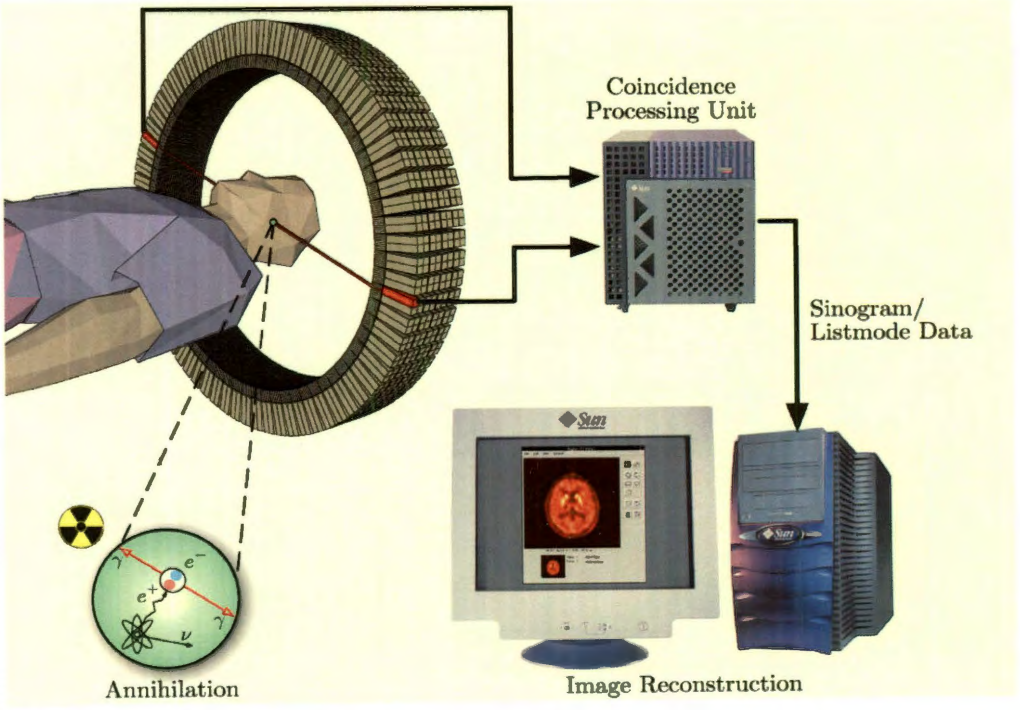

Figure 1.5: The process of PET imaging

Upon completion of the image reconstruction process, PET images are displayed on workstations and physicians can evaluate and diagnose patients' tumors based on ^{18}F-FDG concentration. The whole process of PET imaging, including data acquisition, data storage, image reconstruction and display, is summarized in figure 1.5.

1.3 CT Imaging Principles

CT imaging is a transmission imaging modality, which differs from emission PET imaging. CT acquisition measures transmission X-rays through the human body. Transmitted X-rays are received by detector arrays. The purpose of the CT scanner is to acquire a large number of transmission measurements through the human body at different positions. Figure 1.6 shows the process of a CT scan. The source X-ray transmits through the human body. Each ray transmits and attenuates through the body along a line, where the detector measures an X-ray intensity, I_t. The unattenuated

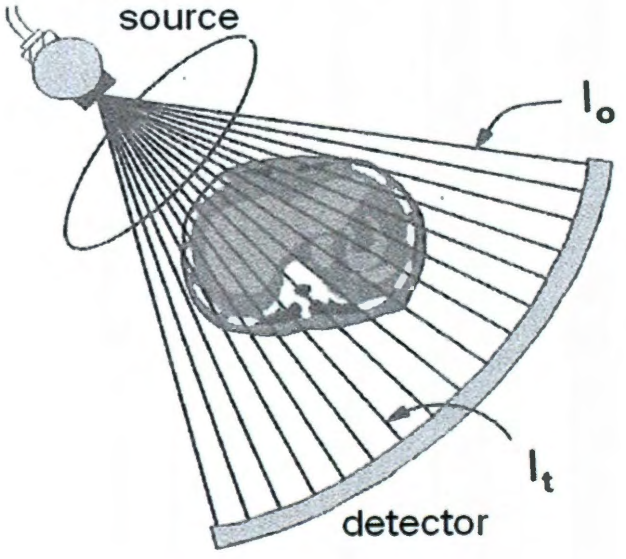

Figure 1.6: CT X-ray source and detector

intensity of the X-ray beam is also measured during the scan by a reference detector, and the intensity is I_0. The relationship between I_t and I_0 is given by the following equation:

$$I_t = I_0 e^{-\mu t} \tag{1.7}$$

where t is the thickness of the body along the ray and μ is the average linear attenuation coefficient along the ray. The product μt in equation 1.7 is an important parameter relating to the anatomy of the body along a given ray that can be easily calculated with knowledge of the measured values I_t and I_0 as:

$$\mu t = \ln(I_0 / I_t) \tag{1.8}$$

Thus, after first preprocessing the CT raw data, the value μ for each ray at each position is calculated and used in the CT reconstruction algorithm for the generation of a CT image. Numerous reconstruction algorithms have been developed for CT imaging, but FBP reconstruction is most widely used scheme employed in clinical CT scanners (*20*). In FBP reconstruction, the back-projection method builds up the CT image in the computer by essentially reversing the acquisition steps, similar to FBP applied in PET imaging (figure 1.4). Attenuation information along a known path of the narrow X-ray beam is integrated by a detector during CT acquisition. During FBP reconstruction, the μ value for each ray is smeared along this same path in the image of the patient. As the data from a large number of rays are back-projected onto the image matrix, areas of high attenuation tend to reinforce each other, and areas of low attenuation also reinforce, thus building up the final CT image.

After CT reconstruction, each pixel in the image is represented by a high-precision floating point number that is useful for computation but less useful for display. Most computer display hardware makes use of integer images and CT images are

normalized and truncated to integer values before storing and displaying. The pixel value in final CT image, *CT(x,y),* for location *(x,y)* (assuming 2D image) is converted using the following expression:

$$CT(x,y) = 1000\frac{\mu(x,y) - \mu_{water}}{\mu_{water}} \tag{1.9}$$

where $\mu(x,y)$ is the floating point number of the *(x,y)* pixel before conversion, μ_{water} is the attenuation coefficient of water, and *CT(x,y)* is the CT number (Hounsfield unit) that is displayed in the final CT image. The value of μ_{water} is about 0.195 for the X-ray beam energies typically used in CT scanning. This conversion results in CT numbers ranging from -1000 to +3000. Here, a value of -1000 corresponds to air; soft tissues range from -300 to -100; water is 0; and dense bone and areas filled with contrast agent have values up to +3000.

CT numbers are quantitative and lead to more accurate diagnosis in some clinical settings. For example, pulmonary nodules that are calcified are typically benign, and the amount of calcification can be determined from the CT image based on the mean CT number of the nodule. Measuring the CT number of a single pulmonary nodule is therefore common practice, and it is an important part of the diagnostic work-up. CT scanners measure bone density with good accuracy, and when phantoms are placed in the scan field along with the patient, quantitative CT techniques can be used to estimate bone density, which is useful to assess fracture risk. CT is also quantitative in terms of linear dimensions, and therefore it can be used to accurately assess tumor volume or lesion diameter.

1.4 PET/CT Multi-modality Imaging

PET imaging has great advantages as a functional imaging modality, however, it has limitations especially when dealing with anatomy such as lesion localization and tumor volume measurement. This limitation is due to its relatively low image resolution and high image noise level when compared to other anatomical imaging modalities such as CT. In this regard, functional images provided by PET and anatomical images provided by CT are usually presented together to facilitate both diagnosis and treatment planning.

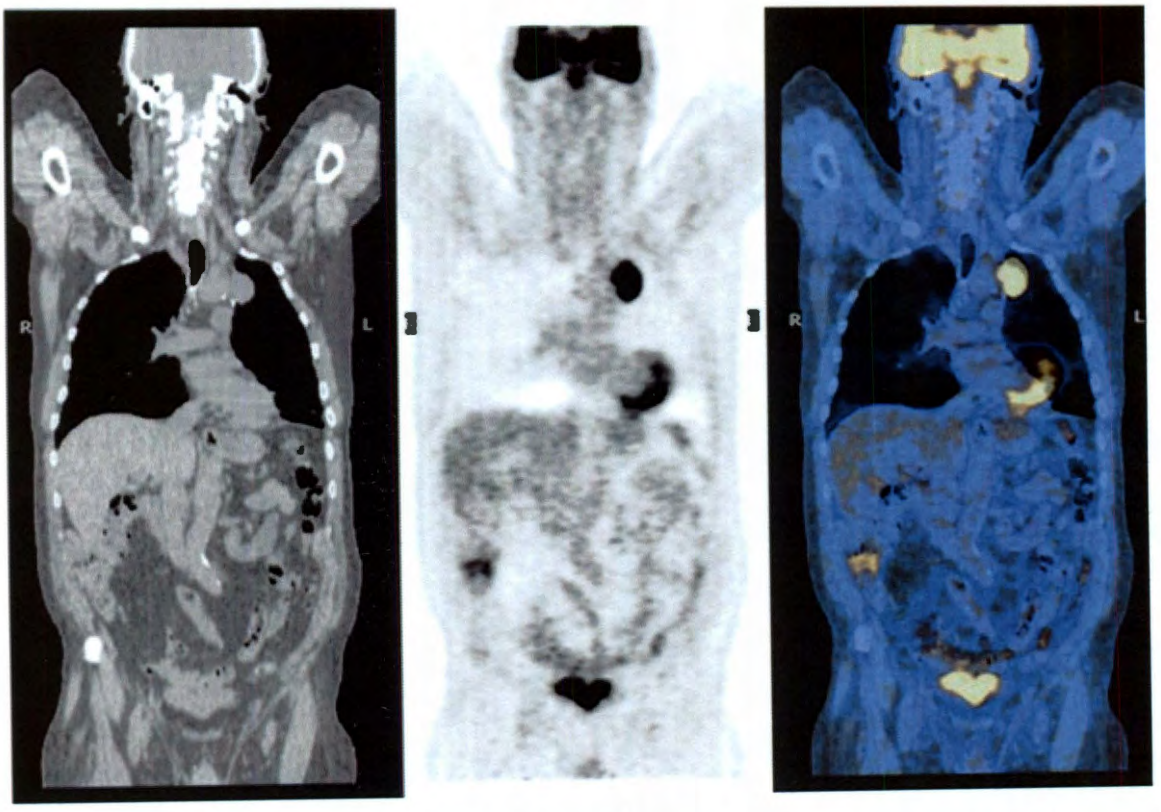

(a) (b) (c)

Figure 1.7: Images for the same patient.
(a) CT, (b) PET, (c) Fused PET/CT

Figure 1.7 shows an example of the PET/CT image, where the PET image, CT image and fused PET/CT image are displayed side by side for comparison. An important assumption associated with the fused PET/CT image is that the PET image is properly registered (aligned) with the CT image, so that a lesion identified in the PET image can be accurately localized on the CT image. If however, the PET and CT acquisitions are scanned separately (e.g., the patient needs to be transported between different scanners), a change in the external pose as well as internal organ displacement could occur between the two imaging procedures. Consequently, an extra image registration process is often required to accurately align the images acquired from different imaging sessions (*21*). This adds to the complexity of the imaging procedure and also reduces the reliability of the overall approach. To resolve this difficulty, combined PET/CT scanners have been developed, where the PET scanner is integrated with a CT scanner. Hence, the patient can receive both PET and CT scans within the same imaging session, without any transportation between different scanners (figure 1.8). An important advantage that accrues with the hybrid PET/CT scanner is that a CT scan can measure the photon attenuation of the object being imaged. Such information from the hybrid scanner can be used in the generation of an attenuation correction map, which can be used directly in PET image reconstruction. There is therefore no need to acquire a separate transmission scan for attenuation correction in the individual PET scanner (*22*). In addition, CT images are characterized by shorter acquisition time and lower noise content than transmission images. Consequently, the brief duration of CT scans significantly shortens the time to scan a patient in a PET/CT scanner. This also shortens the time a patient must remain still, reduces patient discomfort, and lessens the likelihood of patient motion. Finally, CT

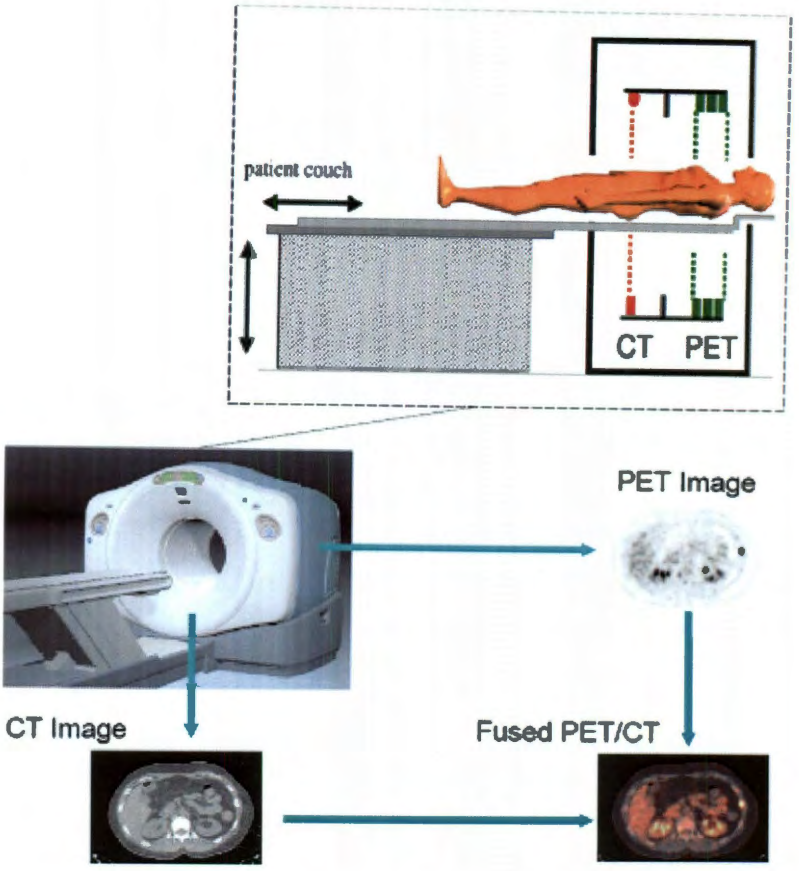

Figure 1.8: An illustration of the PET/CT scanner

images provide high-resolution anatomical information, which, when combined with PET images, can significantly improve diagnostic accuracy and patient management (*23-28*).

Patient scheduling and radiation treatment planning are additional clinical areas that benefit from PET/CT. Most patients who are scheduled for an individual PET scan also receive a diagnostic CT scan prior or after their PET imaging session (*29*). These separate scans could be performed on the same PET/CT scanner in one extended session, thus facilitating patient scheduling and eliminating the need for transportation of the patient from one imaging suite to another. Patient waiting time would be reduced and

throughput would improve. For radiation treatment planning, it has been shown that incorporating PET data into treatment planning along with CT has the potential to improve the accuracy of delineating the lesion target volume (*30-32*). Obtaining the PET and the CT data as a registered data set greatly facilitates using the PET data in planning the treatment.

Nowadays, individual PET scanners are rarely made by major medical imaging equipment manufacturers, while integrated PET/CT scanners are usually supplied. The success of PET/CT multi-modality scanners has motivated the exploration of other integrated imaging techniques, including single photon emission computed tomography (SPECT) / CT imaging (*33*) and PET / magnetic resonance (MR) imaging (*34*).

1.5 PET/CT 3D Image Visualization

PET/CT images that consist of a 3-D volume are usually displayed in three conventional 2D views: transaxial, coronal and sagittal (*35*), as shown in figure 1.9. A transaxial plane divides the body into cranial and caudal (head and tail) portions, while a coronal plane divides the body into dorsal and ventral (back and front) portions. Finally, a sagittal plane divides the body into sinister and dexter (left and right) portions. All three views are often displayed simultaneously on the screen. A cursor within the three images that passes through the same point is also displayed. As the cursor is moved, the transaxial, coronal, and sagittal images are updated to the proper slice in order to show the point. This is an efficient way of navigating through a large 3-D dataset. On the other hand, the dataset can be re-sliced at an arbitrary orientation to provide oblique views.

This is useful for objects whose line of symmetry does not fall naturally along one of the perpendicular axes of the 3-D volume.

(a) (b) (c)

Figure 1.9: Three views of PET image: (a) coronal; (b) transaxial and (c) sagittal

1.6 PET Scanner Detectors

The detector material used in a PET scanner is an important factor influencing its sensitivity and performance. The relatively high energy (511 keV) of the annihilation photons in PET scan result in dense high-Z scintillation detectors (*36,37*). These detectors are arranged in rings around the scanned object (figure 1.5). The PET system not only provides high detection efficiency but also allow the simultaneous collection of data for all projection angles utilizing a completely stationary set of detectors.

Currently most PET scanners utilize scintillation crystals coupled to photomultiplier tubes (PMTs) as detectors (*38,39*). The signals from the PMTs are processed using pulse mode to create signals that identifying the position, deposited energy, and time of each interaction. In early PET scanners, each scintillation crystal was coupled to a single PMT, which was costly and impractical to pack smaller PMTs into each detector ring. Modern designs couple larger crystals to more than one PMT (figure 1.10). The relative magnitudes of the PMT signals coupled to a single crystal are used to determine the position of the interaction in the crystal, as in a scintillation camera (*40*).

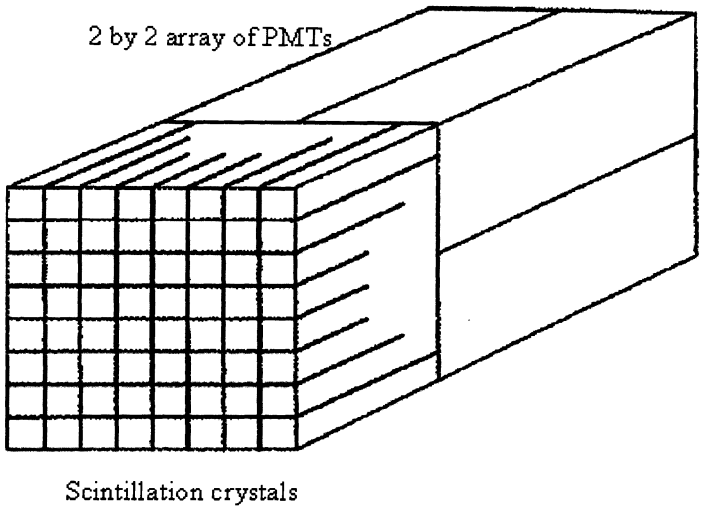

Figure 1.10: Design of PET detectors: scintillator coupled to PMTs

Each detector material has a characteristic dead time that corresponds to the time required to process individual detected events. If a second pulse occurs before the first has been processed completely, the two pulses will overlap to form a single distorted pulse. Overlapped pulse amplitudes may fall outside the pre-selected window of analysis,

reconstruction cases. Finally, examine the effect of scan duration on image quality. In particular determine whether similar image quality can be obtained between TOF and non-TOF scans, while using less scan time for the TOF scan.

Third Area: PET/MR Multi-modality Imaging

PET/CT combined scanner has been proved to be a very powerful diagnostic tool. On the other hand, MR imaging shows the advantages over CT because of its high soft tissue contrast and its ability to assess functional parameters and physiological processes (e.g. heart function, blood flow or diffusion and perfusion) without the application of X-ray radiation. Thus, the combination of PET with MR imaging is contemplated as the next step in the evolution of hybrid imaging. In addition, PET/MR has the advantage of simultaneous acquisition of the two modalities as compared to the contemporaneous, but sequential imaging process in PET/CT. This latter advantage has specific utility for brain imaging when conducting challenge studies where the stimuli and the processes being studied are dynamic. However, the technical challenges of PET/MR include the lack of photon attenuation information with which to correct the PET data, nonuniformity of the MR FOV, truncation artifacts due to differences in the FOV size between the PET and MR, susceptibility artifacts in MR, detecting photons in the presence of a strong magnetic field, and most importantly a clinical application that specifically would benefit from a hybrid PET/MR as opposed to PET/CT.

CT images produced in PET/CT scan has the ability to correct for attenuation in the resultant PET images. MR imaging however gives no direct indication of the amount of gamma photon attenuation because the MR signal intensity is mainly related to the

resulting in a loss of valid events. Such losses are called dead time losses. Scintillation systems usually have dead times in the order of 0.1-1μsec.

The scintillation material should emit light promptly to distinguish true coincident interactions from random coincidences and to minimize dead-time count losses at high interaction rates. In this regard, the detector material must have a high attenuation coefficient for 511 keV photons. Currently most PET systems use crystals of bismuth germinate ($Bi_4Ge_3O_{12}$, abbreviated BGO) (*41,42*). Its great density and average atomic number result in a high efficiency in detecting 511 keV annihilation photons (*43*). However light is emitted rather slowly from BGO (decay constant of 300 nsec), which contributes to dead-time count losses and random coincidences at high interaction rates. Several new scintillators are being investigated as possible replacements for BGO. Three of the most promising scintillators are lutetium oxyorthosilicate (Lu_2SiO_5, abbreviated LSO) (*44*), lutetium yttrium orthosilicate ($Lu_{1.8}Y_{0.2}SiO_5$, abbreviated LYSO) (*45,46*), and gadolinium oxyorthosilicate (Gd_2SiO_5, abbreviated GSO) (*47*). Their attenuation properties are nearly as good as those of BGO and their much faster light emission produces better performance at high interaction rates, especially in reducing dead-time effects and in discriminating between true and random coincidences. Their higher conversion efficiencies may produce improved intrinsic spatial resolution and scatter rejection. The properties of BGO, LSO, LYSO, and GSO are shown in table 1.1.

proton density, whereas the gamma photon attenuation is mainly determined by the density of electrons. Consequently, it is not possible with current MR acquisition schemes to translate the MR image into a PET attenuation map, as it is done with CT images.

Many groups have been investigating the problem of attenuation correction in potential PET/MR system and it is the key issue in PET/MR development. Currently several techniques have been proposed to rely on the use of the MR to either segment MR image into different tissue types and assign corresponding attenuation coefficients, or to use representative anatomical atlas registration to yield an attenuation map (*71-73*). Nevertheless, MR-guided attenuation correction still remains challenging for whole-body imaging, which includes attenuation of MR hardware, positioning aids in the field-of-view (FOV), and truncation in the transverse plane owing to the limited size of the MR FOV.

The aim of the third project is to investigate the feasibility of using the non-attenuated PET images (PET-NAC) as a means for the AC of PET data in the PET/MR systems. An iterative segmentation approach has been proposed and assessed in this project, which could segment PET-NAC into three tissue types (background air, soft tissue, and lung). Then predefined attenuation coefficients were assigned for each tissue type to create an attenuation map for PET reconstruction. Such an approach can potentially be an alternative method of MR-based AC in PET/MR imaging.

Table 1.1: Properties of several scintillators used in PET scanners

Material	Density	Atomic Number (Z)	Attenuation coefficient 511 keV (cm^{-1})	Photo Fraction (%)	Light Output (phtons/MeV)	Decay Time (nsec)	λ (nm)	Energy Resolution (% FWHM)
BGO	7.1	75	0.95	40	9000	300	480	12
GSO	6.7	59	0.70	25	8000	60	440	9
LSO	7.4	66	0.88	32	30000	40	420	10
LYSO	7.1	65	0.83	30	29000	42	420	10

* Data from (*48,49*)

1.7 PET Counting Efficiency

Although PET imaging has been widely used for tumor diagnosis and staging, this imaging modality suffers from a relatively low image quality with respect to other modalities such as CT (figure 1.1). This is mainly due to the high noise content, which is caused by the relatively low counting efficiency of the scanner as well as the acquisition of scatter and random coincidences during the imaging process.

Chapter 2

Reliability of Predicting Image Signal-to-noise Ratio Using Noise Equivalent Count Rate in PET Imaging

2.1 Background and Motivation

PET imaging with fluorine-18 fluorodeoxyglucose (^{18}F-FDG) is widely used in clinical oncology to facilitate patient diagnosis in a wide variety of cancers (*74-76*). However, this modality has been characterized by relatively low image quality (*77*) particularly due to its low sensitivity and the acquisition of random and scatter coincidences during the imaging process. To assess the image quality of PET scanners, the metric noise equivalent count rate (NECR) has been proposed (*78*). The NECR is determined from the PET raw emission data, and is used as a good indicator of the image quality because it takes into account the effects introduced by scatter and random coincidences (*78-80*).

Several groups have investigated the behavior of NECR while using various acquisition parameters, with the goal of obtaining the optimal value of each parameter to achieve the highest NECR. Badawi et al. (*81*) attempted to optimize the NECR for different phantom sizes, activity in the field of view, lower energy discriminator level, and acquisition mode. Surti et al. (*82*) evaluated the impact of phantom diameter and scanner type on the NECR. The effect of injected dose on NECR was also evaluated by several other groups (*83-85*) to optimize the injected dose for patients of different weight or body mass index (BMI). In all these studies (*81-85*), the authors optimized the statistical quality of the data by maximizing the NECR. However, the NECR is a metric

that represents PET raw emission data and, therefore, may introduce potential bias when correlated to the quality of reconstructed images, since the NECR does not account for the normalization, attenuation correction, and reconstruction algorithm of the system.

The signal-to-noise ratio (SNR) is another widely accepted metric that characterizes PET image quality. SNR is derived from *image* statistics rather than *raw* data which are needed for NECR calculation. SNR reflects the relative signal level with respect to the noise of the reconstructed image and, thereby, the ability of PET to detect tumors (*86-88*). Watson et al. (*89*) showed that the square of the SNR is linearly proportional to the NECR in filtered back-projection (FBP) reconstruction. Dahlbom et al. (*90*) then showed a similar relationship when using Fourier rebinned ordered-subset expectation maximization (FORE-OSEM) reconstruction. Recently, several groups have assessed this linear relationship under various conditions. Brasse et al. (*91*) found a linear relationship between SNR and the square-root of the NECR for two random correction methods when PET data was acquired in 3D and reconstructed using FORE-FBP and FORE-OSEM. El Fakhri et al. (*92*) found that the ratio of the square-root of the NECR of 2D and 3D at 3 different BMI values had a similar behavior to the SNR ratio for the 2 modes of PET data acquisition and reconstructed by 2D-OSEM and FORE-OSEM respectively.

Although many studies have shown that the square of the SNR is proportional to the NECR in various situations, some concerns about this relationship still exist. Wilson et al. (*93*) suggested that the choice of reconstruction algorithm and its associated parameters could have a large effect on image quality that could not be predicted by NECR alone. Others have raised concerns about this relationship when OSEM

reconstruction is used (*94-96*). This iterative algorithm provides a different noise propagation (*97,98*) as compared to FBP and such noise characteristics may affect the relationship between NECR and SNR. Badawi et al. (*99*) pointed out that spatial resolution and reconstruction methods frequently differ between systems or acquisition modes, so the NECR might not always track image quality in a meaningful manner. Additionally, the raw data may not follow a Poisson distribution because of effects such as detector dead time (*100*); thus, the use of the NECR may be limited. Furthermore, the NECR does not account for possible count rate bias such as the systematic mispositioning of data because of spatial pile-up effects (*101*).

The aim of this study is to evaluate using phantoms the relationship between the NECR and the SNR in PET imaging when a fully 3D OSEM reconstruction algorithm is applied. To our knowledge, this relationship has not been previously studied for a fully 3D OSEM reconstruction model. Another aim of this study is to evaluate the effects of the NECR-SNR relationship on patient results by analyzing patient studies with different body mass index (BMI) and scanner types. In both phantom and patient studies, linear and nonlinear reconstruction methods were used to evaluate this relationship while using various reconstruction parameters. Two different scanner designs were also included to assess the effect of detection efficiency from various detector materials on the NECR and SNR.

2.2 Materials and Methods

PET/CT Scanners

DSTE scanner: This scanner consists of a full-ring of bismuth germinate oxide (BGO) detectors arranged on four rings of 70 detector blocks. Each block consists of an 8×6 (tangential× axial) detector elements. The detector crystal size is 4.7*6.3*30 mm^3. The scanner has a trans-axial field of view (FOV) of 70 cm and a 15.7 cm axial extent. The scanner has retractable septa and can operate in both 2D and 3D modes. The energy window is 375-650 keV in 2D mode and 425-650 keV in 3D mode, while the coincident timing window width is 9.6 ns for both acquisition modes. The axial and transaxial resolution is 5.1 and 5.4 mm respectively. The sensitivity in 2D and 3D is 2.2 cps/kBq and 8.4 cps/kBq respectively. In 2D mode the peak NECR is 88 kcps at an AC of 43 kBq/cc, while in 3D mode, the peak NECR is 75 kcps at an AC of 13.1 kBq/cc. All measurements are based on the NEMA NU2-2007 standard. The full description and performance characteristics of this system can be found elsewhere (*102*).

DRX scanner: This scanner consists of a full-ring of lutetium yttrium orthosilicate (LYSO) detectors. It is arranged on four rings of 70 detector blocks. Each block is composed of a 9×6 (tangential×axial) detector elements. The detector crystal size is 4.2*6.3*30 mm^3. The trans-axial FOV for this system is 70 cm, and the axial extent is 15.7 cm. The scanner can operate in both 2D and 3D modes. The energy window is 425-650 keV in both 2D and 3D modes, while the coincident timing window width is 5.8 ns. The axial and transaxial resolution is 4.8 and 5.1 mm respectively. The system sensitivity in 2D and 3D is 1.7 cps/kBq and 7.3 cps/kBq respectively. The peak NECR is 155 kcps at 92.1 kBq/ml in 2D and 117.7 kcps at 21.7 kBq/ml in 3D. All measurements are based on the NEMA NU2-2007 standard. The description and performance characteristics of this system can be found elsewhere (*103*).

Phantom Studies

An anthropomorphic phantom (Radiology Support Device Inc., Long Beach, CA) was used in this study. The phantom was filled with F-18 water and scanned on a GE Discovery-STE (DSTE) PET/CT scanner (GE Healthcare, Waukesha, WI, USA) using 3D mode. Only one FOV was scanned, covering the lower chest and upper abdomen regions. In this regard, the acquisition contained scatter and random events from outside the FOV to emulate a real patient study, since the length of the phantom (52 cm) was greater than the axial FOV of the scanner (15.7 cm). Figure 2.1 illustrates the phantom and its position with the FOV of the scanner. The AC in the phantom at the beginning of

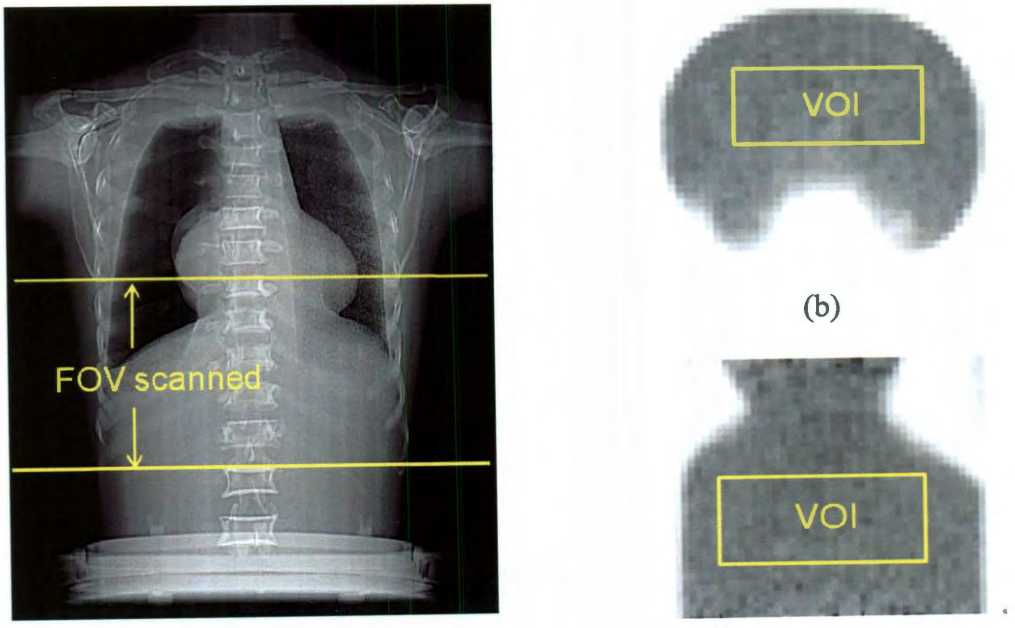

(a) (b) (c)

Figure 2.1: (a) Illustration of the FOV scanned for the anthropomorphic phantom, (b) transaxial and (c) coronal view of the PET image showing VOI drawn on the phantom.

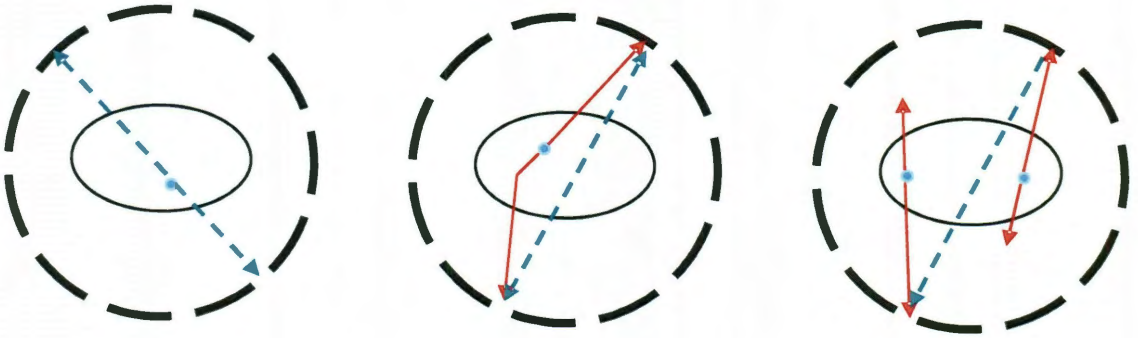

Figure 1.11: Three kinds of coincidences: (a) True, (b) Scatter and (c) Random

Scatter

When two single events are detected within the duration of the coincidence window of the PET scanner, they are recorded as a "coincidence". Figure 1.11 shows three kinds of coincidence events that PET scanners accept: true, scatter, and random coincidence events. Scatter coincidences occur when one or both of the photons from a single annihilation undergoes scattering and is detected by another detector rather than the one for a true coincidence (figure 1.11(b)). Scatter coincidences provide false localization of the annihilation, and lead to a broad distribution of mispositioned events. Scatter coincidences are from real annihilations, therefore reducing the activity administered to the patient, reducing the time window, or using a scintillator with faster light emission does not reduce the scatter coincidence fraction. The energy discrimination window of the PET scanner rejects some events whose energy differs significantly from 511 keV, thus reducing the effect of scatter coincidences to some extent (*50-52*). Annihilation photons that are not scattered by the human body but rather scattered by hitting detectors also deposit less energy than 511 keV. An energy discrimination window that encompasses only the photopeak rejects these true coincidences as well.

There are two main approaches for scatter correction in PET imaging. The first approach utilizes information from the original scatter-contaminated image and the transmission image to derive the correction (*53,54*). Here we note that the transmission image (e.g. CT) reflects the attenuation coefficient of the tissue, which can be related to the probability of scattering. The estimated contribution of scattered radiation is then subtracted from the total projections and the reconstruction is performed with the scatter-corrected data. This method works well when all the sources of radioactivity that could lead to scatter are contained within the FOV of the scanner. However, when large amounts of activity occur outside the FOV of the scanner, problems can arise. A second method for scatter correction is based on an examination of projection profiles immediately outside the object (*55,56*). Based on the premise that scatter is a low frequency phenomenon with little structure, data from the tails of the projections can be extrapolated by simple smoothly varying functions across the entire projection. Thus approximating scatter from radioactivity outside the FOV, this method is rapid but depends on the accuracy of the approximation to the true scatter distribution. In situations where the scatter distribution is complex, or when the object fills the whole FOV with no portion of the profile to examine outside the object, the technique may result in significant errors. In summary, scatter correction is very difficult problem that according to current literature has not been fully resolved.

Random

Random coincidences occur when annihilation photons from two different and unrelated positron annihilation events are detected and recorded as a single coincidence

acquisition time was set to 66.34 kBq/cc. PET data were acquired using dynamic mode for a total of 48 frames at 3 min/frame with a 12-min delay between frames. The same experiment was then repeated using the same AC on a GE Discovery-RX (DRX) scanner. The DRX scanner is similar to the DSTE system except that it has LYSO detectors compared to BGO for the DSTE system (refer to section on PET/CT scanners). Care was taken to place the phantom at identical axial and transaxial positions of both scanners to eliminate the effects of positioning on the NECR and SNR. This process was facilitated by the laser lights of the scanners and markings made on the phantom.

All PET data acquisitions were corrected for attenuation, random, scatter, and dead time using manufacturer software and were reconstructed using both 3D Reprojection (3D-RP) and VuePoint HD fully 3D OSEM (3D-OSEM) algorithms with varying parameters. This 3D-OSEM algorithm incorporates the corrections for attenuation, random and scatter coincidences inside the iterative loop to preserve the Poisson nature of the data (*104*). The reconstruction parameters used are listed in table 2.1. All the images were reconstructed using 128*128 transaxial matrix size with a 70cm FOV, thus having the voxel size of 5.47*5.47*3.27 mm^3. For 3D-OSEM reconstruction, different numbers of subsets were used while fixing the filter width, as well as different filter widths while fixing the number of subsets. These reconstruction schemes were used to evaluate the robustness of the NECR-SNR relationships with regard to the reconstruction parameters. Decay correction was turned off in all reconstructions since that option corrects the AC to the beginning of the dynamic scan, which causes all the frames to have the same AC, increases the image noise, and thus, affects the SNR. Two

event (figure 1.11(c)). Random coincidences add a relatively uniform background on the reconstructed image, suppressing contrast and distorting the relationship between image intensity and the actual amount of activity in the image. One approach to correct for random coincidences is the delayed timing window method (*57,58*). An estimation of the random coincidence rate is first obtained by delaying the coincidence timing window by a time that is much greater than its width. For example, with a timing window of 12 nanoseconds, the delayed window can be 64 nanoseconds. With this amount of time delay, only events that have arrival times separated between 64 and 76 nanoseconds are accepted. Therefore no true or scattered coincidences will be detected in the delayed window. The only detected random coincidences in the delayed windows will be relatively the same as those in undelayed windows because the rate at which uncorrelated photons strike the detector is the same for both windows. In this regard, the delayed window approach provides an estimation of the number of random coincidence events. This number is then subtracted from the total number of coincidence events for the detector pair. The other approach for correcting random coincidences is the singles rate method (*59*). The rate of random coincidences between any pair of detectors is estimated as:

$$R_{random} = 2\tau S_1 S_2 \tag{1.10}$$

where τ is the coincidence timing window, S_1 and S_2 are the actual count rates of the 2 detectors, which are often called singles rates. The timing window is the time interval following an interaction in a single detector in which an interaction in the other detector is considered to be a coincidence. However, there is a limit of the smallest extent the time window can be. If the time window is set to be too short, some true coincidences are also

parameters were calculated for each frame: the NECR from the raw data and the SNR from the reconstructed PET image.

Table 2.1: Reconstruction algorithms and parameters

PET/CT Systems	Reconstruction algorithms	
	3D-RP	VuePoint HD fully 3D-OSEM
DSTE	Transaxial filter: Hanning with 10.9 mm cutoff; Axial filter: Ramp with 6.5 mm cutoff	1) 2 iterations, 14 subsets, Gaussian 6 mm filter 2) 2 iterations, 20 subsets, Gaussian 6 mm filter 3) 2 iterations, 35 subsets, Gaussian 6 mm filter 4) 2 iterations, 20 subsets, Gaussian 4 mm filter 5) 2 iterations, 20 subsets, Gaussian 8 mm filter
DRX		1) 2 iterations, 15 subsets, Gaussian 6 mm filter 2) 2 iterations, 21 subsets, Gaussian 6 mm filter 3) 2 iterations, 35 subsets, Gaussian 6 mm filter 4) 2 iterations, 21 subsets, Gaussian 4 mm filter 5) 2 iterations, 21 subsets, Gaussian 8 mm filter

The NECR was defined by Strother et al. (*78*) as

$$NECR = \frac{T^2}{T + S + kR} \tag{2.1}$$

where T, S, and R are the true, scatter, and random count rates, respectively. The factor k is different for different methods of correcting random coincidences. In this investigation, random events were calculated on the basis of singles measurement; therefore, k was set to 1. Equation (2.1) can be rewritten as

rejected because of imprecision in the interaction timing. Scintillation materials that are able to emit light faster permit the use of shorter timing windows and therefore can better discriminate between true and random coincidences. The number of random coincidences calculated by equation 1.10 is then subtracted from the total number of coincidences (true + scatter + random).

Noise Equivalent Count Rate (NECR)

One method to assess the image quality in PET imaging is to calculate the noise equivalent count rate (NECR) in the acquired raw data. This metric has been suggested as a good indicator of image quality since it takes into account the effects of scatter, as well as random and true coincidences in its evaluation (*60-62*). NECR was defined by Strother et al. (*60*) as:

$$NECR = \frac{T^2}{T + S + kR} \tag{1.11}$$

where T, S and R are the true, scatter and random count rates, respectively. Factor k is defined as 1 or 2 depending on the randoms correcting approach. The delayed window correction method makes k equal to 2, whereas the singles rate correction method makes k equal to 1. According to the definition of NECR in equation 1.11, all factors that affect the relative counting rate of true, scatter and random coincidences can finally impact the NECR response. Such factors include the injected dose of the radioactive materials to the patient, scan time post-injection, scanner type, etc.

1.8 PET Image Quantification

As stated in beginning of this chapter, an important advantage of PET imaging is its ability to quantify the amount of radioactivity in the human body. This radioactivity value is directly related to the extent of malignancy of the tumor. The initial voxel values in a reconstructed PET image is in the unit of Bq/ml, however, this value can vary with patient weight, injected dose, scan time post injection, etc. One approach to standardize this value to a more universal indicator of radioactivity level is to calculate the Standardized Uptake Value (SUV) (*63*):

$$SUV = \frac{Initial\ Value}{Injected\ Dose / Patient\ Weight} \tag{1.12}$$

where *initial value* is the real voxel value from the reconstructed image (units of Bq/ml); *injected dose* (in units of Bq); and *patient weight* (in grams). Therefore, SUV is in units of g/ml. The SUV is a universal quantity that can help distinguish between benign and malignant lesions. In PET images, an SUV below 2.5 corresponds to a benign tissue; a SUV between 2.5 and 4 is indeterminate; and a SUV of 4 and above signals malignant lesions.

1.9 Forward to the Thesis

Recently, there have been three novel areas of development in PET imaging. This thesis focuses on investigating the topic of PET image quality in each of these areas. The first area is fully 3D PET data acquisition and reconstruction. Chapter 2 assesses the properties of PET image signal-to-noise ratio (SNR) and PET raw data NECR when a fully 3D acquisition and reconstruction is performed. The second area is time-of-flight

(TOF) PET data acquisition and reconstruction. Chapter 3 focuses first on an optimization of the reconstruction parameters for TOF reconstruction, followed by an assessment of the improvement in TOF image quality. The third area of development is PET/MR multi-modality imaging. Chapter 4 provides a feasible method of attenuation correction in potential PET/MR systems for the improvement of image quality and quantification.

First Area: 3D PET Acquisition and Reconstruction

PET data can be acquired in either 2-D or 3-D mode (figure 1.12). Historically, most PET imaging has been performed in 2D mode, where lead septa are placed between

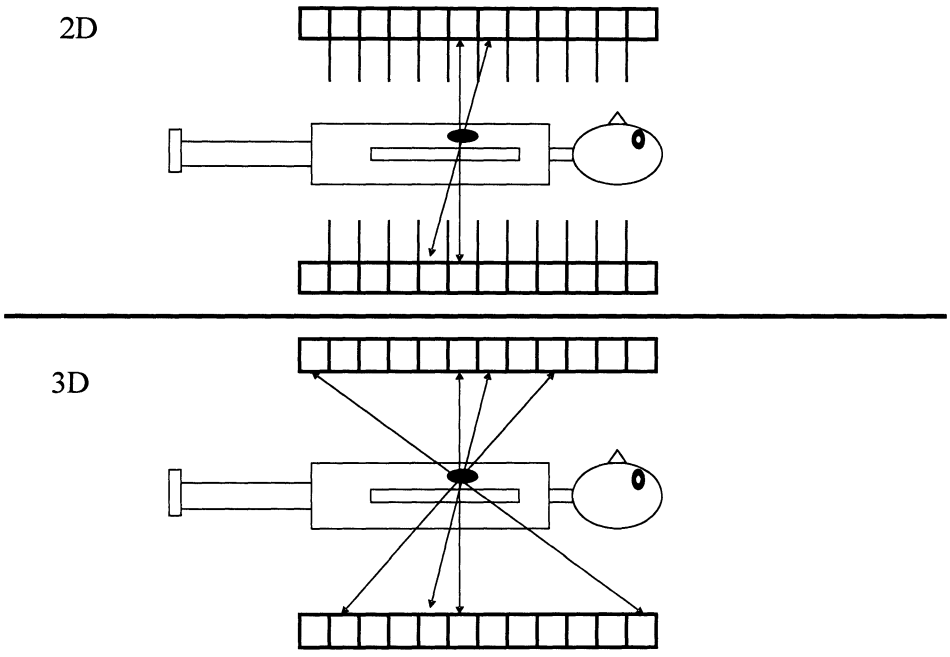

Figure 1.12: 2-D vs. 3-D mode in PET imaging

the planes of the detector elements to reduce detection of scattered photons. In this regard, an acceptable LOR is constrained in the transaxial planes by an axial spanning of no more than two adjacent detector rings. In the past, 2D imaging has been preferred over 3D largely due to the complexity of 3D image reconstruction algorithms. However, 2D imaging requires more administered activity to the patients to obtain adequate count rates when compared to 3D, since 3D has roughly a five-fold greater sensitivity than 2D. This situation changed around year 2003 with the development of new scatter correction techniques and faster and more efficient 3D reconstruction algorithms. These advances have allowed 3D imaging to become the predominant mode of PET data acquisition. In the 3D acquisition mode, data are collected with these lead septa retracted (*64*). Consequently, LORs are not constrained in the transaxial planes and may span across many detector rings. 3D acquisition provides better detection since it can accept more coincidences. In addition, it can result in a lower radiation dose to the patient and shorter imaging times. However, this higher sensitivity in 3D comes at the expense of higher scatter and random counts (*65*). In addition, there are many more LORs in a 3D acquisition compared to a 2D acquisition requiring more memory and computational power for image reconstruction.

With the increased interest in 3D imaging, 2D FBP reconstruction was extended to 3D with the introduction of the re-projection algorithm (RP) (*66*). Also OSEM for 2D PET scan was advanced to a re-binning procedure that converts the 3D data to 2D sonograms, prior to applying 2D OSEM (*67*). More recently, a fully 3D OSEM algorithm without a re-binning process has been developed (*68*). This algorithm incorporates

corrections for random, scatter and attenuation coincidences within the iterative loop to improve image quality.

The aim of the first area project in this thesis is to evaluate the relationship between the NECR and the SNR in PET imaging when a fully 3D OSEM reconstruction algorithm is applied. To our knowledge, this relationship has not been studied previously for a fully 3D OSEM reconstruction model. An additional aim of this study is to evaluate the effects of the NECR-SNR relationship on patient results by analyzing patient studies that report different body mass indices (BMIs) and scanner types.

Second Area: Time-of-Flight (TOF) PET Acquisition and Reconstruction

A normal PET scanner cannot detect the precise location of the annihilation point along the LOR, and the reconstruction algorithm assumes a uniform probability for its location along the length of LOR lying within the object boundary. The availability of fast scintillators with high stopping power (e.g., LSO and LYSO) has facilitated development of the TOF PET scanner (*69*). TOF imaging requires the measurement of the difference between the detection times of the two photons from an annihilation event, hence the need for fast detectors. A TOF scanner characterizes the location of the annihilation point along the LOR with a precise measurement of the difference in arrival times, t1 and t2, of the two annihilation photons by a Gaussian probability distribution. Figure 1.13 is a schematic drawing indicating the localization of the emission point along the LOR in a TOF PET scanner. D is the object diameter. The FWHM of the spatial localization along the LOR is calculated as $\Delta x=c(t1-t2)/2$, where c is the speed of light. This localization leads to reduced noise propagation in the reconstruction algorithm. This

$$NECR = \frac{(P-R)^2 \times (1-sf)^2}{T+S'+R'} \tag{2.2}$$

where P, R, and sf are the prompts rate, randoms rate, and scatter fraction, respectively. sf is defined as $S/(S+T)$. Prompts were defined as the sum of true, scatter, and random events. In this equation, R' and S' are corrected randoms and scatter rates that included only the projections that passed through the phantom. This was achieved by first determining the phantom body contour from the CT images. The contour was then used to simulate a noiseless sinogram using forward projection (figure 2.2). The resulting

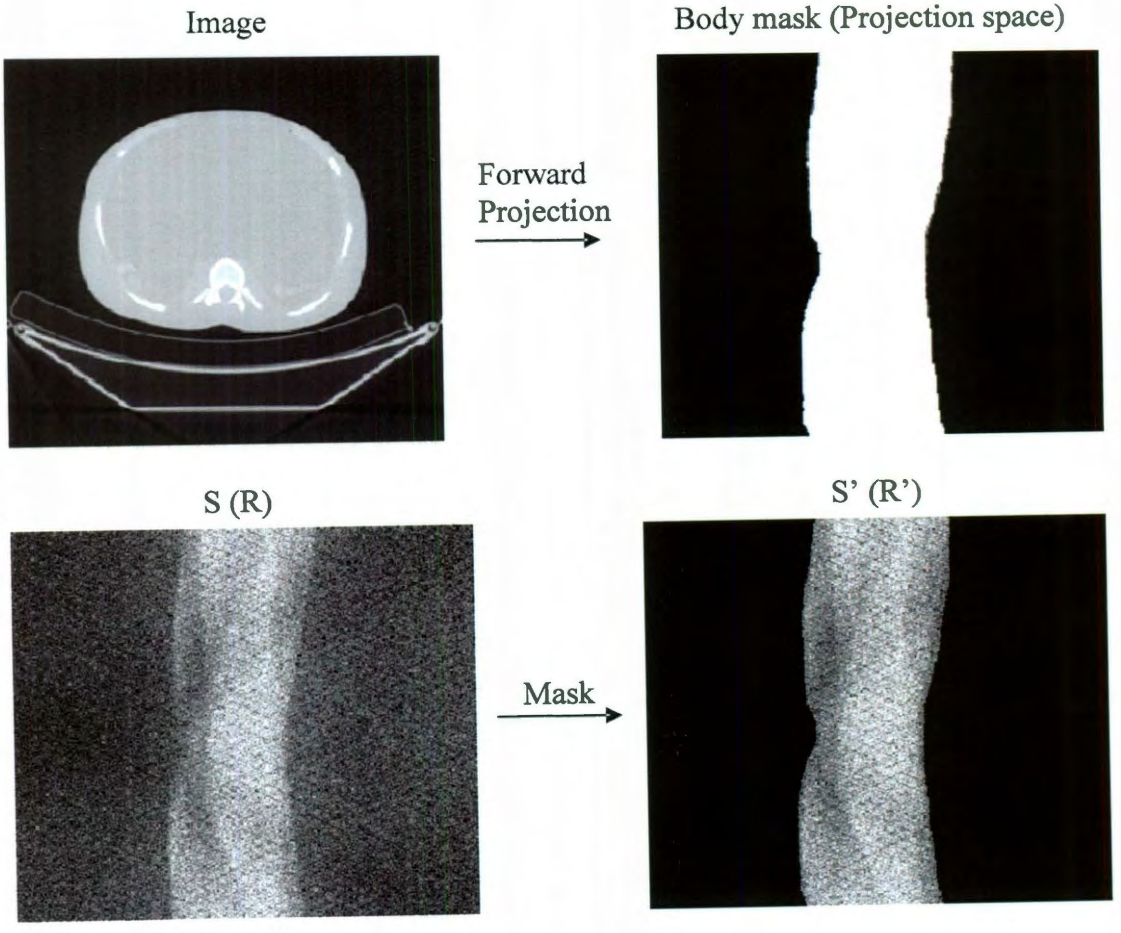

Figure 2.2: Illustration of using simulated body mask to mask S and R, and resulting S' and R'.

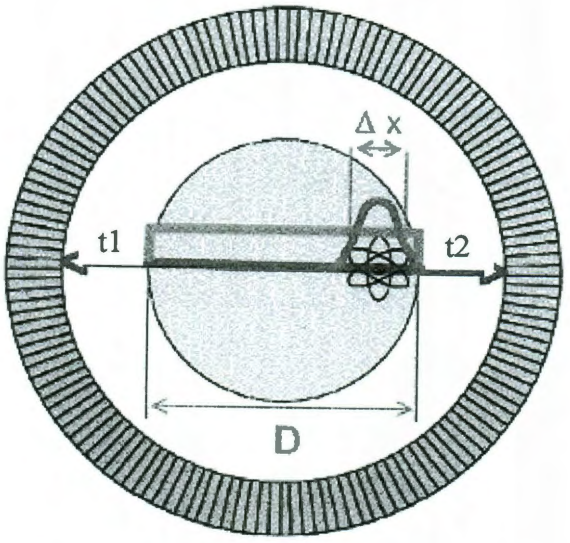

Figure 1.13: A schematic diagram of the localization of the emission point along an LOR in a TOF scanner.

improvement in image quality is manifest as an increase in the SNR that is proportional to the square root of D/Δx (*70*). Current commercially available PET/CT scanners with TOF capability have timing resolution that can identify the location of an annihilation event to within 7-10 cm of spatial uncertainty in the scanner's FOV. As the TOF resolution improves, spatial uncertainty decreases and the SNR increases by a larger factor. Furthermore, as the cross section of the imaged object increases, the improvement in SNR also increases by a large factor. This has an important advantage in improved image quality for large patients, since conventional imaging of this patient population yields inferior image quality due to low counting rates or requiring long scanning sessions at the expense of patient comfort.

The aim of the second project is to first optimize the reconstruction parameters for both TOF and non-TOF reconstruction on a newly developed TOF PET scanner. Then using these optimal parameters, assess image quality for the TOF and non-TOF

sinogram was finally used to decide which projections passed through the phantom habitus. In equation (2.2), P, R and sf are obtained from the patient's raw data which can be extracted directly from the recorded file header on the GE Discovery PET/CT scanners. T is then calculated as $(P-R)*(1-sf)$. R' and S' are calculated by multiplying the randoms and scatter rates respectively by a fraction (f) determined as the ratio of the $R+S$ within a body mask to the total $R+S$ in the sonogram (figure 2.2).

The SNR for each PET image was calculated from the ratio of the mean to standard deviation of 200 randomly selected non-neighboring voxels in a fixed VOI (10*25*15 voxels as shown in figures 2.1(b) and 2.1(c)) drawn in the uniform background. We chose to calculate noise using this approach to reduce correlations between neighboring voxels caused by the reconstruction process (*97,105,106*). The SNR was calculated for all the images in the different dynamic frames, reconstruction algorithms, parameters, and scanner types. The SNR squared was then plotted versus the NECR for each scanner, reconstruction method, and parameter to assess their relationships. The NECR and SNR values from different frames, reconstruction algorithms, parameters, and scanners were also plotted versus AC and evaluated.

Patient Studies

A total of 40 patients' PET/CT studies were evaluated retrospectively. These patients were divided into 2 groups of 20 patients per scanner model (DSTE & DRX). Each group of 20 patients were further divided into 2 BMI subgroups (small & large), giving a total of 10 patients in each BMI & scanner subgroup (table 2.2). The injected

dose and post injection time were kept similar among these subgroups to eliminate any potential effects of these parameters on the results of the study. None of the selected patients had a liver lesion or non-uniformity in order to minimize any bias due to differential liver uptake. An institutional retrospective chart review PA11-0820 was obtained for this study.

Table 2.2: Patients information

Subgroup category	Number of patients	PET/CT systems	BMI (kg/m^2)	Injected dose (MBq)	Post injection time (min)
DSTE, small BMI	10	DSTE	26.1±1.4	418.1±33.3	63.4±3.3
DSTE, large BMI	10	DSTE	32.4±2.2	429.2±51.8	63.2±4.5
DRX, small BMI	10	DRX	24.6±1.5	436.6±48.1	64.2±4.9
DRX, large BMI	10	DRX	31.9±1.8	451.4±48.1	60.4±1.0

PET data were acquired in 3D mode using 3 minutes per bed position. Images were reconstructed using 3D-OSEM (DRX: 2 iterations, 21 subsets; DSTE: 2 iterations, 20 subsets) and a post-reconstruction filter of 6 mm FWHM (clinical protocol at our institution). In addition, patients' data were reconstructed using 3D-RP to evaluate the NECR-SNR relationship between scanners, BMIs, and reconstruction algorithms.

The NECR of the bed position covering the patient liver and the SNR in the liver were calculated for each patient. The liver was used in both cases since it represents the largest organ that is characterized by a relatively high and uniform activity concentration. NECR was determined using the same approach described in the phantom studies above. SNR on the other hand, was calculated from the ratio of the mean to standard deviation of 50 randomly selected non-neighboring voxels in a fixed size VOI (6*6*20 voxels) drawn in the liver of each patient. The NECR and SNR calculated for each patient were then averaged for each subgroup. A comparison of patients' NECR and SNR between different scanner types and BMIs was then performed using a t-test on the original 10 patients' data in each subgroup and a p value less than 5% was considered significant.

2.3 Results

Phantom Studies

Figures 2.1(b) and 2.1(c) show the transaxial and coronal PET image of the phantom, respectively. The position of VOI drawn in the phantom to calculate SNR is also illustrated on these figures. Figures 2.3(a), 2.3(b) and 2.3(c) show the SNR squared versus the NECR for the 3D-RP and 3D-OSEM reconstructions. Each data point in figure 2.3 corresponds to the results from one of the acquired dynamic frames. A linear

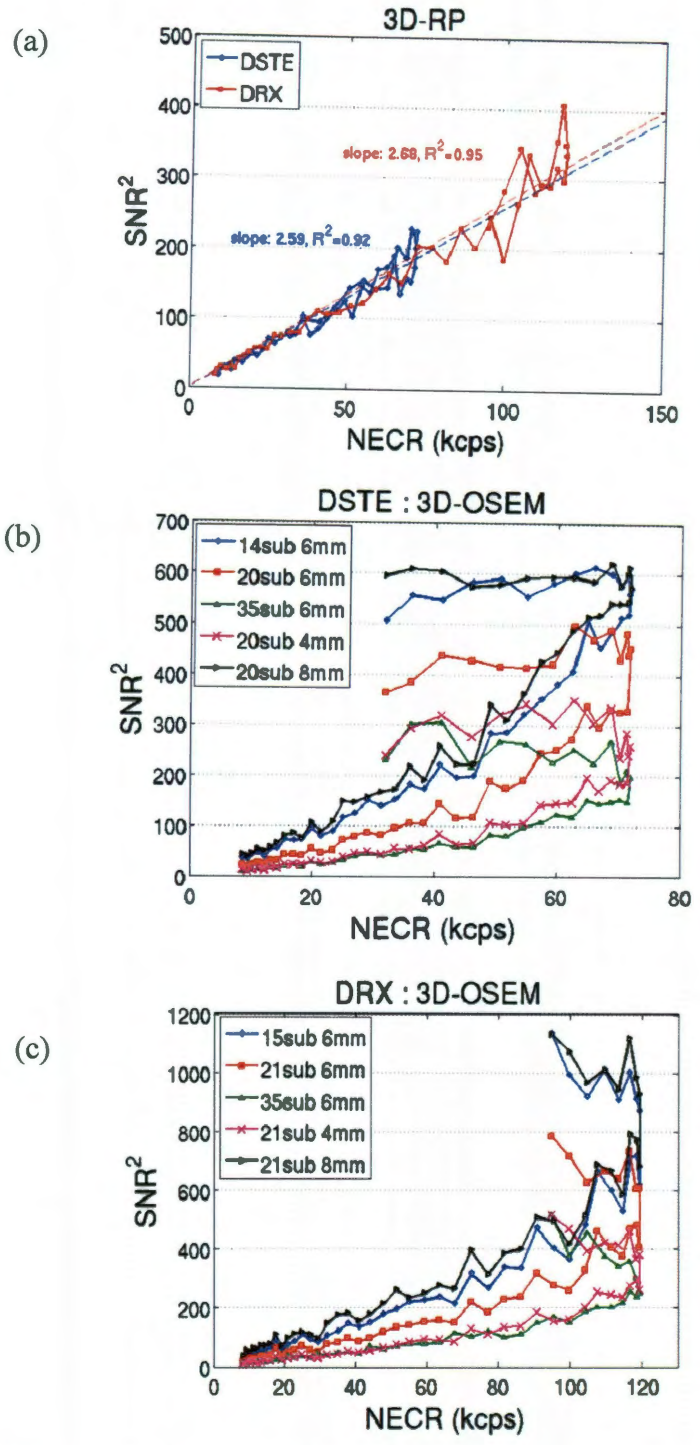

Figure 2.3: SNR squared vs. NECR for different scanners and reconstruction algorithms: (a) images reconstructed using 3D-RP on both scanners, (b) images reconstructed using 3D-OSEM with various subsets and filter widths on the DSTE scanner, (c) images reconstructed using 3D-OSEM with various subsets and filter widths on the DRX scanner.

correlation can be seen in figure 2.3(a) for the 3D-RP reconstruction. Linear curve fittings lead to r^2 of 0.92 and 0.95 for the two scanners respectively (figure 2.3(a)). However, figures 2.3(b) and 2.3(c) show nonlinear relationships between these two variables for the 3D-OSEM reconstruction regardless of the reconstruction parameters and scanner types. The plot shows that the square of the SNR was linearly related to the NECR before the NECR reached its peak. The NECR then decreased from its peak value at high AC while the SNR squared did not track the changes of NECR, resulting in a nonlinear relationship between these two variables.

We also plotted the square of the SNR vs. the trues rate in figures 2.4 and 2.5. Results of fixed filter width and varying subsets were plotted in figure 2.4 for the two scanners. Figure 2.5 shows the results of fixed subset and varying filter widths. Both figures show that the SNR squared and the trues rate were linear ($r^2>0.9$) when using 3D-OSEM reconstruction, regardless of the choice of scanner and reconstruction parameters.

Figures 2.6(a) and 2.6(b) show the relationship between the NECR and AC, trues rate vs. AC for both scanners, respectively. There is a large difference in peak NECR between the two scanners. The peak NECR for the DSTE scanner is 72 kcps and is achieved at 19 kBq/cc, while the peak NECR of the DRX scanner is 119 kcps at 31 kBq/cc. The NECR for the DSTE scanner decreases above 19 kBq/cc while the trues rate continue to increase and reaches its plateau at about 50 kBq/cc. On the other hand, the peak trues rate for the DRX scanner is never reached with the ACs used in this study.

(a)

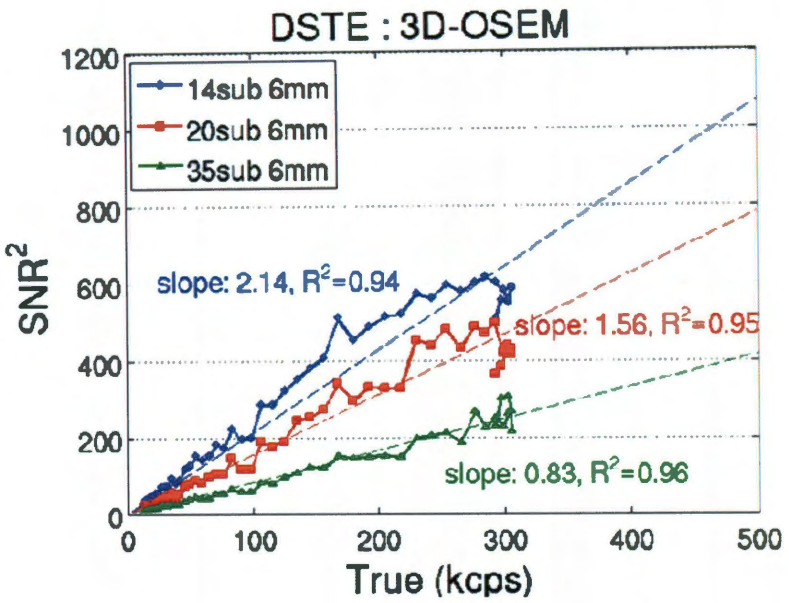

(b)

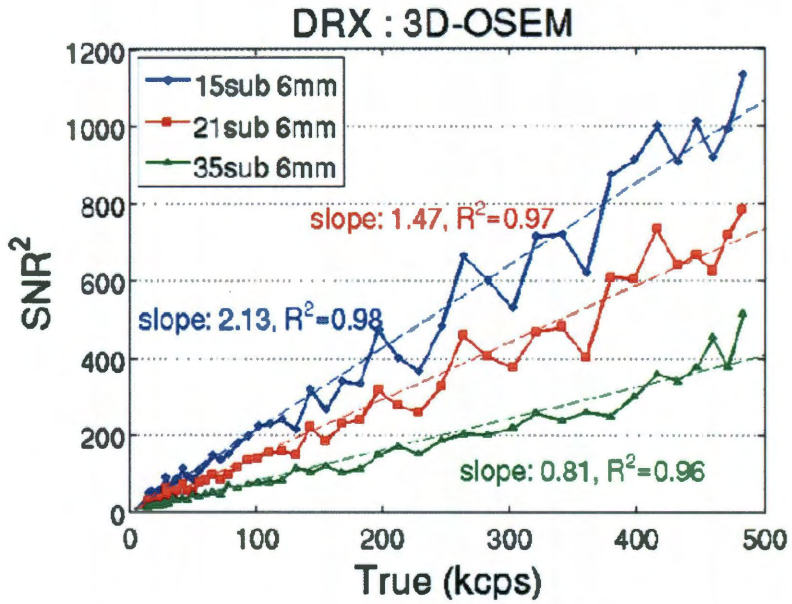

Figure 2.4: SNR squared vs. the trues rate using 3D-OSEM with fixed filter width and varying subsets for (a) DSTE and (b) DRX scanner.

(a)

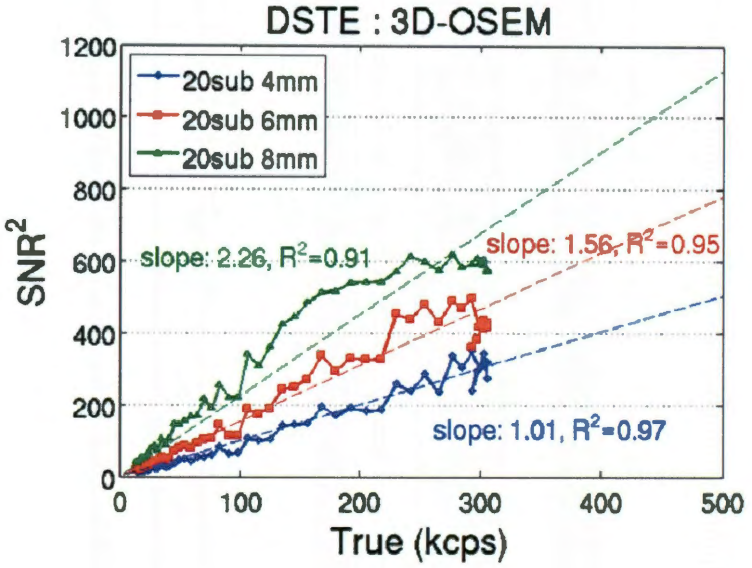

(b)

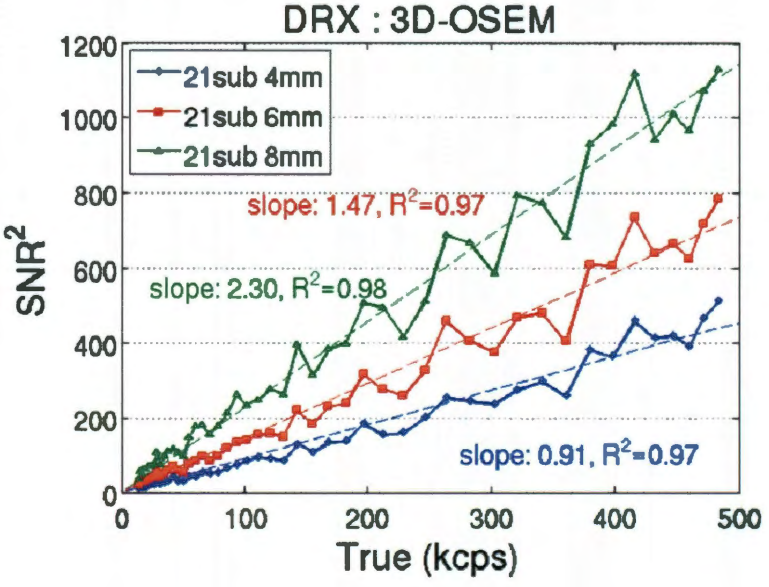

Figure 2.5: SNR squared vs. the trues rate using 3D-OSEM with fixed subset and varying filter widths for (a) DSTE and (b) DRX scanner.

(a)

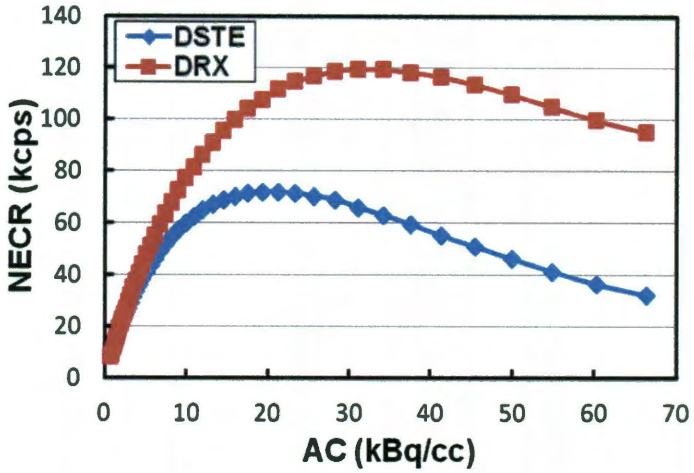

(b)

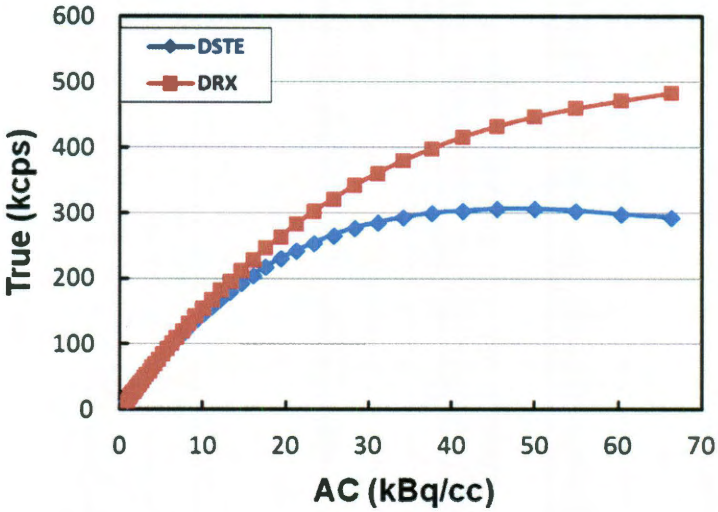

Figure 2.6: (a) NECR vs. AC curves for the two scanners, (b) trues rate vs. AC for the two scanners.

Figure 2.7(a) shows the SNR vs. AC on both scanners using the 3D-RP reconstruction. SNR vs. AC using 3D-OSEM with fixed filter width and fixed subset are shown in figures 2.7(b) and 2.7(c) respectively. Figure 2.7(a) shows that for

(a)

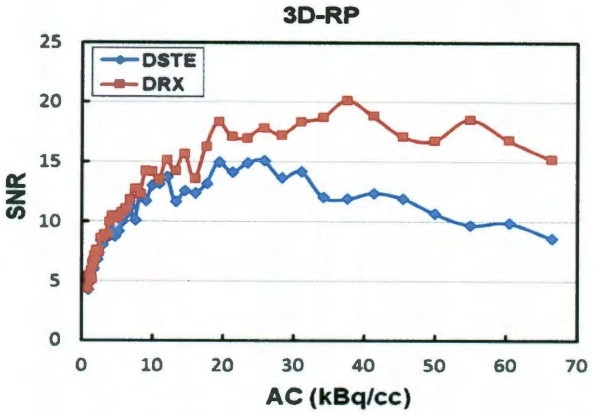

(b)

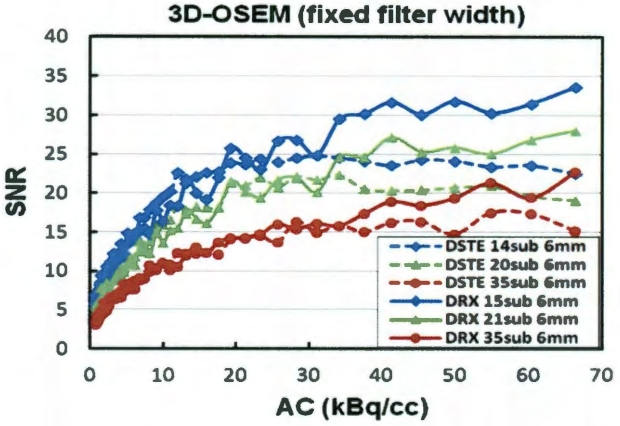

(c)

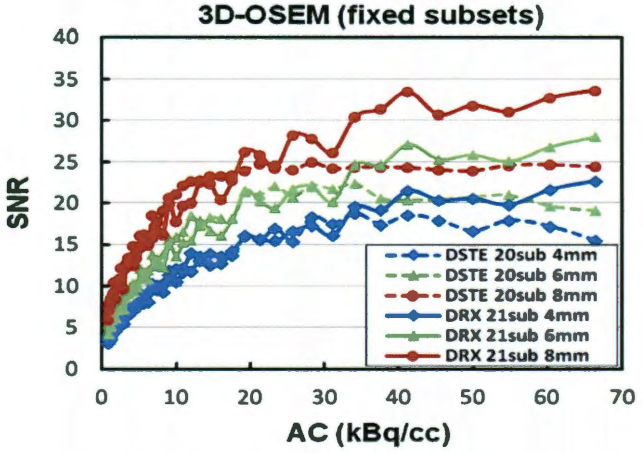

Figure 2.7: PET image SNR vs. AC for different scanners and reconstruction algorithms: (a) images reconstructed using 3D-RP on both scanners, (b) images reconstructed using 3D-OSEM with fixed filter width and varying subsets on both scanners, (c) images reconstructed using 3D-OSEM with fixed subset and varying filter widths on both scanners.

AC<30kBq/cc, the SNR for the DRX scanner was consistently higher by 12±10% than the DSTE scanner with 3D-RP reconstruction (p<5%). However, when using 3D-OSEM reconstruction with similar parameters, the two scanners had similar SNRs ($2 \pm 9\%$ difference on average) (p>5%) despite their having different NECRs (figures 2.7(b) and 2.7(c)). For ACs above 30kBq/cc, there is a large difference for both the NECR and the trues rate between the two scanners (figure 2.6), therefore SNRs start to deviate between the two scanners for both algorithms.

Patient Studies

The NECR and the SNR in the liver for each patient subgroup are shown in figure 2.8. Figure 2.8(a) shows the average NECR for each BMI and scanner subgroup. The NECR values are on average higher by 47% for the DRX scanner when compared to the DSTE scanner, and this difference is statistically significant (p<1%). The NECRs decreased by an average of 26% when BMI changed from the small to the large subgroup, and this change was statistically significant (p<1%).

Figure 2.8(b) shows the average SNR for each BMI and scanner subgroup using the 3D-RP reconstruction. The SNR values are on average higher by 21% for the DRX scanner when compared to the DSTE scanner (comparison of blue-to-blue & red-to-red bars) as expected. This difference is statistically significant (p<5%). SNR on average decreases by 21% when BMI changes from small to large subgroup. This difference is also statistically significant (p<5%).

Figure 2.8(c) shows the average SNR for each BMI and scanner subgroup using the 3D-OSEM reconstruction. The SNR between the two scanners is on average different

by 3% (comparison of blue-to-blue & red-to-red bars) and is not statistically significant despite these two systems having different NECRs. On the other hand, SNR on average decreases by 13% when BMI changes from small to large subgroup. This difference is statistically significant (p<5%).

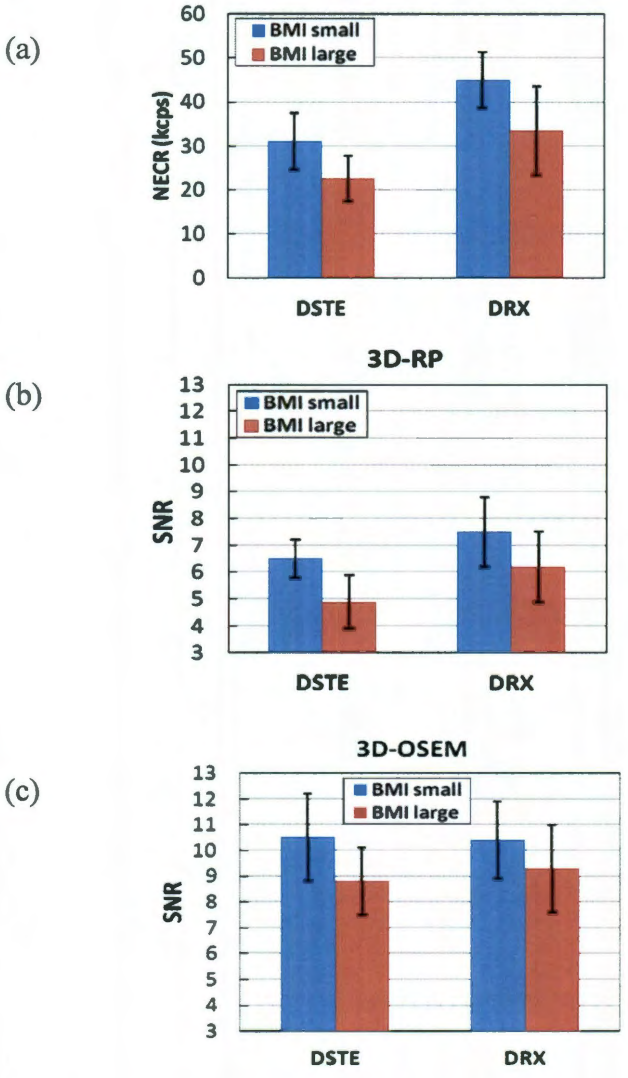

Figure 2.8: The NECR and the SNR in the liver for each patient subgroup: (a) the average NECR for each BMI and scanner subgroup; the average SNR for each BMI and scanner subgroup using (b) 3D-RP and (c) 3D-OSEM.

Figure 2.9 shows PET images of four patients from four subgroups (table 2.2) respectively. Subfigures (a) and (b) correspond to patients scanned on DSTE with small and large BMIs respectively, while subfigures (c) and (d) correspond to patients scanned on DRX scanner with small and large BMIs respectively. All images were reconstructed

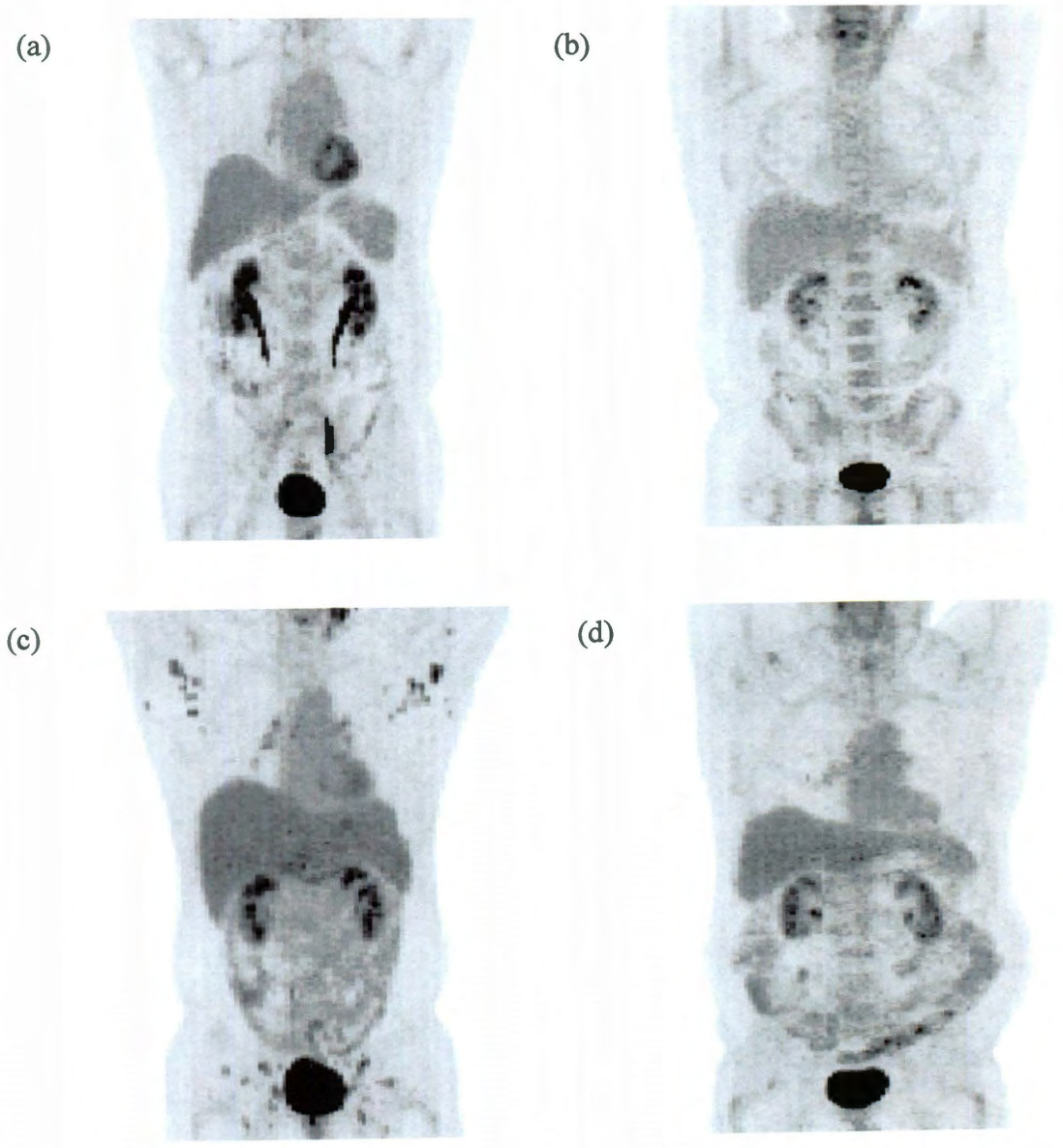

Figure 2.9: PET images of 4 patients from 4 subgroups (table 2.2): (a) small BMI on DSTE, (b) large BMI on DSTE, (c) small BMI on DRX, (d) large BMI on DRX.

using 3D-OSEM. The NECRs of the four patients were 27.5, 17.7, 49.0 and 36.2 kcps, respectively, while the corresponding image SNR in the liver using 3D-OSEM were 11.09, 9.18, 11.22 and 9.45, respectively. On the other hand, the SNRs for these patients when using 3D-RP were 6.78, 4.15, 9.09 and 5.82, respectively.

2.4 Discussion

The aim of this study was to evaluate the linear relationship between the PET raw data NECR and the image SNR for fully 3D-OSEM reconstructions. Our results can be used to clarify the relationship between these metrics (*93-96,99-101*) with regard to the choice of reconstruction algorithms and their associated parameters. Our investigation was based on phantom and patient studies. Two different reconstruction methods were used: a linear (3D-RP) and a nonlinear (3D-OSEM) approach respectively (table 2.1). The NECR was calculated based on the events within the phantom/patient contour only, and the SNR was calculated using non-neighboring voxels to reduce correlations between neighboring voxels caused by the reconstruction process.

Figure 2.3(a) clearly shows a linear correlation between the SNR squared and the NECR in 3D-RP reconstruction. This linear relationship is based on the linear noise propagation of this reconstruction method (*89*). The average signal in the reconstructed image is proportional to the true counts (T) after correction for scatter (S) and random (R) coincidences. However, when assessing the variance of the signal, one should account for the error propagation in correcting S and R. The correction is conducted by subtracting S and R to obtain T only, and thus the resulting variance after such correction should be $T+S+R$ (*107*). This relationship is reflected in the following equation:

$$SNR^2 = \frac{\text{signal}^2}{\text{variance}} \propto \frac{T^2}{T+S+R} = NECR \tag{2.3}$$

However, figures 2.3(b) and 2.3(c) show that the relationship between these two variables was non-linear when using 3D-OSEM reconstruction irrespective of the scanner and reconstruction parameters used. We postulate the reason for this result is that this algorithm (the GE VuePoint 3D-OSEM algorithm) does not correct for *S* and *R* by subtraction of the estimated *S* and *R* respectively, but rather incorporating the corrections inside the iterative loop. Such an approach minimizes the error propagation in correcting *S* and *R* and improves image quality. In this regard, we propose that equation (2.3) could be rewritten for 3D-OSEM reconstruction as follows:

$$SNR^2 = \frac{\text{signal}^2}{\text{variance}} \propto \frac{T^2}{T} = T \tag{2.4}$$

Therefore the square of the SNR is proportional to the true count rate for 3D-OSEM reconstruction.

To validate equation (2.4), we plotted the square of the SNR vs. the trues rate in figures 2.4 and 2.5 using varying reconstruction subsets and filter widths respectively. The SNR squared and the trues rate were linear (r^2>0.9) when using 3D-OSEM reconstruction, regardless of the choice of scanner and reconstruction parameters. These results support our hypothesis in equation (2.4). Figure 2.4 also shows that SNR decreases with the increasing number of subsets. This is expected since image noise increases with the increasing number of subsets. Figure 2.5 shows that SNR increases with the increasing filter widths. This is also expected since noise decreases with larger filter widths.

The results in figure 2.7(a) show that for ACs <30kBq/cc, the image SNR of the DRX scanner was higher than that of the DSTE scanner when 3D-RP reconstruction was used ($p<5\%$). This is expected since the NECR of the DRX scanner is higher than that of the DSTE (figure 2.6(a)). However, when 3D-OSEM reconstruction was used, the two scanners had similar SNRs despite having different NECRs. Similar results are also found from patient studies irrespective of BMI shown in figure 2.8. The difference in NECR as well as SNR between the two scanners when using 3D-RP is statistically significant (figures 2.8(a), 2.8(b)). However, the SNR between the two scanners is not statistically significantly different when using 3D-OSEM (figure 2.8(c)). These findings corroborate our previous results based on 180 patients' PET scans reconstructed using 3D-OSEM (*108*), whereby no statistically significant difference in the amount of image noise between the two scanners was found even though the difference in the NECRs was statistically significant. This finding suggests that the SNR may not correlate with the NECR when 3D-OSEM reconstruction is used. Since the two scanners have similar spatial resolution, quantitative accuracy, etc (*102,103*), image SNR can be regarded as a representation of image quality for these two scanners. In this regard, our results suggest that when comparing DSTE and DRX scanners, a better count rate performance does not translate to a better image quality when using VuePoint 3D-OSEM reconstruction algorithm. Further work is required to validate this finding on other PET/CT scanner types and/or other 3D-OSEM algorithms.

In summary, our investigation confirms the linear relationship between the square of the SNR and the NECR for the linear reconstruction and demonstrates the absence of such a relationship for the 3D-OSEM reconstruction at high AC. On the other hand, the

square of the SNR and the trues rate were found to be linear for the 3D-OSEM reconstruction for the entire AC range used in this study. Furthermore, our results suggest that for the scanners used in this study, higher NECRs do not result in better image quality when 3D-OSEM is used.

A potential limitation of the results is that the two PET/CT machines might have different calibration or correction accuracies that might have affected the corresponding image SNR while sparing the NECR performance. However, both scanners used in this study are based on the GE Discovery PET/CT scanner series. Both systems have similar reconstruction engines (VuePoint fully 3D-OSEM), same scatter, random, attenuation, and normalization correction approaches. Moreover the phantom was placed at the same location of the two scanners. In this regard, we believe that the effects of these systematic corrections are negligible, and the count rate performance is the dominant effect that affects image quality between the two scanners.

The main limitation of this study was that the noise calculation was not based on multiple realizations of the phantom acquisitions, but rather on the standard deviation of voxels in one single scan. However, results from our previous work based on Ge-68 phantom studies using high and low activity concentrations (data not shown) showed that these two methods of calculating image noise generate similar noise values. Another limitation in our study is that there might be a bias in calculating the image noise in patients' liver due to the respiratory motion. Respiratory motion causes the image blurs in the liver, which might affect the liver noise values. In this regard, the VOI used for image noise measurement was placed in the lower portion of the liver to minimize the motion effects since that part of the liver is characterized by less motion when compared to

regions adjacent to the diaphragm. Furthermore, the reliability of the image noise calculation is based on patients with disease free liver. Therefore our image noise results cannot be directly extrapolated to those patients with liver tumors.

2.5 Conclusion

For clinical PET applications that require high injected ACs (e.g., cardiac imaging), the SNR cannot be predicted by the NECR when using 3D-OSEM reconstruction but should be based on the measured trues count rate. Furthermore, our results suggest that scanners with higher NECRs do not result in better image quality when 3D-OSEM is used.

Chapter 3

Optimization of the acquisition and reconstruction parameters for a time-of-flight PET/CT scanner

3.1 Background and Motivation

Time-of-flight (TOF) PET systems have the ability to measure the difference in arrival times of a pair of photons from their annihilation site. This idea was originally proposed in the 1960s (*109*) and the first TOF PET systems were developed in the 1980s (*110-112*). However the slow detectors of these early TOF PET systems precluded the development of such systems and the majority of these scanners were retired in the early 1990s. More recently, however, the development of new scintillators with good timing resolution, high stopping power, short decay time, high light output, and good energy resolution (*113-115*) has renewed interest in TOF PET systems. Currently there are several PET/CT scanners with TOF capabilities that are commercially available (*116-118*).

A TOF PET system can record the difference in arrival time between a pair of coincident photons. Such an ability allows the localization of the annihilation event along the line-of-response (LOR). The error in the localization is determined by the coincidence timing resolution (Δt) of the scanner. The uncertainty in localization along the LOR is given by

$$\Delta d = \Delta t \cdot c / 2 \tag{3.1}$$

where c is the speed of light. Current TOF systems have timing resolutions in the range of 500-600 ps, and thus correspond to a spatial uncertainty of 7-9 cm. Such an uncertainty, although cannot localize annihilation events to within a single voxel, is better than having no timing information at all since the latter results in assigning equal probability to all voxels along the LOR during image reconstruction. The improvement of event localization reduces the noise propagation to a segment of the LOR rather than spreading this noise across the full length of the LOR (*111*). The reduction of noise can be represented as a gain in signal-to-noise ratio (SNR) which is dependent on the object size (*119,120*). This gain is greater for larger object, suggesting that there is increased benefit in TOF imaging for larger patients.

Recently many groups evaluated PET image quality with TOF processing compared to that without TOF. Karp et al. (*121*) reported using phantom and patient studies, TOF reconstruction improved lesion contrast at matched noise levels with faster and more uniform convergence. Wilson et al. (*122*) assessed the ratio of contrast recovery for TOF to non-TOF with respect to a range of object sizes. A tapered phantom was used in this study to represent a range of body dimensions and the ratio was found to increase with increasing body dimensions. El Fakhri et al. (*123*) measured channelized hotelling observer (CHO) SNR for TOF and non-TOF for different lesion locations, scanning time, contrast, and body mass index (BMI) using patient studies. A greater gain in CHO SNR was found for lower contrast, larger subjects, and shorter acquisition times when using TOF imaging.

Several studies also suggested that different acquisition parameters could be used in TOF to maintain similar image quality as compared to non-TOF. Surti et al. (*124*)

compared the CHO SNR for TOF and non-TOF using phantoms with varying acquisition times. The results indicated that half scan time could be used for TOF, while achieving the same CHO SNR as in non-TOF reconstruction. A study of non-prewhitening matched filter SNR on phantoms also suggested a reduction of scan time for TOF (*125*). A more recent study by the same group using phantoms found that the injected activity could also be reduced for TOF while maintaining similar area under the localized receiver operating characteristic curve as for non-TOF (*126*).

In most of these studies, the same reconstruction parameters were used for TOF and non-TOF. However such a comparison may be potentially biased since the convergence rates of these two reconstruction approaches are different. Lois et al. (*127*) assessed the number of iterations need to optimize lesion SNR for both TOF and non-TOF reconstruction using phantoms, and found it differed between TOF and non-TOF. When the number of iterations is selected to maximize lesion SNR, a slightly lower contrast and a much lower noise level were found for TOF as compared to non-TOF. Such results are different with those derived in previous papers using the same reconstruction parameters for TOF and non-TOF. These papers on the other hand showed a higher contrast (*122*) and also a higher noise level (*121,125*) for TOF as compared to non-TOF. These different results suggest that when optimizing TOF and non-TOF reconstruction parameters, image quality will be different. In this regard, the benefit of TOF over non-TOF may be biased when using the same parameters since the comparison may be conducted between optimized and non-optimized results.

In addition to TOF imaging, recent PET/CT scanners have the ability to correct for image blurring due to system response (point spread function - PSF) (*128,129*).

Several studies have evaluated the image quality using PSF as well as TOF (*128-130*). These results showed that when PSF is included, convergence of iterative algorithm and consequently image quality is further changed. An improvement in image quality can be achieved by using PSF with more iteration. In this regard, the reconstruction parameters have to be further optimized when including PSF.

This study provides a comprehensive assessment of the image quality on the GE Discovery-690 (D-690) TOF PET/CT scanner (GE Healthcare, Waukesha, WI, USA). The aim of this study is to first optimize the iteration numbers for all iterative algorithms on this scanner: ordered subset expectation maximization (OSEM), +TOF, +PSF and +TOFPSF. We believe that such an optimization is necessary to perform a fair comparison of image quality between these algorithms. Following optimizations, the improvement in image quality of TOF, PSF, and TOFPSF with respect to OSEM was assessed. Finally the effect of scan duration was evaluated to determine whether similar image quality could be obtained using less scan time for TOF, PSF, and TOFPSF as compared to OSEM. Different phantom sizes, sphere sizes and sphere-to-background ratios (SBRs) were used for this comprehensive evaluation.

3.2 Materials and Methods

PET/CT scanners

GE D-690 TOF PET/CT scanner consists of full-ring lutetium yttrium orthosilicate (LYSO) detectors. It is composed of four rings of 64 detector blocks. Each block consists of 9×6 (tangential×axial) detector elements. The dimension of each element is $4.2\times6.3\times25mm^3$. The scanner has a trans-axial FOV of 70 cm and a 15.7 cm

axial extent. The scanner can acquire PET data in 3D mode only. The energy window is 425-650 keV, while the coincident timing window width is 4.9 ns. The system sensitivity is 7.0 cps/kBq. The peak NECR is 126 kcps at 30.3 kBq/ml. The measured timing resolution of the system is 650 ps. This system uses fully 3D OSEM algorithm. Moreover, TOF information and/or a model of the PSF can be applied to the OSEM providing additional TOF, PSF and TOFPSF options in reconstruction. The description and performance characteristics of this system have been published (*118,129*).

Phantom Studies

Three cubic phantoms (sides=20, 30, 40cm) simulating patients with different BMIs were scanned on the D-690 TOF PET/CT scanner. Each phantom was filled with F18 water to the height of 18cm to simulate BMIs of 20, 30, 40 kg/m^2 respectively. Each phantom was fitted with a NEMA IEC face plate containing six spheres (10-37mm). In each case, the two largest spheres (28, 37mm) were filled with cold water, while the 4 small spheres (10, 13, 17, 22mm) were filled with F18 water. Figure 3.1 shows the phantom setup. The scan was repeated for two SBRs (2:1 & 4:1) with background activity concentration of 0.13 uCi/cc. PET data for each phantom and SBR were acquired in LIST mode for 30 minutes and then rebinned to generate 10 realizations of 3 minutes data.

Figure 3.1: Phantom setup.

All PET data were reconstructed using OSEM, TOF, PSF and TOFPSF. For each algorithm, 12 subsets with varying 1-10, 15, 20, and 30 iterations were used. All the images were reconstructed using 256×256 transaxial matrix size with a 50cm FOV, thus having the voxel size of 1.95×1.95×3.27 mm^3. No filters were used in all reconstructions.

Optimization of iterations. A volume of interest (VOI) was drawn on the CT scan of each sphere and copied to the corresponding PET image. The mean value in each VOI was then measured to calculate the SUV mean in each sphere. The optimal number of iterations for each algorithm and phantom size was then determined as the convergence of the SUV mean for the SBR 4:1 in the smallest 10mm sphere. This convergence was

defined as the iteration that resulted in 95% of the SUV mean at the 30th iteration (360 equivalent iterations; 30×12 subsets).

Image quality evaluation. Image quality was compared between algorithms, phantom sizes, and sphere sizes, using the derived optimal iteration for each algorithm and phantom size. Image quality was evaluated in terms of signal-to-noise ratio (SNR), contrast recovery coefficient (CRC), and background variability (noise). These parameters were defined as follows

$$SNR = \frac{C_{hot} - C_{background}}{\sigma_{background}} \tag{3.2}$$

$$CRC(hot\ sphere) = \frac{C_{hot} / C_{background} - 1}{injected\ SBR - 1} \times 100\% \tag{3.3}$$

$$CRC(cold\ sphere) = (1 - \frac{C_{cold}}{C_{background}}) \times 100\% \tag{3.4}$$

$$noise = \frac{\sigma_{background}}{C_{background}} \times 100\% \tag{3.5}$$

where C_{hot}, C_{cold}, $C_{background}$ were the mean activity concentrations in the hot sphere VOI, cold sphere VOI, and background VOI respectively, and $\sigma_{background}$ was the standard deviation of the activity concentrations in the background VOI. Sphere VOI has been described above. Background VOI consisted of 3600 voxels in the phantom background.

Effect of scan duration. The LIST mode PET raw data were further rebinned into 10 realizations of 1 and 2 minutes respectively, and then reconstructed using TOF, PSF, and TOFPSF with the derived optimized iterations. SNR and CRC were calculated for these images and compared to those of OSEM acquired in 3 minutes. This comparison assessed whether similar image quality could be obtained for TOF and/or PSF with respect to OSEM by using shorter scan duration.

3.3 Results

Optimization of iterations. Figure 3.2 shows the SUV mean vs. iterations for SBR 4:1, 10 mm sphere, in small, medium and large phantoms respectively. Figure 3.3 shows the SUV mean vs. iteration for SBR 4:1, 22 mm sphere, in small, medium and large phantoms respectively. The results for SBR 2:1 follow a similar trend but are noisier. The SUV for the TOF reconstruction increases more quickly and reaches a slightly higher value than OSEM. Furthermore, PSF results in a lower value than TOF at a low number of iterations but can achieve higher values as the number of iterations increases, showing a further improvement in quantification. The best results were obtained when TOF and PSF were used together. Table 3.1 shows the number of iteration that results in 95% of the value at the 30th iteration, for each reconstruction algorithm and phantom size. The results in the table show that the convergence rate TOF > OSEM > TOFPSF > PSF, and also a faster convergence is achieved for the small phantom compared to larger phantoms. Figure 3.4 and 3.5 show the PET images of the phantoms for SBR 4:1 and 2:1 respectively using the iterations derived in table 3.1. The image quality deteriorates with

increasing phantom size. For SBR 2:1, the two smallest spheres could not be identified in any image.

(a)

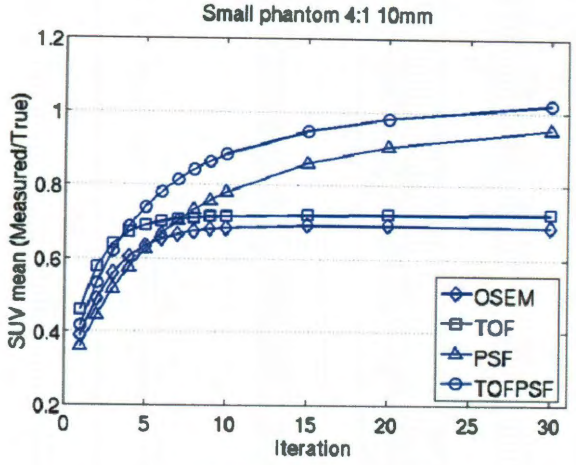

(b)

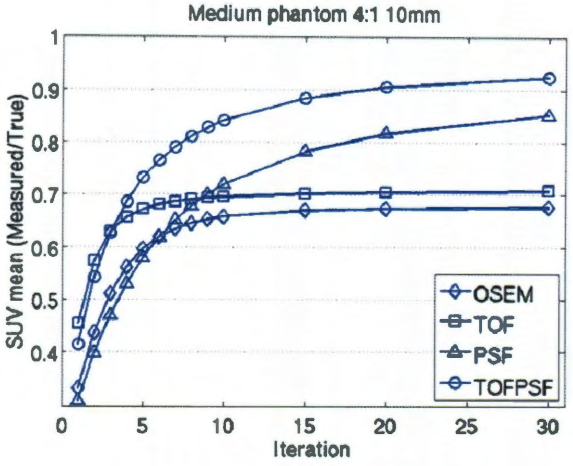

(c)

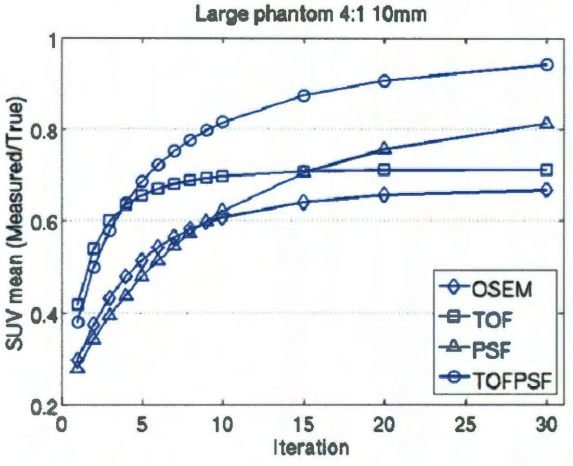

Figure 3.2: SUV mean vs. iterations for SBR 4:1, 10 mm sphere, in (a) small, (b) medium and (c) large phantoms respectively.

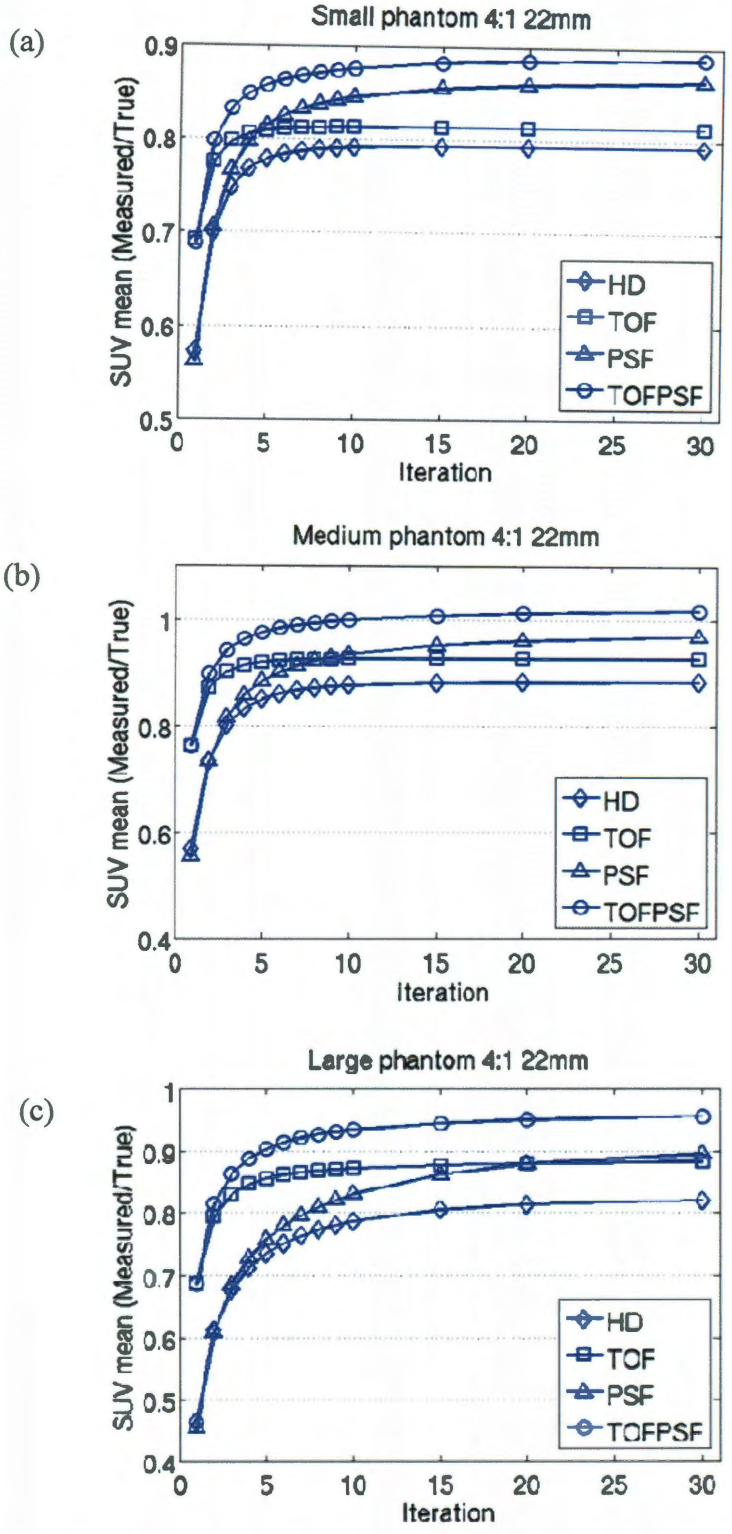

Figure 3.3: SUV mean vs. iterations for SBR 4:1, 22 mm sphere, in (a) small, (b) medium and (c) large phantoms respectively.

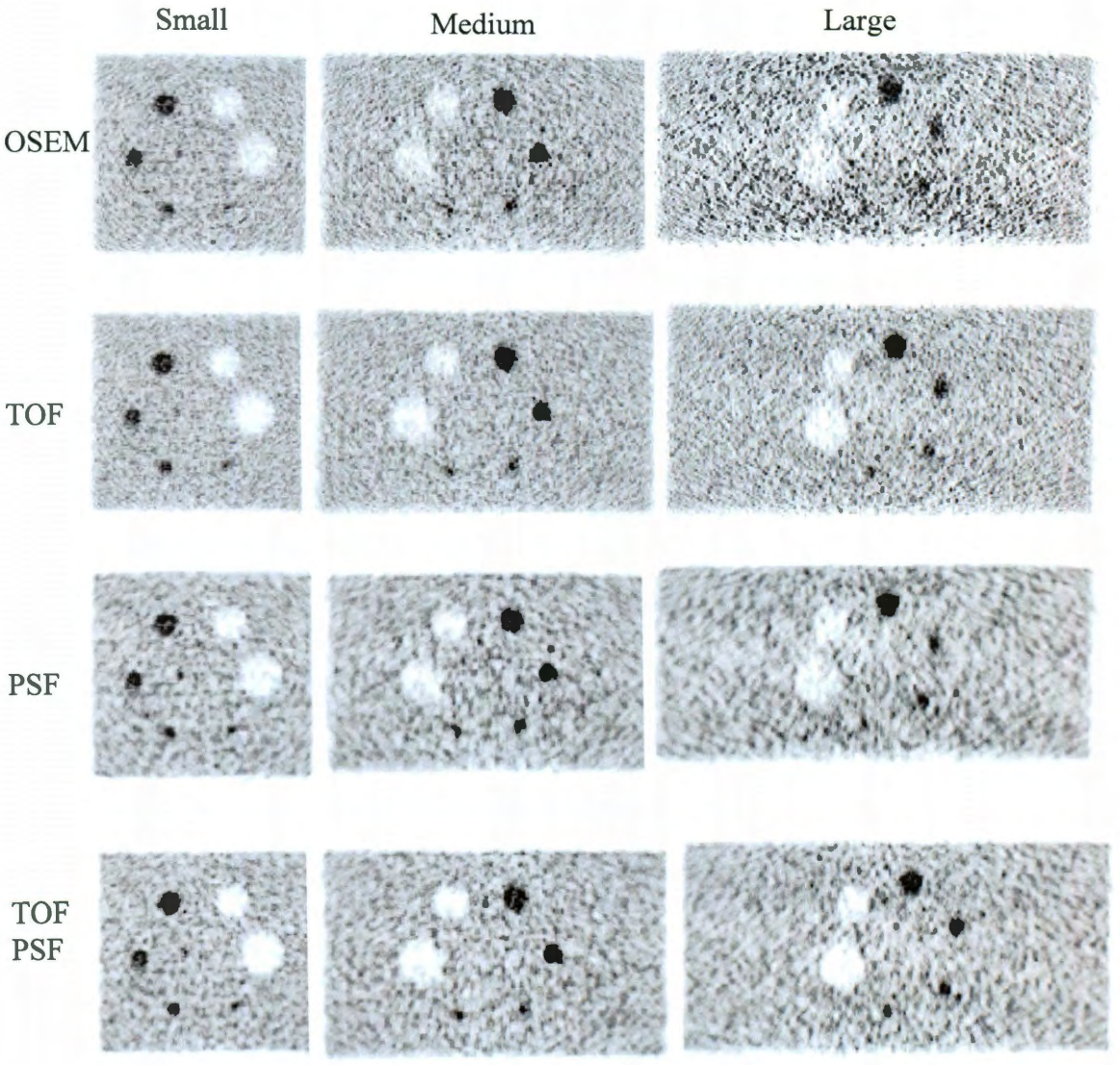

Figure 3.4: PET images of the phantoms for SBR 4:1 using the iterations derived in table 3.1.

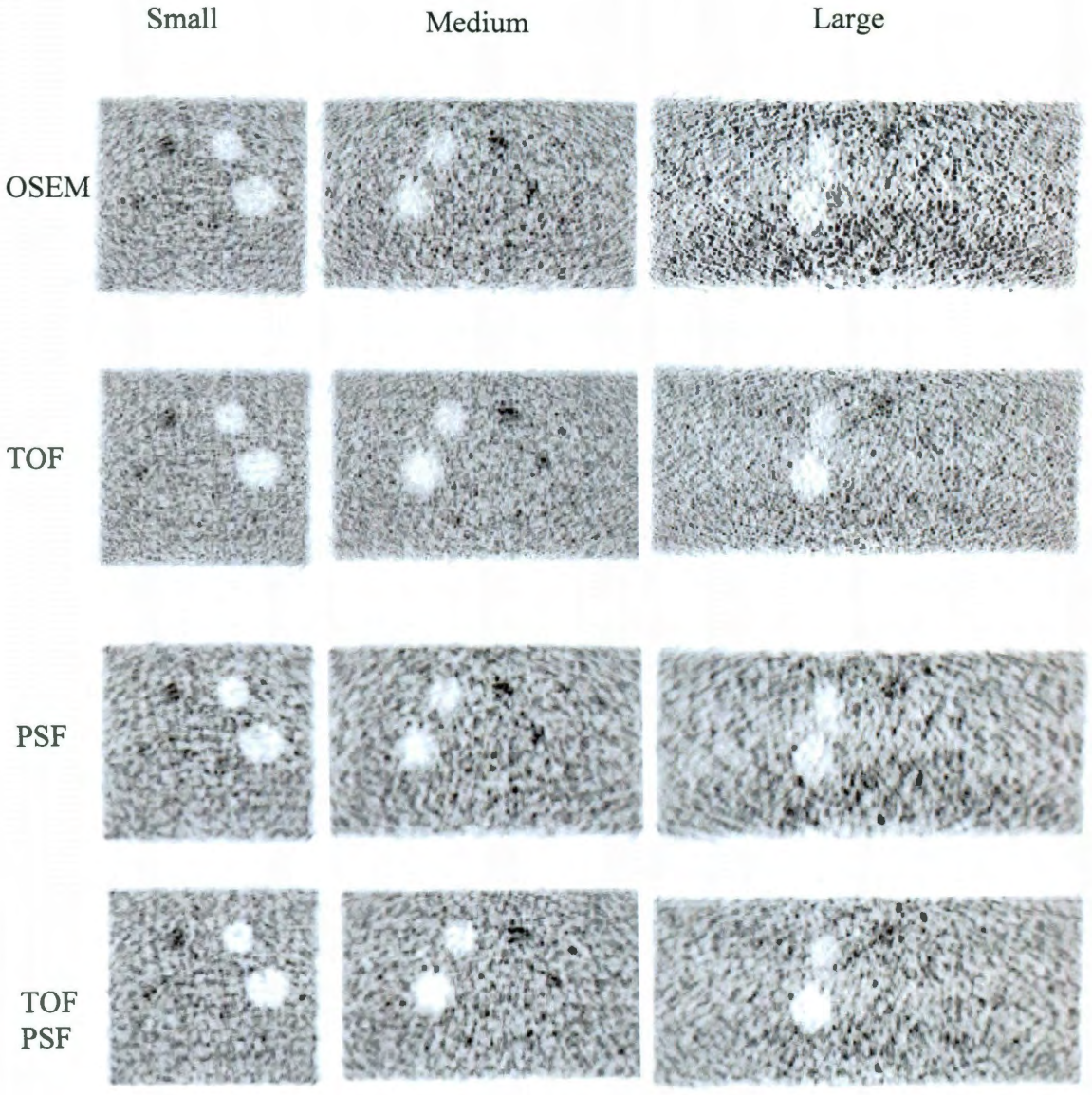

Figure 3.5: PET images of the phantoms for SBR 2:1 using the iterations derived in table 3.1.

Table 3.1: Optimized number of iterations for each algorithm and phantom size

	OSEM	TOF	PSF	TOFPSF
Small phantom	7	5	20	18
Medium phantom	9	5	21	18
Large phantom	18	8	25	20

Image quality evaluation. Figure 3.6 shows the SNR improvement (SNR-TOF, PSF, TOFPSF / SNR-OSEM respectively) in hot sphere vs. sphere diameter using the derived optimal iterations in table 3.1. The improvement in SNR increases with increasing phantom sizes. The average gain in SNR for TOF, PSF, TOFPSF compared to OSEM were 23±4%, 28±5%, 36±7% for the small; 49±7%, 39±5%, 56±11% for the medium; and 66±13%, 94±9%, 121±19% for the large phantom respectively. Furthermore, the improvements in SNR for TOF are constant among the different sphere size, with an average 49±14% and 44±4% higher than SNR-OSEM for the 10 and 22 mm sphere respectively. For PSF and TOFPSF on the other hand, the improvement in SNR decreases with increasing sphere sizes, SNR-PSF is on average 73±11% and 38±4% higher than SNR-OSEM for the 10 and 22 mm sphere respectively. For TOFPSF, these values are 95±24% and 49±5%. Figure 3.7 shows the CRC improvement (CRC-TOF, PSF, TOFPSF / CRC-OSEM respectively) vs. sphere diameter. The 4 smallest spheres in

(a)

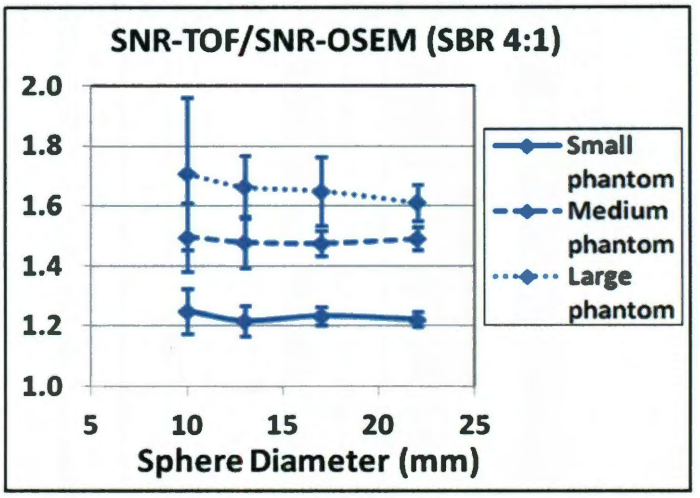

(b)

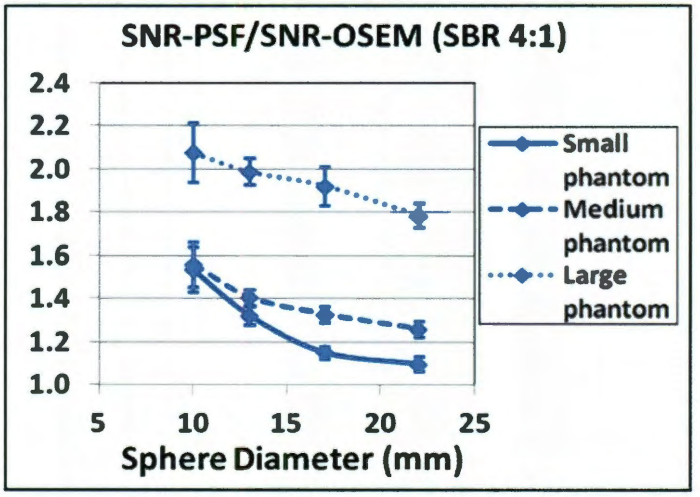

(c)

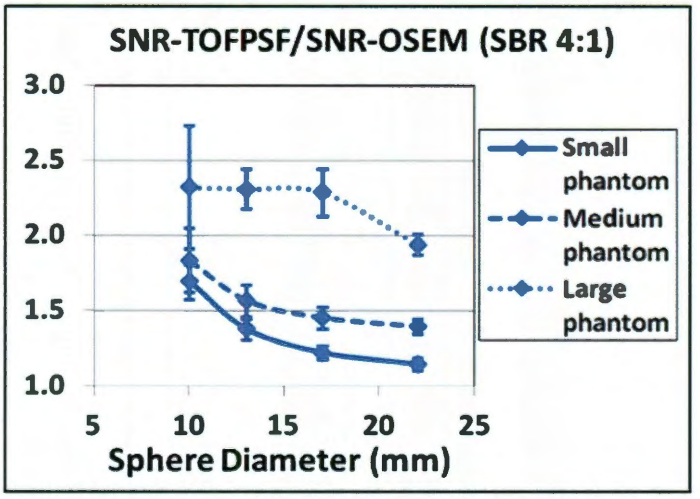

Figure 3.6: The SNR improvement (SNR-TOF, PSF, TOFPSF / SNR-OSEM respectively) in hot sphere vs. sphere diameter using the derived optimal iteration shown in table 3.1.

(a)

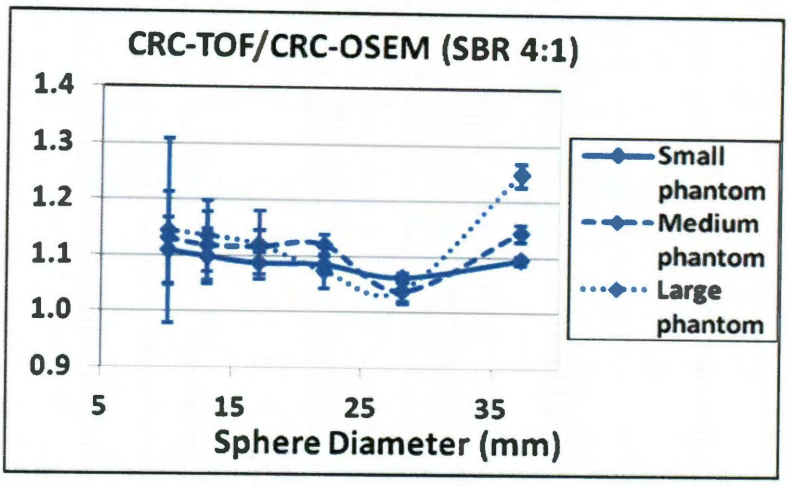

(b)

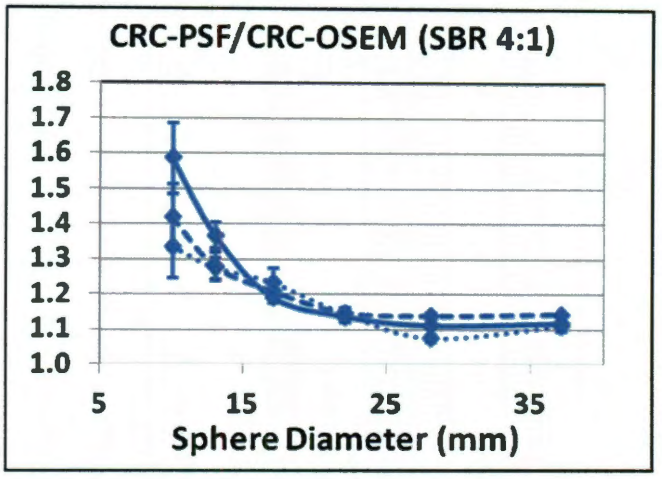

(c)

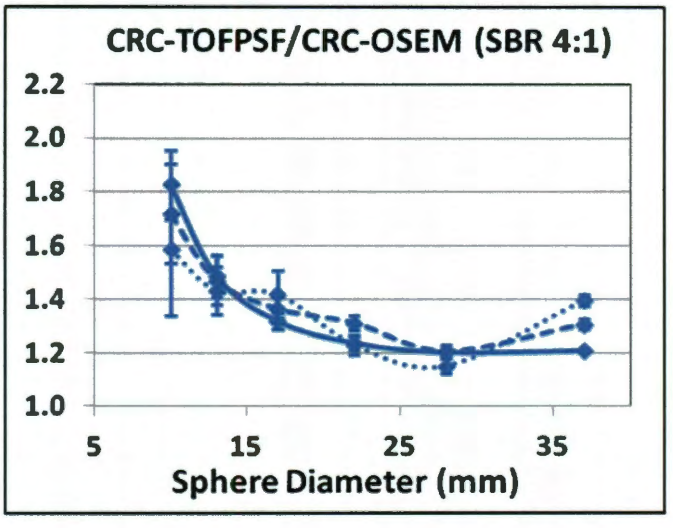

Figure 3.7: The CRC improvement (CRC-TOF, PSF, TOFPSF / CRC-OSEM respectively) vs. sphere diameter using the derived optimal iteration shown in table 3.1.

this figure correspond to hot CRCs (equation (3.3)), while the 2 largest spheres correspond to cold CRCs (equation (3.4)). The improvement in hot CRC for TOF as compared to OSEM is not significant (<15%) and is rather constant with different phantom (10±4% and 12±8% for small and large phantom) and sphere sizes (13±10% and 10±2% for 10mm and 22mm sphere). On the other hand, the improvement in CRC for the small sphere (10mm) when using PSF is significant (45% higher) (figure 3.7(b)) and an additional increase can be achieved when using TOFPSF (figure 3.7(c)). Figure 3.7 also shows that more improvements can be achieved in cold spheres for TOF of larger phantoms. PSF on the other hand does not show a similar trend. Figure 3.8 shows the

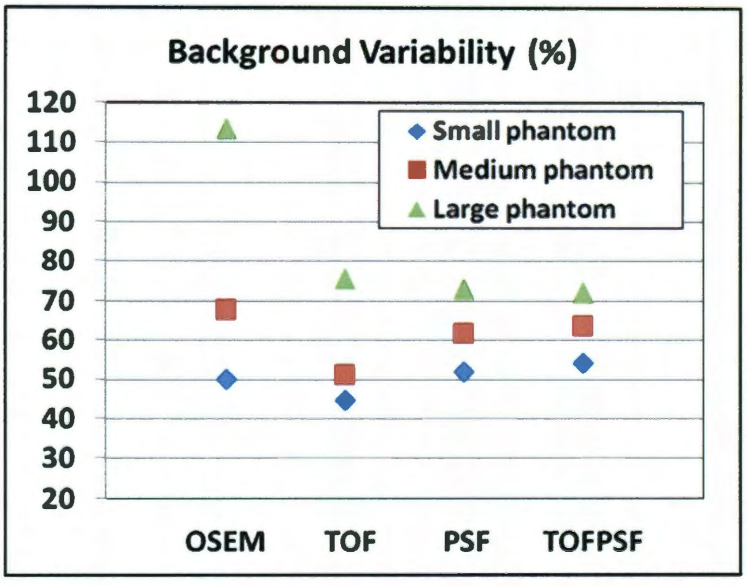

Figure 3.8: The background variability for SBR 4:1 for each phantom and reconstruction algorithm.

background variability for SBR 4:1 for each phantom and reconstruction algorithm at optimal iterations. TOF results in smallest background noise for small and medium phantoms, while TOFPSF leads to the smallest background noise for large phantom.

Effect of scan duration. Figure 3.9 shows SNR improvement vs. sphere diameter, when using TOF, PSF, TOFPSF for 1 or 2min data, compared to OSEM of 3min data. The average gains in SNR over all sphere sizes for TOF, PSF, TOFPSF of 2 min data were 3±8%, 7±12%, 15±14% for the small phantom; 24±11%, 15±13%, 32±13% for the medium phantom; and 34±12%, 58±18%, 84±17% for the large phantom respectively. 1 min data result in lower SNR than 3 min OSEM data except for the largest phantom. For the largest phantom, however, 1min TOF, PSF, and TOFPSF result in a gain of -8±15%, 11±20%, 25±21% SNR compared to 3min OSEM. Figure 3.10 shows the same results but calculated for CRC. The figure shows that the difference between 1 and 2min data are small, and 1min data could always result in similar or higher CRC as compared to OSEM acquired for 3min.

(a)

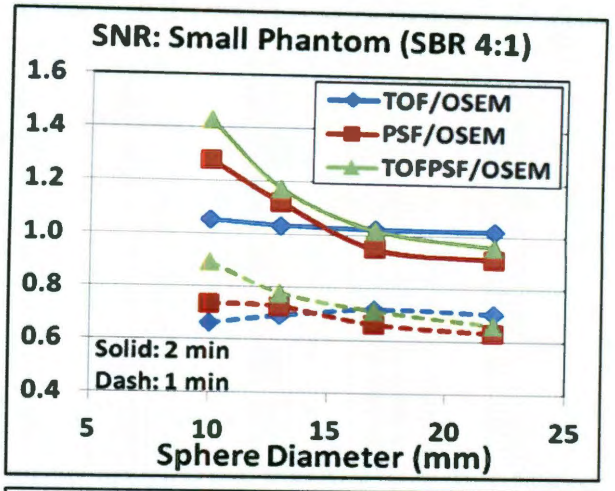

(b)

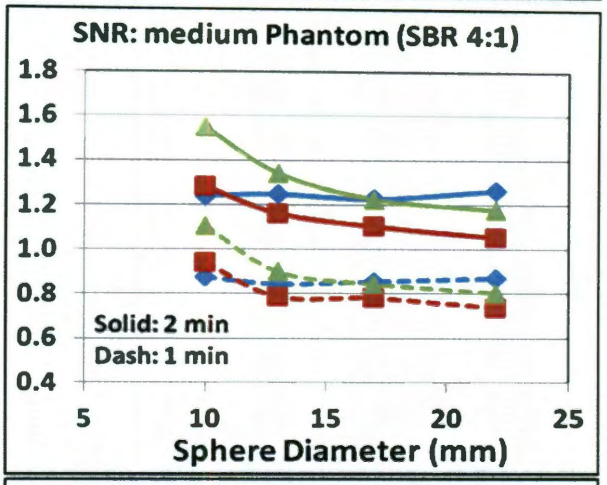

(c)

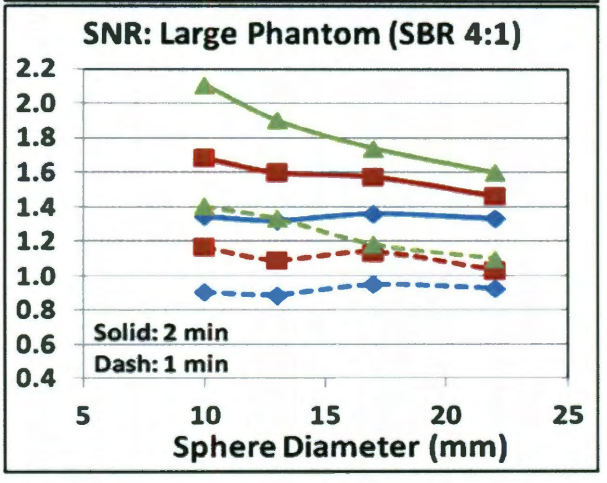

Figure 3.9: SNR improvement vs. sphere diameter using TOF, PSF, TOFPSF on 1 or 2min data, and OSEM on 3min data.

(a)

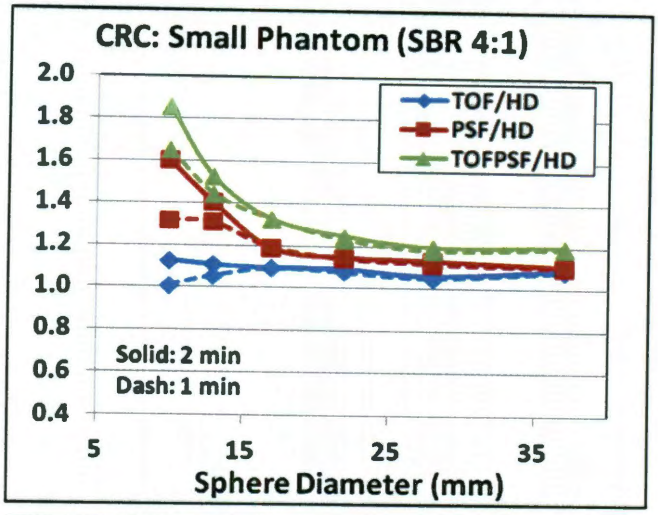

(b)

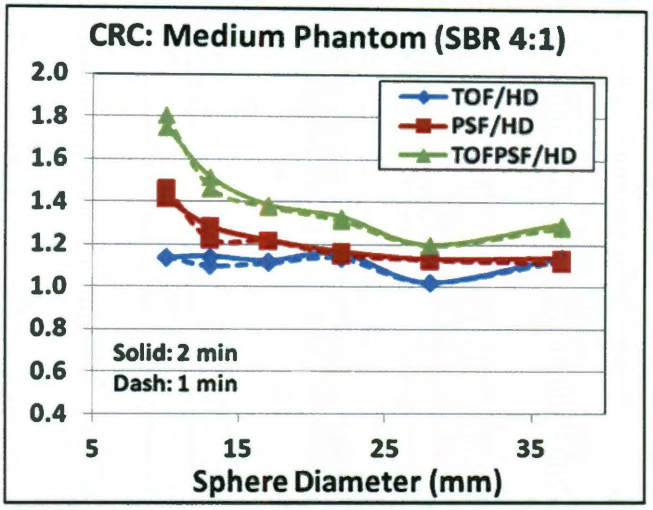

(c)

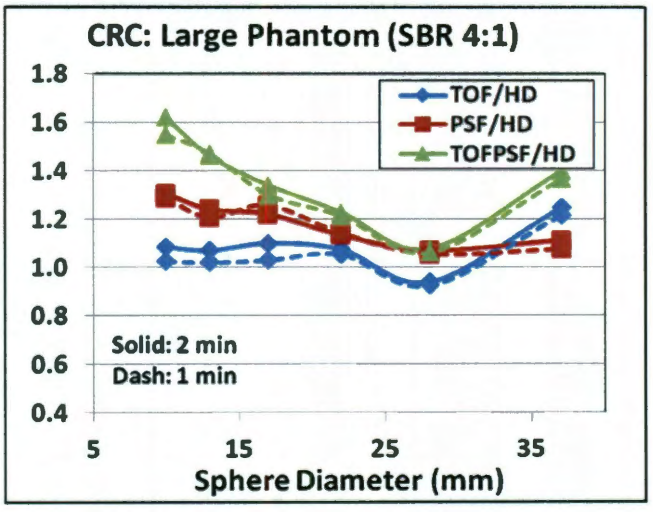

Figure 3.10: CRC improvement vs. sphere diameter using TOF, PSF, TOFPSF on 1 or 2min data, and OSEM on 3min data.

3.4 Discussion

The aim of this paper is to provide a comprehensive assessment of the image quality on a TOF PET/CT scanner. Phantoms with different sizes corresponding to different patient BMI were fitted with varying sphere sizes and SBRs. Data were then reconstructed using OSEM, TOF, PSF and TOFPSF and the image quality was evaluated in terms of SNR, CRC, and background noise. The major difference of this study with previously published papers on TOF evaluation is to perform an optimization of the iterations for different object size and reconstruction algorithm, and then compare the image quality, rather than doing a comparison based on using the same iteration.

In general, our results in image quality analysis following optimization are different with those derived in previous papers using the same reconstruction parameters for both TOF and non-TOF. Our results showed a much lower background noise for TOF as compared to non-TOF (figure 3.8), while previous papers showed a higher noise level for TOF (*121,125*). Furthermore, our results showed a little improvement in TOF hot CRC (<1.15 as shown in figure 3.7(a)), while previous study derived a much higher improvement (*122*). Moreover, our SNR results showed a remarkable improvement in TOF SNR (figure 3.6(a)), which is higher than previously reported of ~1.1 in SNR-TOF/SNR-nonTOF (*123*). Finally, our results suggest that 2 min TOF could replace 3 min non-TOF, which was longer than previously reported (*124,125*).

The optimal iteration number was determined based on 95% convergence in mean SUV of the hot 10 mm sphere for the SBR 4:1. The 10 mm sphere is the smallest sphere in this study and thus has the slowest convergence rate. The iteration corresponding to the convergence for the 10 mm sphere was chosen since it ensures convergence of all other

spheres. In clinical studies, such an iteration number would ensure that the SUVs of tumors of 10 mm or larger have reached convergence. A SBR of 4:1 was selected since a majority of lesions show a >4:1 SBR (SUV greater than ~4 is considered malignant). A 256×256 matrix size was used with a 50 cm transaxial FOV (pixel size=2 mm), in order to have several voxels in the VOI used for calculating the SUV mean for the 10mm sphere, thereby providing better statistics and more reliable results. In real patient studies, a 192×192 matrix size with a 70 cm FOV will be used (3.6 mm pixel). To ensure similar performance between this study and clinical settings, we reconstructed some of the phantom data using these parameters and found a similar trend in the convergence rate but with larger error bars.

The optimization results in table 3.1 show that the convergence rate TOF > OSEM > TOFPSF > PSF, and that a faster convergence is achieved for smaller phantoms as expected. Moreover, more iterations are needed for PSF/TOFPSF as compared to OSEM/TOF in order to achieve convergence, and generate PET images with higher mean SUV for small tumors (figure 3.2). Furthermore, our results show that the mean SUV for PSF/TOFPSF is much higher as compared to TOF in small tumors, as can be seen in figure 3.11 particularly due to correction of partial volume effect. Furthermore, the noise increment per iteration for PSF/TOFPSF is smaller compared to OSEM/TOF (figure 3.11), due to the fact that PSF modeling introduces correlations between neighboring voxels in a manner similar to smoothing filters (*130*). Therefore the large iteration numbers for PSF/TOFPSF only result in a slightly higher noise level in PET images as compared to OSEM/TOF for the small and medium phantom (figure 3.8).

(a)

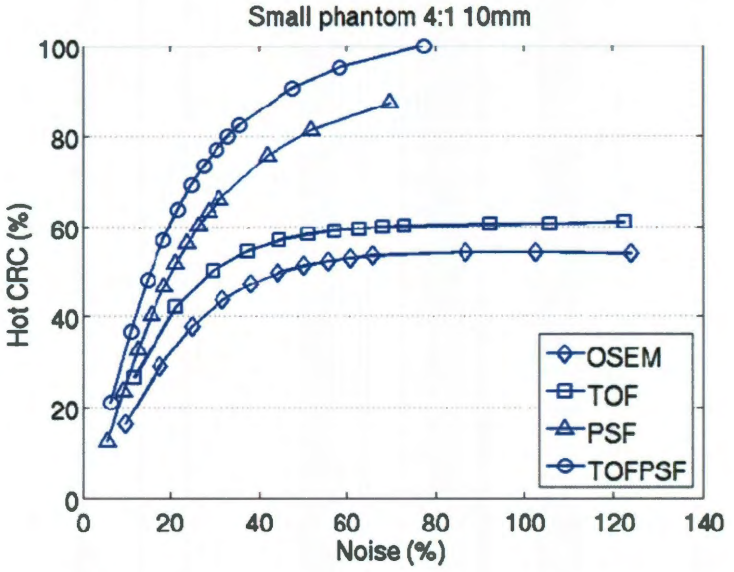

(b)

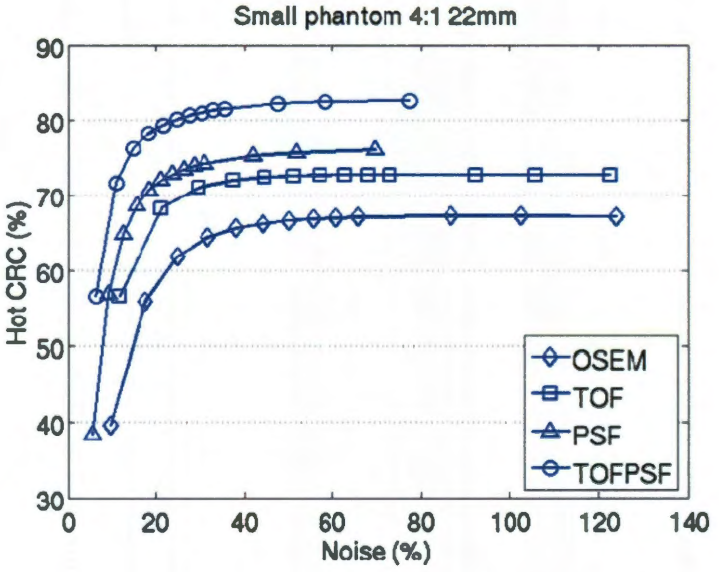

Figure 3.11: CRC vs. noise in small phantom, SBR 4:1, for 10 and 22 mm sphere respectively.

Table 3.2 shows the reconstruction times required for each algorithm for 5, 10 and 20 iterations respectively. The results suggest that OSEM/PSF require less than half of the processing time needed for TOF/TOFPSF. In this regard, using TOFPSF with iterations shown in table 3.1 will result in a relatively long processing time, which might

not be feasible in the clinic. An alternative approach to be considered, if quantification of tumors is not the primary concern, is to use a small number of iterations for TOFPSF reconstruction. For example, if using 5 iteration for TOFPSF instead of 18 as shown in table 3.1 on the SBR 4:1 small phantom, resultant PET images and a comparison of image quality are shown in figure 3.12. The smaller number of iterations results in a significantly decreased reconstruction time and background noise, however at the expense of a lower SUV mean for the smallest 10 mm sphere.

Table 3.2: Reconstruction time for each algorithm

	OSEM	TOF	PSF	TOFPSF
5 iteration	1 min	4 min	1.5 min	4 min
10 iteration	1.5 min	7 min	2 min	7.5 min
20 iteration	2.5 min	13 min	3 min	14 min

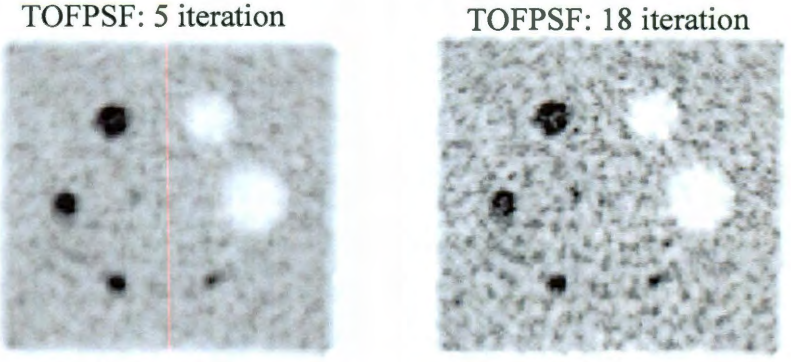

SUV mean of 10mm sphere (Measured/True)	0.74	0.97
Background noise	22%	54%
Reconstruction time	4 min	12.5 min

Figure 3.12: PET images of 5 and 18 iteration for TOFPSF in small phantom with SBR 4:1, and a comparison in image quality and reconstruction time.

The improvement of TOF, PSF, and TOFPSF with respect to OSEM on image quality was assessed using the derived optimal iterations shown in table 3.1. Figure 3.6 shows that the improvement in SNR increases with the increasing phantom sizes as expected. However the improvements in SNR for TOF are relatively similar among different sizes of spheres. For PSF and TOFPSF, the improvement decreases with increasing sphere sizes, since PSF corrects for the partial volume effect, which is more significant for small tumors. The average SNR-TOF/SNR-OSEM was 1.23, 1.49 and 1.66 for the small, medium and large phantom respectively. Such a result is consistent with the relationship (*131*):

$$(SNR_{TOF} / SNR_{OSEM})^2 \propto D / \Delta d \tag{3.6}$$

where D is the diameter of the object, calculated as

$$D = 2 \cdot \sqrt{\frac{transaxial\ area}{\pi}} \tag{3.7}$$

in our study. Δd is the error in localization, and is due to the error in timing resolution, Δt (650ps), calculated using equation (3.1). Figure 3.13 shows $(SNR_{TOF} / SNR_{OSEM})^2$ vs.

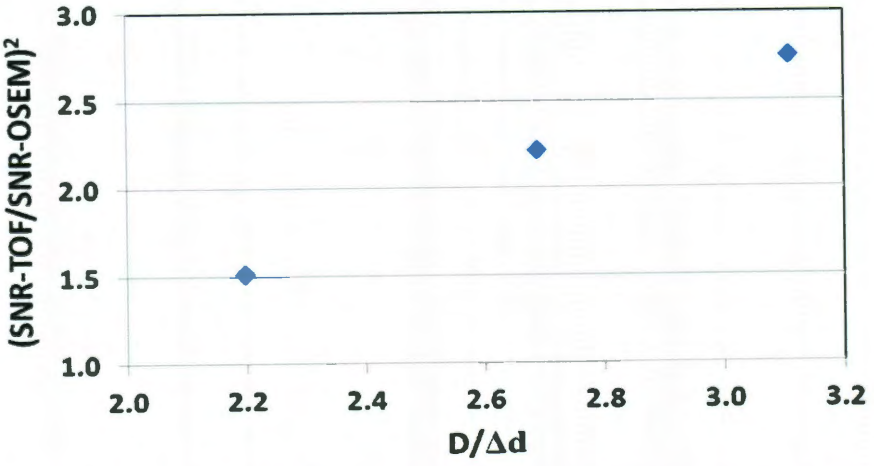

Figure 3.13: Square of the SNR_{TOF} to SNR_{OSEM} ratio vs. D/Δd for the three phantoms.

$D / \Delta d$ for the three phantoms of SBR 4:1 used in this study, and a linear relationship can be found in the figure.

TOF and PSF have different characteristics in hot and cold CRC respectively. PSF results in more improvement as compared to TOF in hot CRC, while TOF is better in cold CRC as shown in figure 3.7, which are similar with previous findings. Using the iterations in table 3.1, TOF results in a significantly less background noise ($p<5\%$) compared to other algorithms for the small and medium phantom, while PSF & TOFPSF has significantly less background noise (compared to OSEM and TOF) for the large phantom ($p<5\%$) (figure 3.8). On the other hand, figure 3.11 shows that for the same iterations, PSF<TOFPSF<OSEM<TOF in image noise. In this regard, the very large iteration numbers used in PSF and TOFPSF to reach convergence compared to TOF in the small and medium phantom is the main reason of its larger image noise. However, for large phantom, PSF/TOFPSF finally achieved less image noise as compared to TOF.

The results of the reduced acquisition time (figure 3.9) suggest that for patients with small and medium sizes, 1 minute TOF, PSF and TOFPSF reconstructions always resulted in worse SNR while 2 minutes had similar or higher SNR. On the other hand, for very large patient, 1 minute TOF, PSF or TOFPSF data could result in similar SNR to the 3 min OSEM images. Furthermore, the difference in CRC between 1 and 2 minutes for each algorithm are small (figure 3.10), and suggest that CRC is not sensitive when decreasing acquisition time, however SNR is quite sensitive to the acquisition time (figure 3.9).

3.5 Conclusion

Optimization of acquisition and reconstruction parameters for different object sizes and reconstruction algorithms have been derived for a TOF PET/CT scanner based on the convergence of SUV. Image quality has been compared between OSEM, TOF, PSF and TOFPSF after optimization. Such results could be used as guidance for clinical studies on this TOF PET/CT scanner.

Chapter 4

Investigating the Use of Non-attenuation Corrected PET Images for the Attenuation Correction of PET Data in PET/MR Systems

4.1 Background and Motivation

PET imaging is widely used in clinical oncology to facilitate patient diagnosis in a wide variety of cancers (*132-134*). In addition to provide qualitative measurement, PET can also provide quantitative analysis of the radioactive tracer concentration by calculating the standardized uptake value (SUV) (*135*). This also enables the use of PET for evaluation of the response to cancer therapy (*136*), and kinetic modeling of tracer uptake (*137*). In order to achieve an accurate quantitative measurement of the PET tracer distribution, several correction techniques have to be applied, including the attenuation correction (AC) of gamma photons using attenuation maps. In current PET imaging, AC is often performed by an additional CT scan by the hybrid PET/CT scanners. CT image shows the electronic density of body tissues. Then the CT Hounsfield units can be bilinearly transformed to tissue attenuation coefficient at the energy of gamma photons at 511 keV (*138,139*).

PET/MR hybrid imaging has recently been introduced as a new multimodality imaging device that has gathered a widespread clinical interest (*140,141*). MR imaging shows advantages over CT because of its high soft tissue contrast and its ability to assess functional parameters and physiological processes without X-ray radiation. However,

MR signal is not related to the electronic density of biologic tissue, therefore MR data cannot be transferred to tissue attenuation coefficient directly. In this regard, one challenge of this multimodality imaging device is how the AC of the PET data is performed. Currently several techniques have been proposed to rely on the use of the MR to either segment MR image into different tissue types and assign corresponding attenuation coefficients (*142,143*), or to use representative anatomical atlas registration to yield an attenuation map (*144*). Nevertheless, MR-guided attenuation correction still remains challenging for whole-body imaging, which includes attenuation of MR hardware (*145*), positioning aids in the field-of-view (FOV) (*146*), and truncation in the transverse plane owing to the limited size of the MR FOV (*147*).

The aim of this paper is to investigate the feasibility of using the non-attenuated PET images (PET-NAC) as a means for the AC of PET data in the PET/MR systems. Similar ideas were first proposed in the 1990s when there was no PET/CT hybrid scanner. Several techniques have been suggested at that time to use PET-NAC only during the image reconstruction. These techniques can be divided into two classes. One class of algorithms applies segmentation algorithms to the emission sinograms or uncorrected emission images to locate regions of approximately constant attenuation, to which predefined attenuation coefficients can be assigned (*148*). The other class of algorithms attempts to extract information on the attenuation coefficients directly from the emission data by iterative inversion of the forward mathematical model using likelihood optimization, and simultaneous reconstruction of attenuation and activity (*149*). However, such techniques were not preferred at that time and a transmission scan was often acquired in addition to the emission scan to perform attenuation correction. Later in the

1990s such problem was resolved by using a CT scan and PET/CT scanner has been introduced. However, current interest in PET/MR imaging could re-apply these ideas of using PET-NAC for the AC of PET data in PET/MR systems. This paper proposed and assessed an iterative segmentation approach, which could segment PET-NAC into three tissue types (background air, soft tissue, and lung) and then create an attenuation map for PET reconstruction. Such an approach can potentially be an alternative method of MR-based AC in PET/MR imaging.

4.2 Materials and Methods

Iterative segmentation approach

The PET-NAC images were used to create an attenuation map with three tissue types: background air, soft tissue, and lung. Three steps were involved in this iterative segmentation process.

STEP 1: Body segmentation. The patient body contour is segmented from the PET-NAC image in STEP 1. An active contour model is used in this step (*150*), and models the contour as a mapping function from an interval [0, 1] to a 2D space:

$$v(s) = (x(s), y(s)), \qquad s \in [0,1] \tag{4.1}$$

where v is a mapping function , s is the independent variable, and (x, y) is the location of a resulting contour point. The energy function of this contour is defined as

$$E = \int_0^1 E_{\text{int}}(v(s)) + \kappa E_{ext}(v(s))\, ds \tag{4.2}$$

where

$$E_{\text{int}}(v(s)) = (\alpha|v'|^2 + \beta|v''|^2)/2 \tag{4.3}$$

is the internal energy depending on the first-order term controlled by α and a second-order term controlled by β. $E_{ext}(v(s))$ is the external energy of the contour associated with images via their gradient magnitude and pixel intensity, and weighted by κ.

The contour searching process reaches equilibrium when internal and external forces are balanced, which corresponds to a local minimum of the energy E in equation (4.2). This minimizing gives rise to the following Euler equation

$$-\alpha v'' + \beta v'''' + \kappa \nabla E_{ext} = 0 \tag{4.4}$$

As the model is implemented in discrete format, equation (4.4) becomes a finite difference equation

$$-\alpha(v_{i-1} - 2v_i + v_{i+1}) + \beta(v_{i-2} - 4v_{i-1} + 6v_i - 4v_{i+1} + v_{i+2}) + \kappa \nabla E_{ext}\big|_{v=v_i} = 0 \tag{4.5}$$

Let

$$\nabla E_{ext}\big|_{v=v_i} = \left(\frac{\partial E_{ext}(v_i)}{\partial x_i}, \frac{\partial E_{ext}(v_i)}{\partial y_i}\right) = (f_x(x_i, y_i), f_y(x_i, y_i)) \tag{4.6}$$

Equation (4.5) can then be written is matrix form as

$$Ax + \kappa f_x(x, y) = 0 \tag{4.7}$$

$$Ay + \kappa f_y(x, y) = 0 \tag{4.8}$$

where A is a pentadiagonal banded matrix determined by α and β.

To solve equations (4.7) and (4.8) iteratively, a product of a step size and the negative time derivatives are introduced to the right-hand side. The resulting equations are

$$Ax_t + \kappa f_x(x_{t-1}, y_{t-1}) = -\gamma(x_t - x_{t-1}) \tag{4.9}$$

$$Ay_t + \kappa f_y(x_{t-1}, y_{t-1}) = -\gamma(y_t - y_{t-1}) \tag{4.10}$$

where γ is a step size. At equilibrium, the time derivative vanishes and they become equations (4.7) and (4.8). Rearranging equations (4.9) and (4.10), the solution of the contour points at iteration t is

$$x_t = (A + \gamma I)^{-1}(\gamma x_{t-1} - \kappa f_x(x_{t-1}, y_{t-1})) \tag{4.11}$$

$$y_t = (A + \gamma I)^{-1}(\gamma y_{t-1} - \kappa f_y(x_{t-1}, y_{t-1})) \tag{4.12}$$

Using this model, searching for the contour from an image is an optimization process from an initial contour. This model is performed on 2D image, and has to be repeated for each axial 2D slice of PET-NAC. An initial contour has to be drawn manually on the first slice, and then the optimized contour of the previous slice can be used as the automatic initial contour for the next slice. One contour is needed in the human torso region. However, in the legs region, or head & neck region with arms up, more than one contour has to be performed for each slice.

After the contouring process, voxels inside the segmented body contour are then assigned a value of 0.096 cm^{-1} to represent the attenuation coefficient of soft tissue at 511 keV. This segmented attenuation map is then used to attenuate correct and reconstruct the raw PET data. The resulting PET-AC images are then used as the input to the STEP 2 of the iterative process.

STEP 2: Lung segmentation. The lung region is segmented from the resultant PET-AC from STEP 1. First a starting and ending slice are determined manually from

this PET-AC which include the whole lung region. A threshold is then calculated and used to segment the lung region on PET-AC. The threshold is determined by an optimal thresholding approach from the image intensity distribution (*151*) of the lung parts on PET-AC from STEP 1.

Suppose $p(i)$ is the intensity distribution of a digital image in the range [1, L]. A threshold $k \in [1, L]$ divides the image into two classes $C_1([1,\cdots,k])$ and $C_2([k+1,\cdots,L])$. Then the following statistics can be calculated: the probabilities of first and second class: $\omega_1(k)$ and $\omega_2(k)$; the mean value of first and second class: $i_1(k)$ and $i_2(k)$; variances of first and second class: $\sigma_1^2(k)$ and $\sigma_2^2(k)$; and the mean of the entire image: $i_T(k)$.

Then the optimal thresholding formulation is written as

$$T(k) = \frac{\log[v(k)+1]}{J(k)} \tag{4.13}$$

where

$$v(k) = \omega_1(k)[i_1(k) - i_T(k)]^2 + \omega_2(k)[i_2(k) - i_T(k)]^2 \tag{4.14}$$

$$J(k) = \omega_1(k)\log\left\lceil\frac{\sigma_1(k)}{\omega_1(k)}\right\rceil + \omega_2(k)\log\left\lceil\frac{\sigma_2(k)}{\omega_2(k)}\right\rceil \tag{4.15}$$

A single maximum for $T(k)$ can always be found, and the corresponding k is defined as the optimal threshold.

The resultant voxel intensities that are greater than the optimal threshold k were considered to be lung tissue and were updated by a value of 0.024 cm^{-1} representing the attenuation coefficients of lung tissue at 511 keV. The updated attenuation map was then

used for a second time to attenuate correct and reconstruct the raw PET data, and the resulting PET-AC images were used as the input to the STEP 3 of the iterative process.

STEP 3: Modification. The purpose of STEP 3 is to delineate parts of the heart and liver from the lung contour (red contour in figure 4.1) using a region growing approach (*152*) since these parts were unavoidably included in the lung region derived from STEP 2.

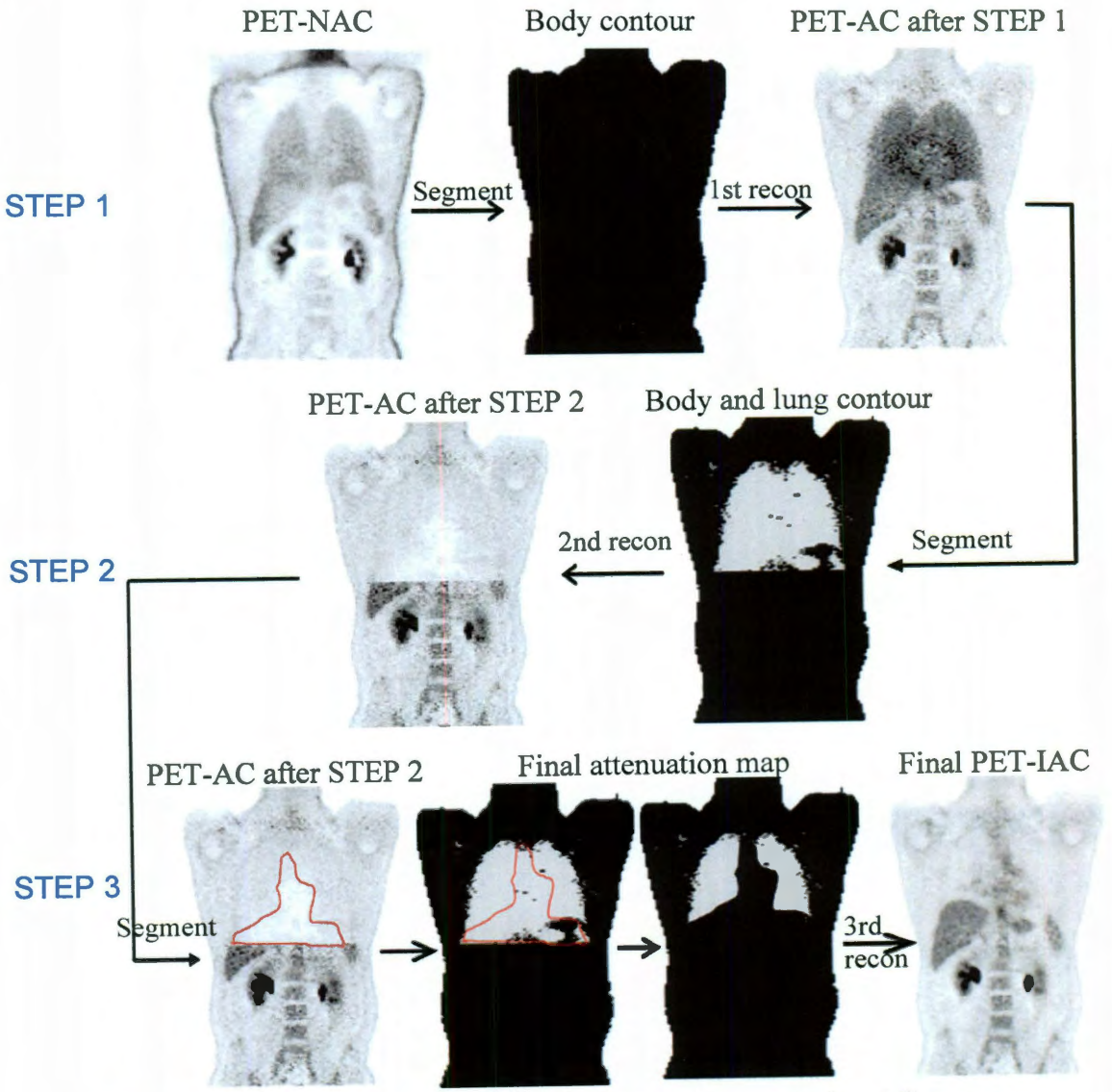

Figure 4.1: The flow chart of the whole iterative segmentation AC process.

A 3D region growing technique is applied based on a pre-selected seed point. The region is iteratively grown by comparing all unallocated neighboring pixels to the region. The difference between a pixel's intensity and the region's mean intensity is used as a measure of similarity. The pixel with the smallest difference measured this way is allocated to the region. This process stops when the intensity difference between region mean and new pixel intensity becomes larger than a certain threshold. The final grown region was then corrected by using a value of 0.096 cm^{-1} in the attenuation map. In addition, voxels in the lung region with SUVs greater than 1.5g/cc were considered to be lung tumors and were also modified by 0.096 cm^{-1} in this step.

Finally the attenuation coefficients of the scanner couch were included based on the CT images to eliminate the impact of the couch on the accuracy of AC. The final attenuation map was then used to AC the raw PET data and result in a final PET image (PET-IAC). A flow chart of the whole iterative segmentation AC process is shown in figure 4.1.

Phantom and Patient Studies

A water fillable torso phantom with hollow spheres was scanned on a GE Discovery-RX PET/CT scanner. The specifications of this scanner can be found in (*153*). The activity concentration in the phantom spheres and background was 37.2 and 6.27 kBq/cc respectively. A PET scan was acquired in 3D mode using 2 FOV with 5 minutes per FOV. CT-attenuation corrected PET (PET-CTAC), PET-NAC, and CT images were generated following the data acquisition using the standard scanner software. In addition

the PET-NAC images were used to create an attenuation map through the proposed iterative segmentation process and resulted in PET-IAC.

In addition, ten patients were scanned on the same PET/CT scanner. Each patient study was acquired in 6 axial FOV with 3 minutes per FOV. PET-CTAC, PET-NAC, and CT images were generated for each patient using the standard scanner software. Then PET-IAC was generated for each patient from the iterative segmentation process.

To evaluate the proposed segmentation approach, visual inspection was performed comparing PET-IAC and PET-CTAC. The SUV differences between PET-IAC and PET-CTAC were also performed by calculating 2D histograms of SUV in PET-CTAC over the SUV in PET-IAC. In addition, the tumors' SUV max was compared between PET-IAC and PET-CTAC to assess the accuracy of tumor quantification.

4.3 Results

Figure 4.2(a) shows an axial slice of the PET-NAC of a patient. The body contour after STEP 1 of the iterative segmentation approach is shown in figure 4.2(b). Figure 4.2(c) shows the CT image for comparison. The figures show that the derived body contour is very similar to that shown on the CT image.

Figure 4.3(a) shows the same slice of the reconstructed PET-AC after STEP 1 for the same patient. Figure 4.3(b) shows the image intensity histograms of the lung region on this PET-AC, as well as the corresponding $T(k)$ calculated from the optimal thresholding approach (equation (4.13)). The maximum of $T(k)$ achieves at k=2300, which was then determined as the optimal threshold to segment lung region on figure 4.3(a). The resulting attenuation map is shown in figure 4.3(c). Comparing figures 4.3(c)

and the CT image shown in figure 4.2(c), this map accurately shows the outer contour of the lung region, however it also includes other tissues (e.g. trachea) not belong to lung.

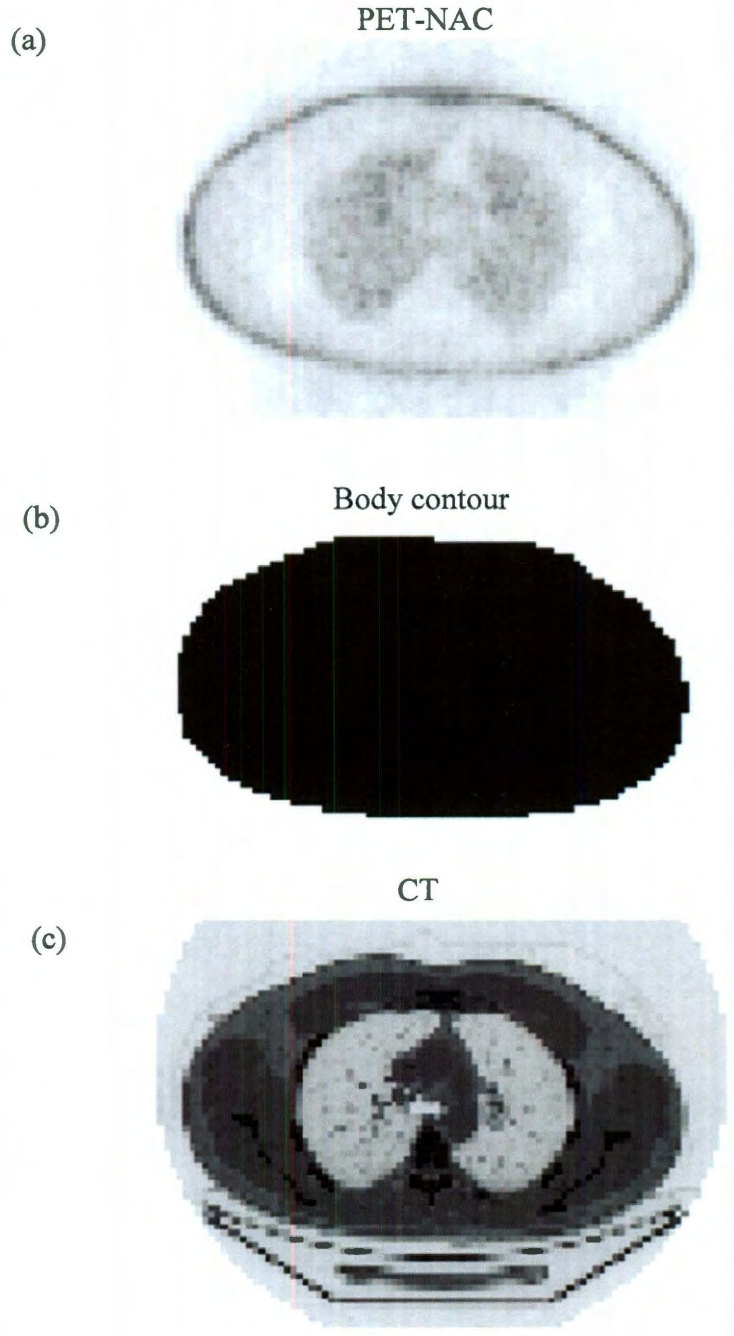

Figure 4.2: An axial slice of (a) PET-NAC, (b) body contour after STEP 1, and (c) reference CT image of a patient.

(a)

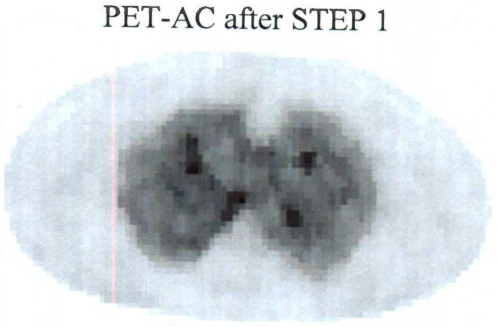

(b)

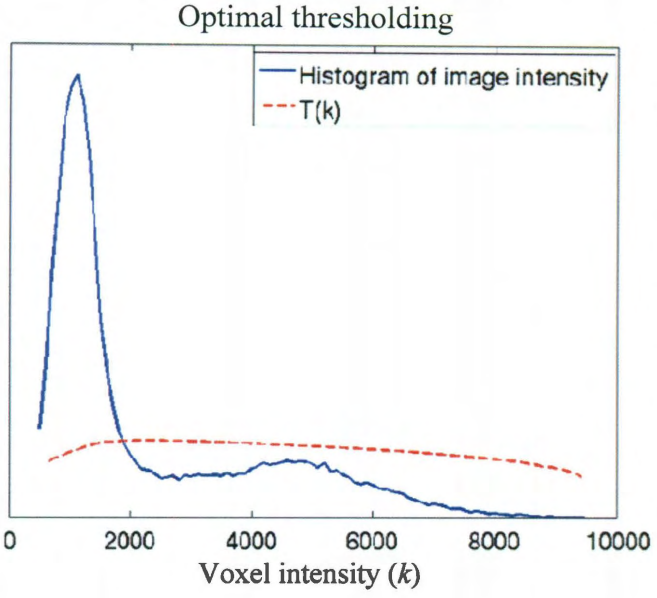

(c)

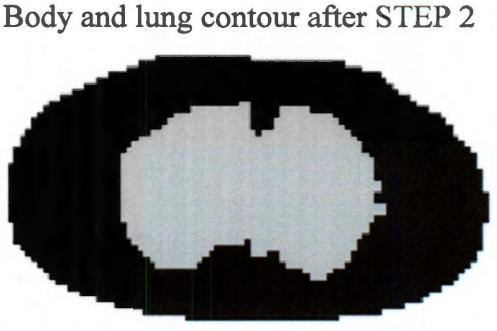

Figure 4.3: (a) An axial slice of PET-AC after STEP 1, (b) image intensity histogram, and (c) body and lung contour in the STEP 2.

Figure 4.4(a) shows the reconstructed PET-AC after STEP 2. The region growing technique in STEP 3 of the iterative segmentation approach results in the region inside the red contour. This region is then added to the attenuation map from STEP 2 (figure 4.4(b) or 4.3(c)), and finally results in the modified attenuation map (figure 4.4(c)). Figure 4.4(c) looks very similar to the CT image shown in figure 4.2(c), showing the feasibility of the proposed iterative segmentation approach.

(a) PET-AC after STEP 2

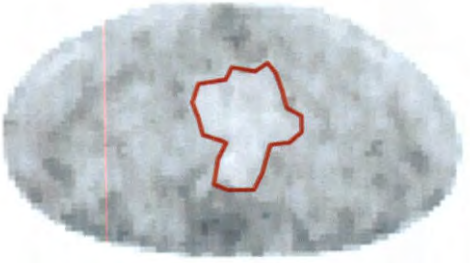

(b) Body and lung contour after STEP 2

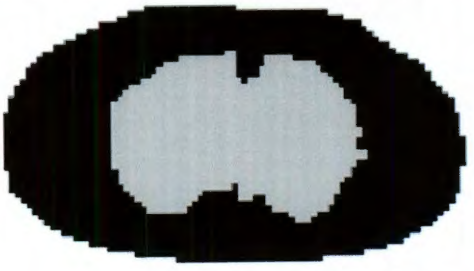

(c) Final attenuation map

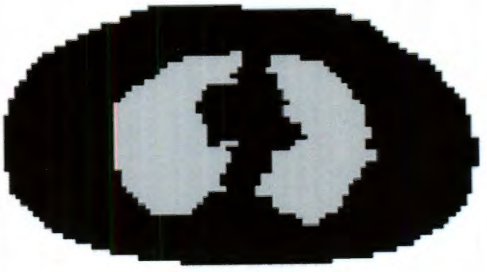

Figure 4.4: An axial slice of (a) PET-AC after STEP 2, (b) body and lung contour in the STEP 2, and (c) final attenuation map in the STEP 3.

Figure 4.5 shows a coronal slice of CT, PET-NAC, attenuation maps generated from proposed approach and CT, PET-IAC, and the reference PET-CTAC of the torso phantom. By visual inspection, the body contour and lung region in the attenuation map derived from PET-NAC looks similar to that derived from CT. However, the details in the lung structure are missing in our approach, and also there is a small difference between the PET-IAC and PET-CTAC. A comparison of the SUVs of the 6 hot spheres in the phantom between PET-IAC and the PET-CTAC are shown in table 4.1. PET-IAC SUVs are on average equal to 103±9% compared to the SUVs from the PET-CTAC.

Table 4.1: SUV max of the spheres in the phantom

Sphere #	PET-CTAC	PET-IAC	% difference
1	4.0	4.4	9%
2	2.5	2.3	-7%
3	1.4	1.5	9%
4	2.8	3.0	10%
5	2.9	2.6	-10%
6	5.0	5.3	6%
			Average 3±9%

Figure 4.6 shows the same images as in figure 4.5 for one patient. Visual inspection, shows a quite accurate body contour, and a reasonable lung region in the attenuation map derived from PET-NAC as compared to reference attenuation map. Also there is very small difference between PET-IAC and PET-CTAC. Table 4.2 shows the SUVs of 5 tumors in this patient (tumor #2 is shown on figure 4.6). PET-IAC SUVs are on average 109±3% as compared to the PET-CTAC SUVs. Figure 4.7 and table 4.3 are images and tumor quantification comparison for the other patient. Figures for the other 8 patients are not shown. However, for all the 10 patients, PET-IAC tumor SUVs were on average equal to 110±8% compared to the SUVs from the PET-CTAC.

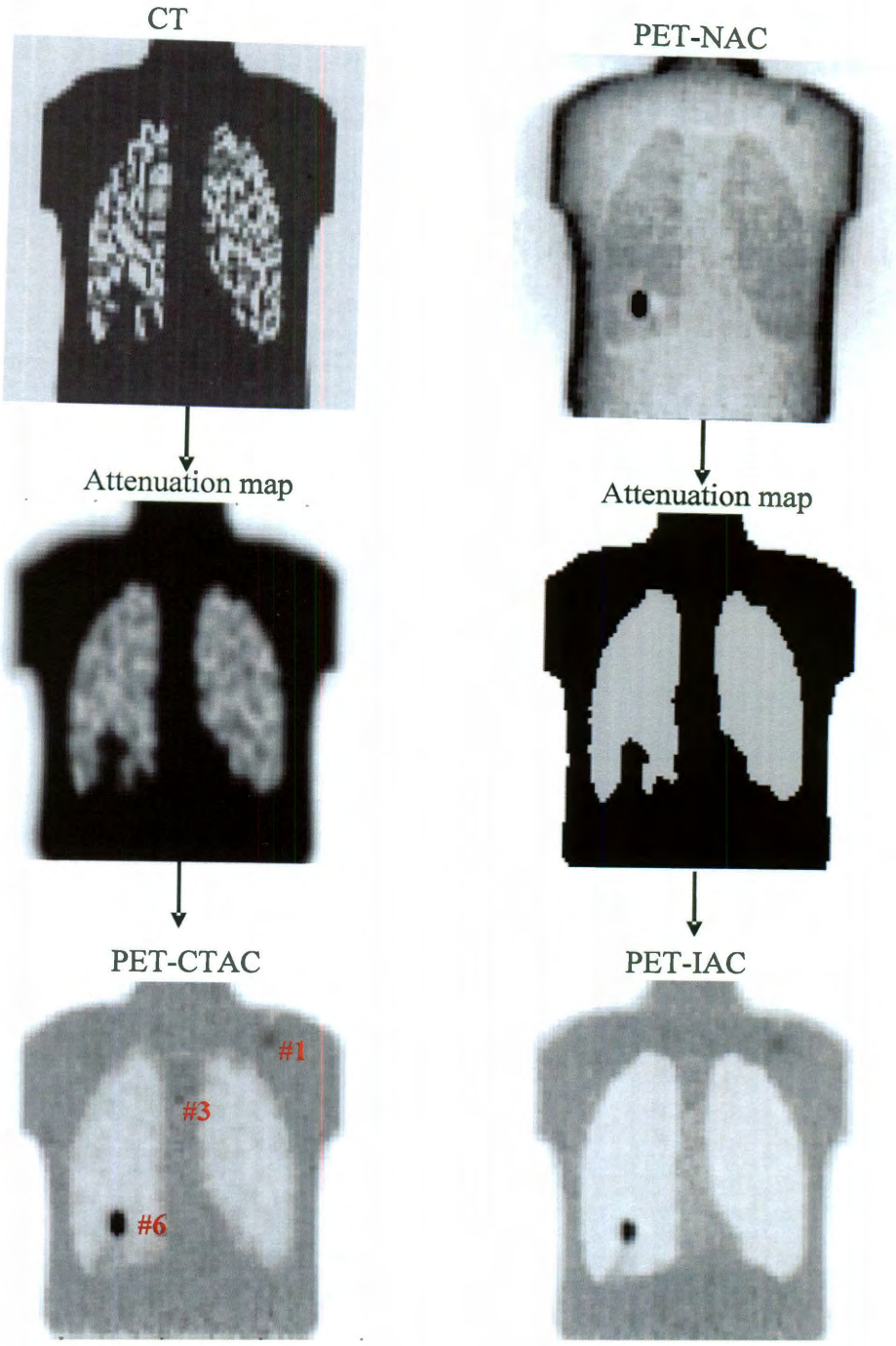

Figure 4.5: Comparison between PET-CTAC and PET-IAC of the torso phantom.

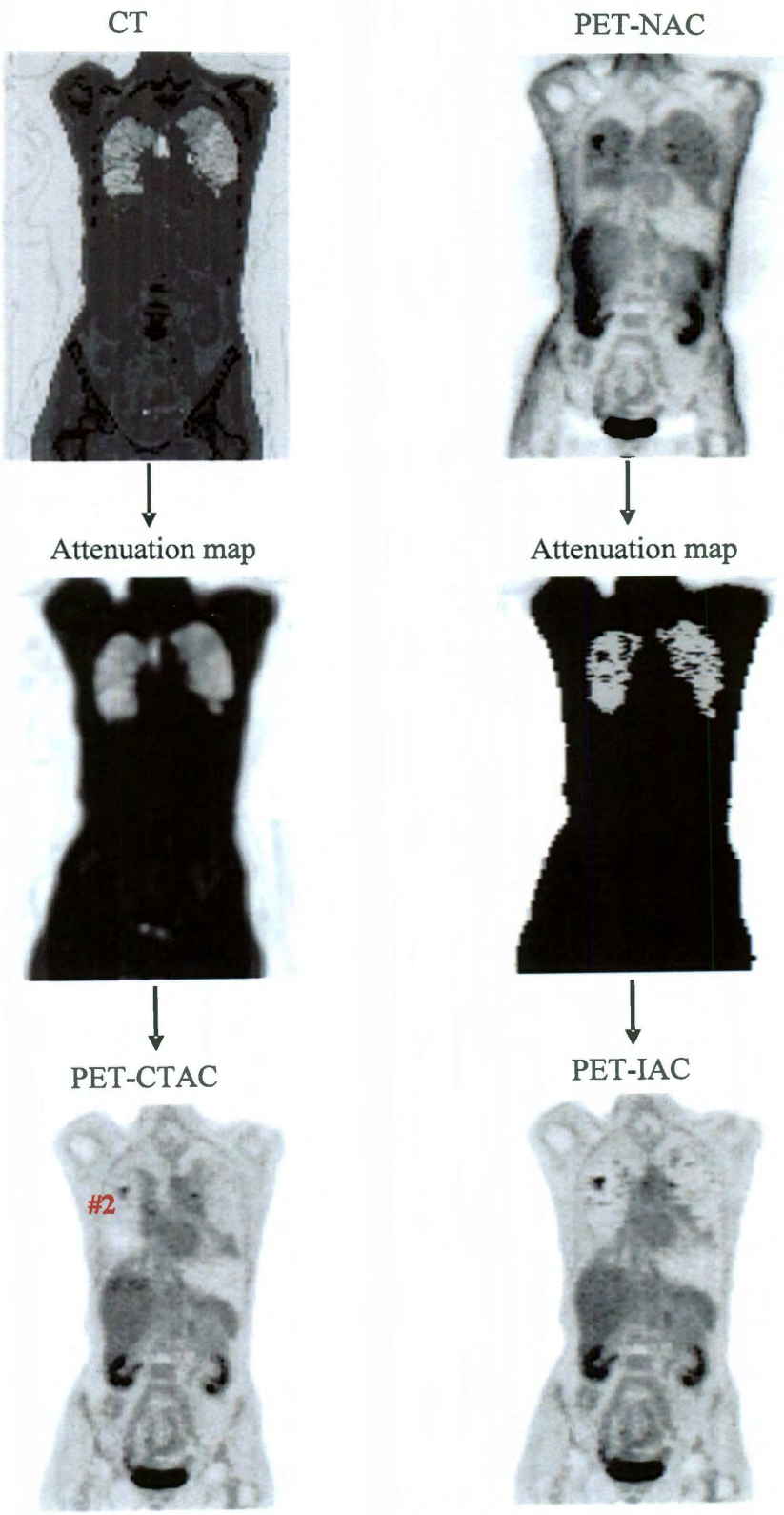

Figure 4.6: Comparison between PET-CTAC and PET-IAC of a patient.

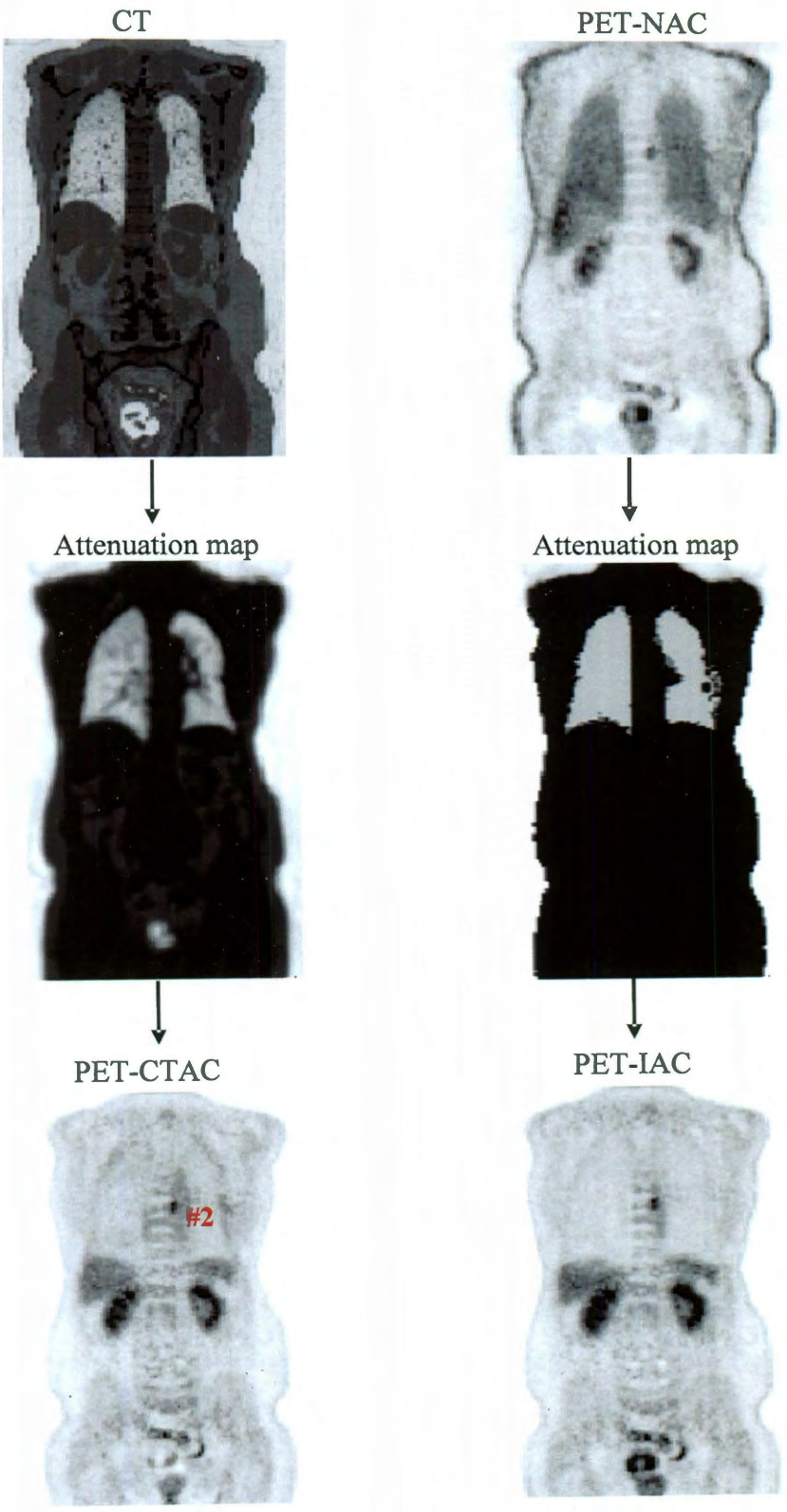

Figure 4.7: Comparison between PET-CTAC and PET-IAC of another patient.

Table 4.2: SUV max of the tumors in a patient

Tumor #	PET-CTAC	PET-IAC	% difference
1	2.7	3.0	11%
2	2.6	2.9	11%
3	2.8	3.1	9%
4	3.9	4.3	9%
5	5.3	5.5	4%
			Average 9±3%

Table 4.3: SUV max of the tumors in another patient

Tumor #	PET-CTAC	PET-IAC	% difference
1	3.7	3.6	-2%
2	3.5	3.6	2%
3	6.2	6.4	4%
4	6.3	6.3	1%
			Average 1±3%

Figure 4.8 shows the histogram (H) of SUV in PET-CTAC vs. SUV in PET-IAC for a patient. $\sqrt[10]{\frac{H}{N}}$ is plotted in this figure instead of H to increase the contrast at lower

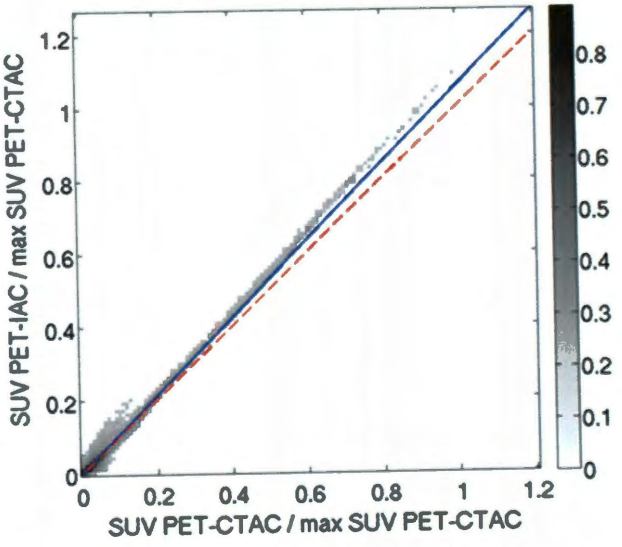

Figure 4.8: Histogram ($\sqrt[10]{H/N}$ is plotted instead of H) of SUV in PET-CTAC vs. SUV in PET-IAC for a patient. The blue line shows the linear regression, while dashed red line shows $y=x$.)

levels. N is the number of voxels of the data set. The blue line shows the linear regression of the histogram, while dashed red line shows $y=x$ as reference. In the figure and the computation of the regression coefficients, only SUVs of PET-CTAC with SUVs>0.2 were taken into account to exclude the background voxels. This figure shows a similar quantification between PET-IAC and PET-CTAC in general. The linear regression of the histogram results in a relationship of $y=1.06x-0.0007$, with R^2 of 0.975.

4.4 Discussion

This study investigated the feasibility of using PET-NAC as a means for the AC of PET images. Such an approach can be used when CT images are not available for the AC of PET. One potential application of this study is in PET/MR systems since no CT information is available. An iterative segmentation approach is proposed to use PET-NAC images to create an attenuation map. Such approach could segment patient body into three tissue types: background air, soft tissue, and lung using three steps. Previous studies have shown that attenuation map composed of these three tissue types could result in reasonable quantification (<10% error) in PET images (*143*).

The key to the proposed segmentation approach is to segment the body contour from the background air, and to segment the lung region inside the body. The body contour is determined from the active contour model. One contour is needed for each axial slice in the human torso region. However, in the legs region, or head & neck region with arms up, more than one contour has to be performed for each slice. The segmentation of the lung region is rather difficult since the lung boundary is not obvious on PET-NAC especially at the lung-liver and lung-heart interface. In this regard, an

iterative segmentation process was applied to first perform a rough estimate of the lung region and then corrects it for details. One important procedure in STEP 3 of the segmentation procedure is to delineate lung lesions using a threshold of 1.5g/cc and then assign the attenuation coefficient of soft tissue for the lesions. This threshold has been chosen because previous study has shown that assigning the attenuation coefficient of air to lung tissue leads to errors up to 45% (*154*). In this regard, voxels with SUVs >1.5g/cc inside the lung could possibly have a true value of >3g/cc which would potentially be considered to be lung lesions.

PET-NAC is quite noisy and has a low resolution as compared to the CT image, therefore the segmentation could not perform very accurately. Comparing standard attenuation map derived from CT and the attenuation map from our approach (figures 4.5, 4.6 and 4.7), the biggest difference occurs in the delineation of the lung region, particularly in the detailed structures inside the lung and lung-liver and lung-heart interface. However, such difference does not bias the resultant PET-IAC and its quantification very much. The resultant PET-IAC was similar to the standard PET-CTAC as shown in figure 4.6 and 4.7. The SUV values of most of the tumors on PET-IAC are within 10% error as compared to PET-CTAC (tables 4.1, 4.2 and 4.3).

Tables 4.1, 4.2, 4.3 and figure 4.8 all shows that the SUVs from PET-IAC is always slightly higher than the SUVs from PET-CTAC. There are three possible reasons for such results. The first reason is that the segmented body contour is a little larger than the actual body contour derived from CT image. Figure 4.9 shows an axial slice of the patient body size in the head & neck and abdomen region respectively. The black region corresponds to the patient body that is shown in both CT image and from our approach,

while the gray voxels are that included in our approach but excluded from the CT. The results show that our approach tends to overestimate the body size, which will overestimate the attenuation effect and thus excessively correct for the activity concentration, and finally result in higher SUVs in the final PET-IAC as compared to PET-CTAC.

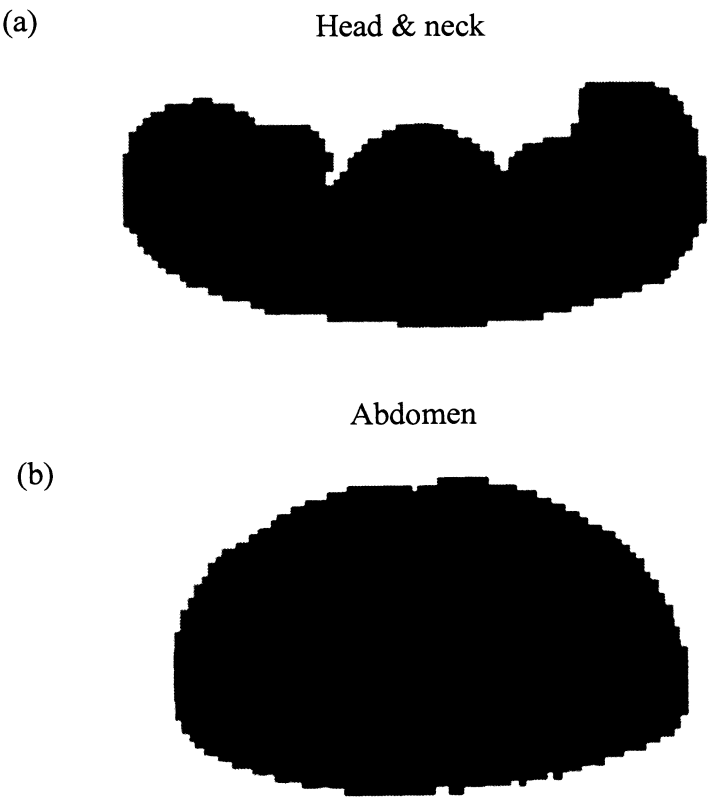

Figure 4.9: Body contour of (a) head & neck, (b) abdomen region; Black region corresponds to the patient body that is shown in both CT image and from our approach, while the gray voxels are that included our approach but exclude from the CT.

The second reason is that a fixed attenuation coefficient of $0.0096cm^{-1}$ is used for all tissues except for the lung region in the final attenuation map. However, CT image

could derive attenuation coefficient ranges from 0.008 to 0.012cm^{-1} for these body tissues. This might result in possible overestimation in the attenuation correction and the corresponding SUV measurement.

The third reason is that CT only captures a single phase of the patient's respiration. Therefore if the patient has lung tumors, CT image shows the tumor size correspond to a single phase. On the other hand, the tumor size in PET image corresponds to all the phases, which is always larger than the size shown on CT. In this regard, our attenuation map displays a larger size of soft tissues corresponds to such tumors than that derived from CT. Such attenuation map increases the resultant tumor SUV since more attenuation correction is performed with respect to CT attenuation map. An example of such case is shown in figure 4.10. Figure 4.10(a) shows a coronal slice of a patient's CT image, and figure 4.10(b) shows the same slice of PET-AC after STEP 2 of the proposed segmentation approach. This figure is the input to STEP 3 whereby heart, liver and lung tumors will be modified to be soft tissue. Comparing the two tumors in arrows between figure 4.10(a) and (b), we can see that these tumors occupy more voxels in figure 4.10(b), probably due to the respiratory motion. In this regard, our approach results in a larger size of these two tumors in the final attenuation map. Finally the SUVs of these two tumors in the PET-IAC are 14% and 17% higher than that shown on the PET-CTAC. However, we consider that our results should be closer to the true value by estimating the tumor size more accurately.

Another potential advantage of our approach is that it could possibly eliminates the "banana artifact" existed in the diaphragm region due to the respiratory motion. Figure 4.11(a) shows a coronal slice of a patient's PET-CTAC, where a banana shaped

light region can be seen above the liver. Such effect is caused by the motion of the

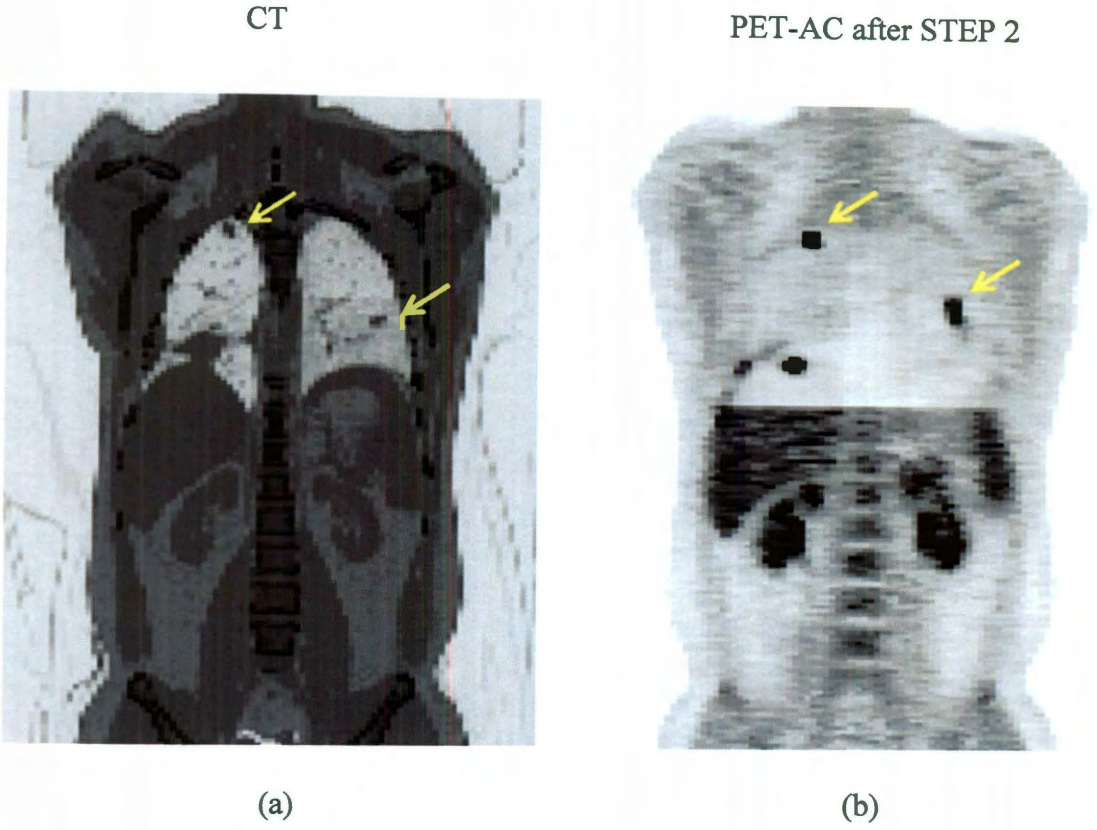

Figure 4.10: A coronal slice of a patient's (a) CT image, (b) PET-AC after STEP 2 of the proposed iterative segmentation approach; showing different sizes of the tumors in arrows.

diaphragm during patient's respiration, which results in the mismatch between PET and CT. Figure 4.11(b) shows the same slice from PET-IAC derived by our approach, which shows an elimination of such artifact.

Histograms comparing SUVs in PET-CTAC to SUVs in PET-IAC (figure 4.8) show that the quantification in PET-IAC is quite accurate. The linear regression of the histogram results in a relationship of $y=1.06x-0.0007$, with R^2 of 0.975. It is very close to the ideal situation (red dashed line in figure 4.8) of $y=x$. For all the 10 patients in this

study, the regression lines on average has the form of $y=(1.07\pm0.07)x+(0.0002\pm0.0011)$, with $R^2=0.98\pm0.008$. This result shows a minor tendency of overestimation in the SUVs in the proposed segmentation approach, and its reasons have been stated above. Overall, SUVs are very close to the reference SUV according to the histogram and the linear regression.

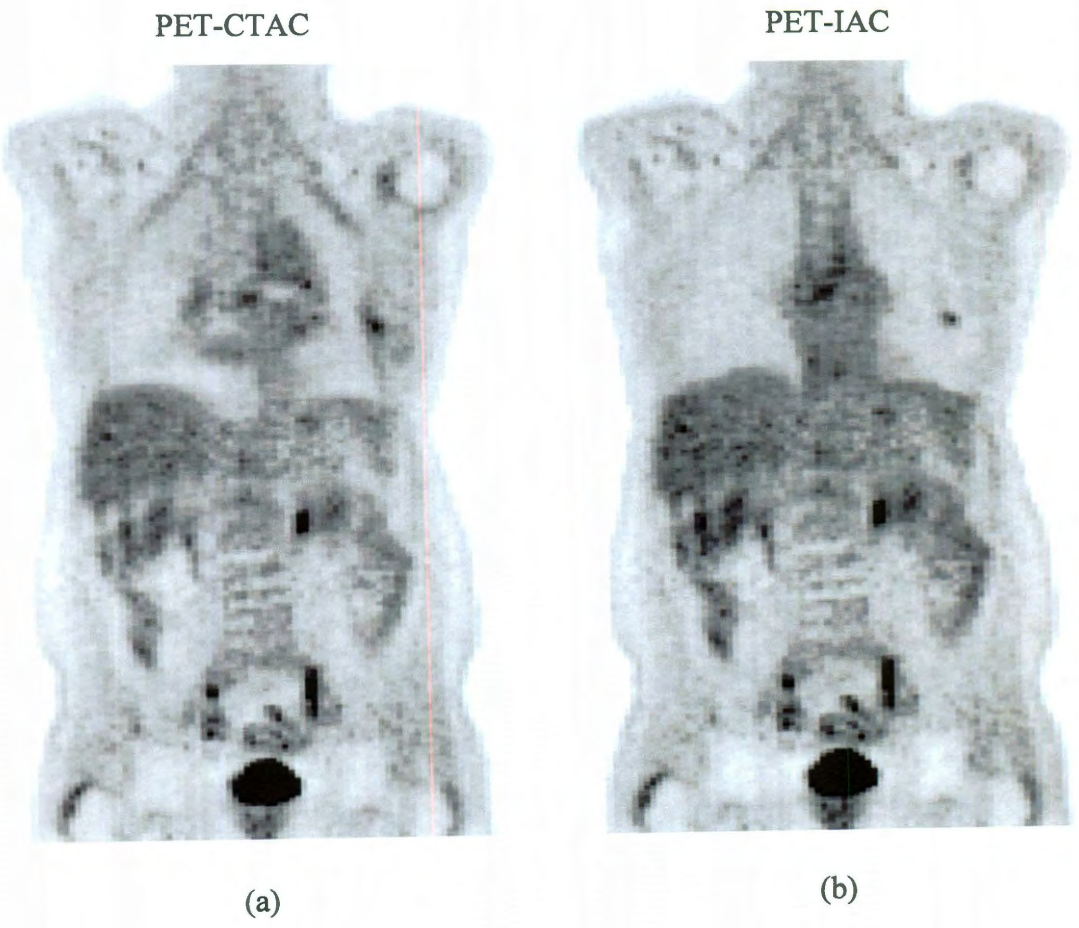

Figure 4.11: A coronal slice of a patient's (a) PET-CTAC, (b) PET-IAC derived by the proposed iterative segmentation approach.

4.5 Conclusion

Preliminary results suggest that the use of PET-NAC as a means for the AC of PET images is feasible in the clinic. Such approach can potentially be an alternative method of MR-based AC in PET/MR imaging.

Chapter 5

Summary and Future Work

5.1 Summary

This thesis focuses on the optimization of three novel developments in positron emission tomography (PET) imaging. The major part of this thesis is composed of three projects (chapter 2-4). Each project evaluated the image quality of one novel development in PET imaging. The three novel developments in PET imaging are as follows:

1. Fully 3D PET data acquisition and reconstruction have recently replaced 2D mode. 3D acquisition provides better detection as compared to 2D since it can accept more events. In addition, it can result in a lower radiation dose to the patient and shorter imaging times. However, this higher sensitivity in 3D comes at the expense of higher scatter and random counts. In addition, there are many more data in a 3D acquisition compared to a 2D acquisition requiring more memory and computational power for image reconstruction. 3D acquisition is followed by 3D data reconstruction. A fully 3D ordered subsets expectation maximization (OSEM) algorithm has recently been developed. This algorithm incorporates corrections for random, scatter and attenuation coincidences within the iterative loop to improve image quality.
2. The development of the time-of-flight (TOF) PET scanner is the state of the art scanner, as compared to conventional PET scanner. A TOF scanner characterizes the location of the annihilation point along the line-of-response (LOR) with a

precise measurement of the difference in arrival times of the two annihilation photons. This localization leads to reduced noise propagation in the reconstruction algorithm. This improvement in image quality is manifest as an increase in the image signal-to-noise ratio (SNR). As the TOF resolution improves, spatial uncertainty decreases and the SNR increases by a larger factor. Furthermore, as the cross section of the imaged object increases, the improvement in SNR also increases by a large factor. This has an important advantage in improved image quality for large patients, since conventional imaging of this patient population yields inferior image quality due to low counting rates or requiring long scanning sessions at the expense of patient comfort.

3. The combination of PET with MR imaging is contemplated as the next step in the evolution of hybrid imaging, following the success of PET/CT imaging currently available. MR imaging shows the advantages over CT because of its high soft tissue contrast and its ability to assess functional parameters and physiological processes (e.g. heart function, blood flow or diffusion and perfusion) without the application of X-ray radiation. A combined PET/MR system can provide both the anatomical and structural description of MR simultaneously with the quantitative capabilities of PET. In addition, such a system would allow exploiting the power of MR spectroscopy to measure the regional biochemical content and to assess the metabolic status or the presence of neoplasia and other diseases in specific tissue areas.

The three major sections in this thesis optimize/investigate the PET image quality for the three novel developments respectively. The primary contributions of these three sections are as follows:

1. An investigation is performed using phantoms to evaluate the relationship between the raw data noise equivalent count rate (NECR) and the image SNR in PET imaging when a fully 3D OSEM reconstruction algorithm is applied. To our knowledge, this relationship has not been previously studied for a fully 3D OSEM reconstruction model. In addition, the effects of the NECR-SNR relationship on patient results is assessed by analyzing patient studies with different body mass index (BMI) and scanner types. In both phantom and patient studies, linear and nonlinear reconstruction methods were used to evaluate this relationship while using various reconstruction parameters. Two different scanner designs were also included to assess the effect of detection efficiency from various detector materials on the NECR and SNR. The relationship between NECR and SNR derived from this investigation can be used to determine the acquisition and reconstruction parameters that could optimize PET image quality.
2. A comprehensive assessment is performed to evaluate PET image quality on a newly developed TOF PET/CT scanner. The investigation first optimizes the iteration numbers for all iterative algorithms available on this scanner: OSEM, +TOF, +point spread function (PSF) and +TOF&PSF (TOFPSF). We believe that such an optimization is necessary to perform a fair comparison of image quality between these algorithms. Following optimizations, the improvement in image quality of advanced algorithms (TOF, PSF, and TOFPSF) with respect to OSEM

is assessed. Finally the effect of scan duration is evaluated to determine whether similar image quality could be obtained using less scan time for advanced algorithms (TOF, PSF, and TOFPSF) as compared to OSEM. Different phantom sizes, sphere sizes and sphere-to-background ratios (SBRs) were used for this comprehensive evaluation. The derived results could be used as guidance for clinical studies on this TOF PET/CT scanner.

3. The feasibility of using the non-attenuated PET images (PET-NAC) as a means for the AC of PET data in the PET/MR systems is investigated. An iterative segmentation approach is proposed. This approach has the ability to segment PET-NAC into three tissue types (background air, soft tissue, and lung) and then assign a predefined attenuation coefficient for each tissue type. Finally an attenuation map is created for PET image reconstruction. This iterative segmentation approach is assessed using both phantom and patient studies. Such an approach can potentially be an alternative method of MR-based AC in PET/MR imaging.

The major results and conclusions of the first project (chapter 2) are as follows:

- A linear correlation is found between the SNR squared and the NECR in 3D-reprojection (RP) reconstruction algorithm. This linear relationship is based on the linear noise propagation of this algorithm.
- The relationship between SNR squared and the NECR is non-linear when using 3D-OSEM reconstruction irrespective of the scanner and reconstruction parameters used.

- The SNR squared and the trues rate is linear when using 3D-OSEM reconstruction, regardless of the choice of scanner and reconstruction parameters.
- The image SNR of the Discovery-RX (DRX) scanner is higher than that of the Discovery-STE (DSTE) scanner when 3D-RP reconstruction was used. When 3D-OSEM reconstruction is used, the two scanners have similar SNRs despite having different NECRs.
- Patient results show that the difference in NECR as well as SNR between the two scanners when using 3D-RP is statistically significant. However, the SNR between the two scanners is not statistically significantly different when using 3D-OSEM. This finding suggests that the SNR may not correlate with the NECR when 3D-OSEM reconstruction is used.
- For clinical PET applications that require high injected ACs (e.g., cardiac imaging), the SNR cannot be predicted by the NECR when using 3D-OSEM reconstruction but should be based on the measured trues count rate. Furthermore, our results suggest that scanners with higher NECRs do not result in better image quality when 3D-OSEM is used.

The major results and conclusions of the second project (chapter 3) are as follows:

- The convergence rate TOF > OSEM > TOFPSF > PSF, and also a faster convergence is achieved for the small phantom compared to larger phantoms.
- The standardized uptake value (SUV) for the TOF reconstruction reaches a slightly higher value than OSEM. PSF can achieve higher values than TOF,

showing a further improvement in quantification. The best results were obtained when TOF and PSF were used together.

- The image noise increment per iteration for PSF/TOFPSF is smaller compared to OSEM/TOF.
- OSEM/PSF requires less than half of the processing time needed for TOF/TOFPSF.
- The improvement in SNR for TOF increases with the increasing phantom sizes. However the improvements in SNR for TOF are relatively similar among different sizes of spheres. For PSF and TOFPSF, the improvement decreases with increasing sphere sizes, since PSF corrects for the partial volume effect, which is more significant for small tumors.
- TOF and PSF have different characteristics in hot and cold contrast recovery coefficient (CRC) respectively. PSF results in more improvement as compared to TOF in hot CRC, while TOF is better in cold CRC.
- TOF results in smallest background noise for small and medium phantoms, while TOFPSF leads to the smallest background noise for large phantom.
- For patients with small and medium sizes, 1 minute TOF, PSF and TOFPSF reconstructions always result in worse SNR while 2 minutes had similar or higher SNR. On the other hand, for very large patient, 1 minute TOF, PSF or TOFPSF data could result in similar SNR to the 3 min OSEM images.
- The difference in CRC between 1 and 2 minutes for each algorithm are small, and suggest that CRC is not sensitive when decreasing acquisition time.

- Our results could be used as guidance for clinical studies on this TOF PET/CT scanner.

The major results and conclusions of the third project (chapter 4) are as follows:

- An iterative segmentation approach is proposed to use PET-NAC images to create an attenuation map. Such approach could segment patient body into three tissue types: background air, soft tissue, and lung using three steps.
- The SUVs from our approach is slightly higher than the SUVs from standard image. The SUV values of most of the tumors on our approach are within 10% error as compared to standard value.
- Our approach could possibly eliminates the "banana artifact" existed in the diaphragm region due to the respiratory motion. Also we consider that our attenuation map estimated the tumor size more accurately.
- Preliminary results suggest that the use of PET-NAC as a means for the AC of PET images is feasible in the clinic. Such approach can potentially be an alternative method of MR-based AC in PET/MR imaging.

5.2 Future Work

The three projects optimize three novel developments in PET imaging. These initial investigations in how PET image quality will be changed under new technologies only provide a first glance or guidance on the manipulation of PET data acquisition and reconstruction. Deeply investigations are required to further optimize or improve PET image quality.

The first project investigated the relationship between NECR and SNR for fully 3D OSEM reconstruction. The phantom and patient studies all acquired on one of the two General Electric PET/CT scanners. However, there are many other PET/CT systems that are currently available from General Electric, as well as from other manufacturers (e.g. Siemens, Phillips, etc.). This relationship needs further examinations on these systems to obtain a more generalized conclusion. In addition, the 3D-OSEM algorithms on these different PET/CT systems are different. This relationship also needs investigations for these different versions of 3D-OSEM algorithms to evaluate its feasibility. Finally, the relationship between true count rate and SNR squared has been found to be linear from experimental studies, which has not been reported previously. This relationship lacks a mathematical demonstration in theory. Further investigation in 3D-OSEM algorithm mathematically may provide such theoretically confirmation in the future.

The second project optimizes the acquisition and reconstruction parameters of a newly developed TOF PET/CT scanner. In the phantom studies, no post filter has been applied on any reconstruction algorithm to preserve the original property of each algorithm. However, in clinical studies, post filters are always applied following iterative reconstruction to decrease image noise and improve image quality, as preferred by physicians for diagnosing. The larger the filter width, the smaller the image noise, but also the worse the image quantification and resolution. In this regard, filter width has to be carefully determined. Currently there is no gold standard of how much filter should be applied on image. The standard filter width is usually determined by human observation. Images applied with different filters are generated and evaluated by several physicians. Physicians then graded each image and finally the one with the highest score is chosen as

the standard clinical protocol. Therefore, investigation in post filter is a very important work in addition to the assessment that has been performed. In the future, different filter widths should be applied on the optimized phantom images, and these images will be graded by several physicians to determine the final filter selection. Furthermore, patient studies have to be performed in the future to validate the results derived from phantom studies.

The third project proposed an iterative segmentation approach to segment PET-NAC into three tissue types, and then generated an attenuation map for AC of PET data. However, PET-NAC is quite noisy and has a low resolution, therefore the segmentation could not be performed very accurately, especially in the detailed structures inside the lung and lung-liver and lung-heart interface. In the future, investigation in better algorithm to segment lung region is warranted. Moreover, ways to segment image into more than 3 tissue types will be an improvement for the current algorithm. Approaches that could combine MR based and PET-NAC based AC may be an interesting topic in the future. Such approach has the ability to include the advantages of both methods and thus provide a more accurate attenuation map. Finally, the implementation problems should be taken into account when applying this technique on future PET/MR hybrid systems. For example, MR hardware and the positioning aids are unavoidable in the PET imaging field-of-view. Such devices could not be seen on PET images and may raise problem if not attenuate corrected properly. More evaluation should be performed on how to generate attenuation maps that also include these devices.

Bibliography

1. Price P. PET as a potential tool for imaging molecular mechanisms of oncology in man. *Trends Mol Med.* 2001;7:442-446.
2. Kumar R, Nadig MR, Chauhan A. Positron emission tomography: clinical applications in oncology. Part 1. *Expert Rev Anticancer Ther.* 2005;5:1079-1094.
3. Kumar R, Chauhan A. Positron emission tomography: clinical applications in oncology. Part 2. *Expert Rev Anticancer Ther.* 2006;6:625-640.
4. Herholz K, Heiss WD. Positron emission tomography in clinical neurology. *Mol Imaging Biol.* 2004;6:239-269.
5. Schwaiger M, Ziegler S, Nekolla SG. PET/CT: challenge for nuclear cardiology. *J Nucl Med.* 2005;46:1664-1678.
6. Bhatnagar A, Hustinx R, Alavi A. Nuclear imaging methods for noninvasive drug monitoring. *Adv Drug Deliv Rev.* 2000;41:41-54.
7. Deans SR. *The radon transform and some of its applications.* New York City, NY: John Wiley & Sons; 1983.
8. Natterer F, Wubbeling F. *Mathematical Methods in Image Reconstruction.* Piladelphia, PA: SIAM: Society for Industrial and Applied Mathematics; 2001.
9. Kauppinen T, Koskinen MO, Alenius S, et al. Improvement of brain perfusion SPECT using iterative reconstruction with scatter and non-uniform attenuation correction. *Eur J Nucl Med.* 2000;27:1380-1386.
10. Etchebehere E, Macapinlac HA, Gonen M, et al. Qualitative and quantitative comparison between images obtained with filtered back projection and iterative

reconstruction in prostate cancer lesions on F-18-FDG PET. *Q J Nucl Med.* 2002;46:122-130.

11. Mesina CT, Boellaard R, Jongbloed G, et al. Experimental evaluation of iterative reconstruction versus filtered back projection for 3D [O-15]water PET activation studies using statistical parametric mapping analysis. *Neuroimage.* 2003;19:1170-1179.
12. Barrett HH, Myers K. Foundations of Image Science. *J Electron Imaging.* 2005;14.
13. Qi J, Leahy RM, Cherry SR, et al. High resolution 3D bayesian image reconstruction using the microPET small animal scanner. *Phys Med Biol.* 1998;43:1001-1013.
14. Qi J, Leahy RM, Hsu C, et al. Fully 3D bayesian image reconstruction for the ECAT EXACT HR+. *IEEE Trans Nucl Sci.* 1998;45:1096-1103.
15. Leahy RM, Qi J. Statistical approaches in quantitative positron emission tomography. *Stat Comput.* 2000;10:147-165.
16. Shepp LA, Vardi Y. Maximum likelihood reconstruction for emission tomography. *IEEE Trans Med Imaging.* 1982;1:113-122.
17. Hudson HM, Larkin RS. Accelerated image reconstruction using ordered subsets of projection data. *IEEE Trans Med Imaging.* 1994;13:601-609.
18. Byrne CL. Convergent block-iterative algorithms for image reconstruction from inconsistent data. *IEEE Trans Image Process.* 1997;6:1296-1304.
19. Byrne CL. Accelerating the EMML algorithm and related iterative algorithms by rescaled block-iterative methods. *IEEE Trans Image Process.* 1998;7:100-109.
20. Herman GT. Image reconstruction from projections: the fundamentals of computerized tomography. New York: Academic Press, 1980.

21. Sercarz JA, Bailet JW, Abemayor E, et al. Computer coregistration of positron emission tomography and magnetic resonance images in head and neck cancer. *Am J Otolaryngol.* 1998;19:130-135.

22. Kinahan PE, Townsend DW, Beyer T, et al. Attenuation correction for a combined 3D PET/CT scanner. *Med Phys.* 1998;25:2046-2053.

23. Hany TF, Steinert HC, Goerres GW, et al. PET diagnostic accuracy: improvement with in-line PET-CT system: initial results. *Radiology.* 2002;225(2):575-581.

24. Israel O, Mor M, Gaitini D, et al. Combined functional and structural evaluation of cancer patients with a hybrid camera-based PET/CT system using F-18-FDG. *J Nucl Med.* 2002;43(9)1129-1136.

25. Cohade C, Osman M, Leal J, et al. Direct comparison of FDG-PET arid PET-CT imaging in colorectal cancer. *J Nucl Med.* 2002;43(suppl 5):78.

26. Freudenberg LS, Antoch G, Mueller SP, et al. Preliminary results of whole-body FDG-PET/CT in lymphoma. *J Nucl Med.* 2002;43(suppl 5):106.

27. Yeung HW, Schoder H, Larson SM. Utility of PET/CT for assessing equivocal PET lesions in oncology—initial experience. *J Nucl Med.* 2002;43(suppl 5):115.

28. Bar-Shalom R, Keidar Z, Guralnik L, et al. Added value of fused PET/CT imaging with FDG in diagnostic imaging and management of cancer patients. *J Nucl Med.* 2002;43(suppl 5):117.

29. Mah K, Caldwell CB, Ung YE, et al. The impact of 18F-FDG-PET on target and critical organs in CT-based treatment planning of patients with poorly defined non-small-cell lung carcinoma: a prospective study. *Int J Radiat Oncol Biol Phys.* 2002;52(2):339-350.

30. Erdi YE, Rosenzweig K, Erdi AK, et al. Radiotherapy treatment planning for patients with non-small-cell lung cancer using positron emission tomography (PET). *Radiother Oncol.* 2002;62:51-60.

31. Mutic S, Grigsby PW, Low DA, et al. PET-guided three-dimensional treatment planning of intracavitary gynecologic implants. *Int J Radiat Oncol Biol Phys.* 2002;52(4):1104-1110.

32. Dizendorf E, Ciernik IF, Baumert B, et al. Impact of integrated PET CT scanning on external beam radiation treatment planning. *J Nucl Med.* 2002;43(suppl 5):118.

33. Keidar Z, Israel O, Krausz Y. SPECT/CT in tumor imaging: Technical aspects and clinical applications. *Semin Nucl Med.* 2003;33:205-218.

34. Gaa J, Rummeny EJ, Seemann MD. Whole-body imaging with PET/MRI. *Eur J Med Res.* 2004;9:309-312.

35. Dahlbom M, Hoffman EJ, Hoh CK, et al. Whole-body positron emission tomography: part I. Methods and performance characteristics. *J Nucl Med.* 1992;33:1191-1199.

36. Derenzo SE, Moses WW. Experimental efforts and results in finding new heavy scintillators. In: Notaristefani FD, LeCoq P, Schneegans M, eds. *Heavy Scintillators for Scientific and Industrial Applications.* Gifsur-Yvette, France: Editions Frontieres; 1993:125-135.

37. Moses WW. Current trends in scintillator detectors and materials. *Nucl Instrum Methods Phys Res A.* 2002;487:123-128.

38. Dahlbom M, Hoffman EJ. An evaluation of a two-dimensional array detector for high resolution PET. *IEEE Trans Med Imaging.* 1988;7:264-272.

39. Cherry SR, Tornai MP, Levin CS, et al. A comparison of PET detector modules employing rectangular and round photomultiplier tubes. *IEEE Trans Nucl Sci.* 1995;42:1064-1068.

40. van Eijk CWE. Inorganic scintillators in medical imaging detectors. *Nucl Instrum Methods Phys Res A.* 2003;509:17-25.

41. Weber MJ, Monchamp RR. Luminescence of $Bi_4Ge_3O_{12}$: spectral and decay properties. *J Appl Phys.* 1973;44:5495.

42. Townsend DW, Wensveen M, Byars LG, et al. A rotating PET scanner using BGO block detectors: design, performance and applications. *J Nucl Med.* 1993;34:1367-1376.

43. Cho ZH, Farukhi MR. Bismuth germanate as a potential scintillation detector in positron cameras. *J Nucl Med.* 1977;18:840-844.

44. Melcher CL, Schweitzer JS. Cerium-doped lutetium oxyorthosilicate: a fast, efficient new scintillator. *IEEE Trans Nucl Sci.* 1992;39:502-505.

45. Pepin CM, Perrot AL, Berard P, et al. Investigation of the properties of new scintillator LYSO and recent LSO scintillators for phoswich PET detectors. *IEEE Nucl Sci Symp Conf Rec.* 2002;2:655-660.

46. Kimble T, Chou M, Chai BHT. Scintillation properties of LYSO crystals. In: Metzler SD, ed. 2002 IEEE Nuclear Science Symposium and Medical Imaging Conference Record [book on CD-ROM]. Norfolk, VA: Institute of Electrical and Electronics Engineers; 2002.

47. Takagi K, Fukazawa T. Cerium-activated Gd_2SiO_5 single crystal scintillator. *App Phys Lett.* 1983;42:43-45.

48. Miles N. Wernick and John N. Aarsvold,"Emission Tomography,"Chapter 10, pp. 179–194, 2004.

49. Townsend DW. Physical principles and technology of clinical PET imaging. *Ann Acad Med Singapore.* 2004;33:133-145.

50. Bendriem B, Trebossen R, Frouin V, et al. A PET scatter correction using simultaneous acquisitions with low and high lower energy thresholds. *IEEE Medical Imaging Conf Rec.* 1993;3:1779-1783.

51. Shao L, Freifelder R, Karp JS. Triple energy window scatter correction technique in PET. *IEEE Trans Med Imaging.* 1994;13:641-648.

52. Grootoonk S, Spinks TJ, Sashin D, Spyrou NM, Jones T. Correction for scatter in 3D brain PET using a dual energy window method. *Phys Med Biol.* 1996;41:2757-2774.

53. Levin CS, Dahlbom M, Hoffman EJ. A Monte Carlo correction for the effect of Compton scattering in 3-D PET brain imaging. *IEEE Trans Nucl Sci.* 1995;42:1181-1185.

54. Ollinger JM. Model based scatter correction for fully 3D PET. *Phys Med Biol.* 1996;41:153-176.

55. Watson CC, Newport D, Casey M, et al. Evaluation of simulation-based scatter correction for 3D PET cardiac imaging. *IEEE Trans Nucl Sci.* 1997;44:90-97.

56. Watson CC. New, faster, image-based scatter correction for 3D PET. *IEEE Trans Nucl Sci.* 2000;47:1587-1594.

57. Hoffman EJ, Huang S-C, Phelps ME, et al. Quantitation in positron emission computed tomography. 4. Effect of accidental coincidences. *J Comput Assist Tomogr.* 1981;5:391– 400.

58. Casey ME, Hoffman EJ. Quantitation in positron emission computed tomography. 7. A technique to reduce noise in accidental coincidence measurements and coincidence efficiency calibration. *J Comput Assist Tomogr.* 1986;10:845– 850.

59. Stearns CW, McDaniel DL, Kohlmyer SG, et al. Random coincidence estimation from single event rates on the Discovery ST PET/CT scanner. *Proceedings of the 2003 IEEE Nuclear Science Symposium and Medical Imaging Conference*. Portland, OR: IEEE. 2003;5:3067–3069.

60. Strother SC, Casey ME, Hoffman EJ. Measuring PET scanner sensitivity: Relating countrates to image signal-to-noise ratios using noise equivalent counts. *IEEE Trans Nucl Sci*. 1990;37:783-788.

61. Bailey DL, Jones T, Spinks TJ, et al. Noise equivalent count measurements in a neuro-PET scanner with retractable septa. *IEEE Trans Med Imaging*. 1991;10:256-260.

62. Stearns CW, Cherry SR, Thompson CJ. NECR analysis of 3D brain PET scanner designs. *IEEE Trans Nucl Sci*. 1995;42:1075-1079.

63. Zasadny KR, Wahl RL. Standardized uptake values of normal tissues at PET with 2-[fluorine-18]-fluoro-2-deoxy-D-glucose: variations with body weight and a method for correction. *Radiology*. 1993;189:847-850.

64. Spinks TJ, Jones T, Bailey DL, et al. Physical performance of a positron tomography for brain imaging with retractable septa. *Phys Med Biol*. 1993;37:1637-1655.

65. Ollinger JM. Model-based scatter correction for fully 3D PET. *Phys Med Biol.* 1996;41:153-176.

66. Kinahan PE, Rogers JG. Analytic 3d image-reconstruction using all detected events. *IEEE Trans Nucl Sci.* 1989;36(1):964-968.

67. Stearns CW, Fessler JA. 3D PET reconstruction with FORE and WLS-OS-EM. *IEEE Nucl Sci Symp Conf Rec.* 2003;2:912-915.

68. Iatrou M, Ross SG, Manjeshwar RM, et al. A fully 3D iterative image reconstruction algorithm incorporating data corrections. *IEEE Nucl Sci Symp Conf Rec.* 2004;4,:2493-2497.

69. Mullani N, Wang W, Hartz P, et al. Sensitivity improvement of TOFPET by the utilization of the inter-slice coincidences. *IEEE Trans Nucl Sci.* 1982;29(1):479-483.

70. Budinger TF. Time-of-flight positron emission tomography: status relative to conventional PET. *J Nucl Med.* 1983;24:73-78.

71. Zaidi H. Is MRI-guided attenuation correction a viable option for dual-modality PET/MR imaging. *Radiology.* 2007;244: 639-642.

72. Hu Z, Ojha N, Renisch S, et al. MR-based attenuation correction for a whole-body sequential PET/MR system. *IEEE Nucl Sci Symp Conf Rec.* 2009; 3508-3512.

73. Schulz V, Torres-Espallardo I, Renisch S, et al. Automatic, three-segment, MR-based attenuation correction for whole-body PET/MR data. *Eur J Nucl Med Mol Imaging* 2011; 38:138-152.

74. Rigo P, Paulis P, Kaschten BJ, et al. Oncological applications of positron emission tomography with fluorine-18 fluorodeoxyglucose. *Eur J Nucl Med.* 1996;23:1641-1674.

75. Demura Y, Tsuchida T, Ishizaki T, et al. ^{18}F-FDG accumulation with PET for differentiation between benign and malignant lesions in the thorax. *J Nucl Med.* 2003;44:540-548.

76. Schöder H, Larson SM, Yeung HWD. PET/CT in oncology: integration into clinical management of lymphoma, melanoma, and gastrointestinal malignancies. *J Nucl Med.* 2004;45(suppl 1):72-81.

77. Gordon BA, Flanagan FL, Dehdashti F. Whole-body positron emission tomography: normal variations, pitfalls, and technical considerations. *Am J Roentgenol.* 1997;169:1675-1680.

78. Strother SC, Casey ME, Hoffman EJ. Measuring PET scanner sensitivity: Relating countrates to image signal-to-noise ratios using noise equivalent counts. *IEEE Trans Nucl Sci.* 1990;37:783-788.

79. Bailey DL, Jones T, Spinks TJ, Gilardi M-C, Townsend DW. Noise equivalent count measurements in a neuro-PET scanner with retractable septa. *IEEE Trans Med Imaging.* 1991;10:256-260.

80. Stearns CW, Cherry SR, Thompson CJ. NECR analysis of 3D brain PET scanner designs. *IEEE Trans Nucl Sci.* 1995;42:1075-1079.

81. Badawi RD, Marsden PK, Cronin BF, Sutcliffe JL, Maisey MN. Optimization of noise-equivalent count rates in 3D PET. *Phys Med Biol.* 1996;41:1755-1776.

82. Surti S, Badawi RD, Holdsworth CH, El Fakhri G, Kinahan PE, Karp JS. A multi-scanner evaluation of PET image quality using phantom studies. *IEEE Nuclear Science Symposium and Medical Imaging Conference.* October 19-25, 2003; Portland, Oregon. IEEE. 2003;4:2425-2427.

83. Lartizien C, Comtat C, Kinahan PE, Ferreira N, Bendriem B, Trebossen R. Optimization of injected dose based on noise equivalent count rates for 2- and 3-dimensional whole-body PET. *J Nucl Med.* 2002;43:1268-1278.

84. Watson CC, Casey ME, Bendriem B, et al. Optimizing injected dose in clinical PET by accurately modeling the counting-rate response functions specific to individual patient scans. *J Nucl Med.* 2005;46:1825-1834.

85. Danna M, Lecchi M, Bettinardi V, et al. Generation of the acquisition-specific NEC (AS-NEC) curves to optimize the injected dose in 3D ^{18}F-FDG whole body PET studies. *IEEE Trans Nucl Sci.* 2006;53:86-92.

86. Kinahan PE, Karp JS. Figures of merit for comparing reconstruction algorithms with a volume-imaging PET scanner. *Phys Med Biol.* 1994;39:631-642.

87. Farquhar TH, Llacer J, Sayre J, Tai YC, Hoffman EJ. ROC and LROC analyses of the effects of lesion contrast, size, and signal-to-noise ratio on detectability in PET images. *J Nucl Med.* 2000;41:745-754.

88. Tong S, Alessio AM, Kinahan PE. Evaluation of noise properties in PSF-based PET image reconstruction. *IEEE Nuclear Science Symposium and Medical Imaging Conference.* October 25-31, 2009; Orlando, Florida. IEEE. 2009:3042-3047.

89. Watson CC. Count rate dependence of local signal-to-noise ratio in positron emission tomography. *IEEE Trans Nucl Sci.* 2004;51:2670-2680.

90. Dahlbom M, Schiepers C, Czernin J. Comparison of noise equivalent count rates and image noise. *IEEE Trans Nucl Sci.* 2005;52:1386-1390.

91. Brasse D, Kinahan PE, Lartizien C, Comtat C, Casey M, Michel C. Correction methods for random coincidences in fully 3D whole-body PET: impact on data and image quality. *J Nucl Med.* 2005;46:859-867.

92. El Fakhri G, Santos PA, Badawi RD, Holdsworth CH, Van Den Abbeele AD, Foley Kijewski M. Impact of acquisition geometry, image processing, and patient size on lesion detection in whole-body ^{18}F-FDG PET. *J Nucl Med.* 2007;48:1951-1960.

93. Wilson JW, Turkington TG, Wilson JM, Colsher JG, Ross SG. Image quality vs. NEC in 2D and 3D PET. *IEEE Nuclear Science Symposium and Medical Imaging Conference.* October 23-29, 2005; Puerto Rico. IEEE. 2005;4:2133-2137.

94. Boellaard R, Van Lingen A, Lammertsma AA. Experimental and clinical evaluation of iterative reconstruction (OSEM) in dynamic PET: quantitative characteristics and effects on kinetic modeling. *J Nucl Med.* 2001;42:808-817.

95. Watson CC. Image noise variance in 3D OSEM reconstruction of clinical time-of-flight PET. *IEEE Nuclear Science Symposium and Medical Imaging Conference.* October 29-November 5, 2006; San Diego, California. IEEE. 2006;3:1736-1739.

96. Walker MD, Matthews JC, Asselin M-C, et al. Optimization of the injected activity in dynamic 3D PET: a generalized approach using patient-specific NECs as demonstrated by a series of ^{15}O-H_2O scans. *J Nucl Med.* 2009;50:1409-1417.

97. Willson DW, Tsui BMW, Barrett HH. Noise properties of the EM algorithm II: Monte Carlo simulations. *Phys Med Biol.* 1994;39: 847-871.

98. Qi J. A unified noise analysis for iterative image estimation. *Phys Med Biol.* 2003;48: 3505-3519.

99. Badawi RD, Dahlbom M. NEC: some coincidences are more equivalent than others. *J Nucl Med.* 2005;46:1767-1768.

100. Muller JW. Dead-time problems. *Nucl Instrum Methods.* 1973;112:47-57.

101. Badawi RD, Domigan P, Johnson O, et al. Count-rate dependent event mispositioning and NEC in PET. *IEEE Trans Nucl Sci.* 2004;51:41-45.

102. Kinahan P, Vesselle H, Williams J, et al. Performance evaluation of an integrated PET/CT scanner: Discovery STE. *J Nucl Med.* 2006;47(suppl 1):392P.

103. Kemp BJ, Kim C, Williams JJ, Ganin A, Lowe VJ. NEMA NU 2-2001 performance measurements of an LYSO-based PET/CT system in 2D and 3D acquisition modes. *J Nucl Med.* 2006;47:1960-1967.

104. Iatrou M, Ross SG, Manjeshwar RM, Stearns CW. A fully 3D iterative image reconstruction algorithm incorporating data corrections. *IEEE Nuclear Science Symposium and Medical Imaging Conference.* October 16-22, 2004; Italy. IEEE. 2004;4:2493-2497.

105. Barrett HH, Willson DW, Tsui BMW. Noise properties of the EM algorithm I: Theory. *Phys Med Biol.* 1994;39:833-846.

106. Soares EJ, Byrne CL, Glick SJ. Noise characterization of block-iterative reconstruction algorithms: I. Theory. *IEEE Trans Med Imaging.* 2000;19:261-270.

107. Cherry SR, Sorenson JA, Phelps ME. *Physics in Nuclear Medicine*, 3rd ed. Saunders, Pennsylvania, 2003, 131-148.

108. Chang T, Chang G, Kohlmyer S, Clark JW, Rohren E, Mawlawi OR. Effects of injected dose, BMI and scanner type on NECR and image noise in PET imaging. *Phys Med Biol.* 2011;56:5275-5285.

109. Anger HO. Survey of radioisotope cameras. *ISA Trans.* 1966;5:311-334.

110. Allemand R, Gresset C, Vacher J. Potential advantages of a cesium fluoride scintillator for a time-of-flight positron camera. *J Nucl Med.* 1980;21:153-155.

111. Ter-Pogossian MM, Mullani NA, Ficke DC, Markham J, Snyder DL. Photon time-of-flight-assisted positron emission tomography. *J Comput Assist Tomogr.* 1981;5:227-239.

112. Wong WH, Mullani NA, Wardworth G, Hartz RK, Bristow D. Characteristics of small barium fluoride (BaF_2) scintillator for high intrinsic resolution time-of-flight positron emission tomography. *IEEE Trans Nucl Sci.* 1984;31:381-386.

113. Moses WW, Derenze SE. Prospects for time-of-flight PET using LSO scintillator. *IEEE Trans Nucl Sci.* 1999;46:474-478.

114. Kimble T, Chou M, Chai BHT. Scintillation properties of LYSO crystals. *IEEE Nucl Sci Symp Conf Rec.* 2002;3:1434-1437.

115. Surti S, Karp JS, Muehllehner G, Raby PS. Investigation of lanthanum scintillators for 3-D PET. *IEEE Trans Nucl Sci.* 2003;50:348-354.

116. Surti S, Kuhn A, Werner ME, Perkins AE, Kolthammer J, Karp JS. Performance of Philips Gemini TF PET/CT scanner with special consideration for its time-of-flight imaging capabilities. *J Nucl Med.* 2007;48:471-480.

117. Jakoby BW, Bercier Y, Conti M, et al. Performance investigation of a time-of-flight PET/CT scanner. *IEEE Nucl Sci Symp Conf Rec.* 2008;3738-3743.

118. Kemp B, Williams J, Ruter R, Lowe V, Mullan B. Performance measurements of a whole body PET/CT system with time-of-flight capability. *J Nucl Med.* 2009;50(suppl 2):1546P.

119. Tomitani T. Image-reconstruction and noise evaluation in photon time-of-flight PET. *IEEE Trans Nucl Sci.* 1981;28:4581-4589.

120. Watson CC. An evaluation of image noise variance for time-of-flight PET. *IEEE Trans Nucl Sci.* 2007;54:1639-1647.

121. Karp JS, Surti S, Daube-Witherspoon ME, Muehllehner G. Benefit of time-of-flight in PET: experimental and clinical results. *J Nucl Med.* 2008;49:462-470.

122. Wilson JM, Turkington TG. TOF-PET small-lesion image quality measured over a range of phantom sizes. *IEEE Nucl Sci Symp Conf Rec.* 2009;3710-3714.

123. El Fakhri G, Surti S, Trott CM, Scheuermann J, Karp JS. Improvement in lesion detection with whole-body oncologic time-of-flight PET. *J Nucl Med.* 2011;52:347-353.

124. Surti S, El Fakhri G, Karp JS. Optimizing acquisition parameters in TOF PET scanners. *IEEE Nucl Sci Symp Conf Rec.* 2006;2354-2359.

125. Surti S, Karp JS. Experimental evaluation of a simple lesion detection task with time-of-flight PET. *Phys Med Biol.* 2009;54:373-384.

126. Surti S, Karp JS. Application of a generalized scan statistic model to evaluate TOF PET images. *IEEE Trans Nucl Sci.* 2011;58:99-104.

127. Lois C, Jakoby BW, Long MJ, et al. An assessment of the impact of incorporating time-of-flight information into clinical PET/CT imaging. *J Nucl Med.* 2010;51:237-245.

128. Jakoby BW, Bercier Y, Conti M, Casey ME, Bendriem B, Townsend DW. Physical and clinical performance of the mCT time-of-flight PET/CT scanner. *Phys Med Biol.* 2011;56:2375-2389.

129. Bettinardi V, Presotto L, Rapisarda E, Picchio M, Gianolli L, Gilardi MC. Physical performance of the new hybrid PET/CT discovery-690. *Med Phys.* 2011;38:5394-5411.

130. Kadrmas DJ, Casey ME, Conti M, Jakoby BW, Lois C, Townsend DW. Impact of time-of-flight on PET tumor detection. *J Nucl Med.* 2009;50:1315-1323.

131. Budinger TF. Time-of-flight positron emission tomography: status relative to conventional PET. *J Nucl Med.* 1983;24:73-78.

132. Rigo P, Paulis P, Kaschten BJ, et al. Oncological applications of positron emission tomography with fluorine-18 fluorodeoxyglucose. *Eur J Nucl Med.* 1996; 23:1641-1674.

133. Demura Y, Tsuchida T, Ishizaki T, et al. ^{18}F-FDG accumulation with PET for differentiation between benign and malignant lesions in the thorax. *J Nucl Med.* 2003; 44:540-548.

134. Schöder H, Larson SM, Yeung HWD. PET/CT in oncology: integration into clinical management of lymphoma, melanoma, and gastrointestinal malignancies. *J Nucl Med.* 2004; 45:72S-81S.

135. Lodge MA, Lucas JD, Marsden PK, Cronin BF, O'Doherty MJ, Smith MA. A PET study of 18 FDG uptake in soft tissue masses. *Eur J Nucl Med Mol Imag.* 1999; 26:22-23.

136. Kostakoglu L, Goldsmith SJ. 18F-FDG PET evaluation of the response to therapy for lymphoma and for breast, lung, and colorectal carcinoma. *J Nucl Med.* 2003; 44:224-239.

137. Huang SC, Phelps ME, Hoffman EJ, Sideris K, Selin CJ, Kuhl DE. Noninvasive determination of local cerebral metabolic rate of glucose in man. *Am J Physiol*. 1980; 238:E69-E82.

138. Kinahan P, Townsend D, Beyer T, Sashin D. Attenuation correction for a combined 3D PET/CT scanner. *Med Phys*. 1998; 25:2046-2053.

139. Bai C, Shao L, Da Silva AJ, Zhao Z. A generalized model for the conversion from CT numbers to linear attenuation coefficients. *IEEE Trans Nucl Sci*. 2003; 50:1510-1515.

140. Catana C, Wu Y, Judenhofer MS, Qi J, Pichler BJ, Cherry SR. Simultaneous acquisition of multislice PET and MR images: initial results with a MR-compatible PET scanner. *J Nucl Med*. 2006; 47:1968-1976.

141. Schlemmer HP, Pichler B, Schmand M, et al. Simultaneous MR/PET imaging of the human brain: feasibility study. *Radiology*. 2008; 248:1028-1035.

142. Steinberg J, Jia G, Sammet S, Zhang J, Hall N, Knopp MV. Three-region MRI-based whole-body attenuation correction for automated PET reconstruction. *Nucl Med Biol*. 2010; 37:227-235.

143. Schulz V, Torres-Espallardo I, Renisch S, et al. Automatic, three-segment, MR-based attenuation correction for whole-body PET/MR data. *Eur J Nucl Med Mol Imaging*. 2011; 38:138-152.

144. Hofmann M, Steinke F, Scheel V, et al. MRI-based attenuation correction for PET/MRI: a novel approach combining pattern recognition and atlas registration. *J Nucl Med*. 2008; 49:1875-1883.

145. Delso G, Martinez-Moller A, Bundschuh RA, et al. Evaluation of the attenuation properties of MR equipment for its use in a whole-body PET/MR scanner. *Phys Med Biol.* 2010; 55:4361-4374.

146. Mantlik F, Hofmann M, Werner MK, et al. The effect of patient positioning aids on PET quantification in PET/MR imaging. *Eur J Nucl Med Mol Imaging.* 2011; 38:920-929.

147. Delso G, Martinez-Moller A, Bundschuh RA, Nekolla SG, Ziegler SI. The effect of limited MR field of view in MR/PET attenuation correction. *Med Phys.* 2010; 37:2804-2812.

148. Michel C, Bol A, De Volder AG, Goffinet AM. Online brain attenuation correction in PET: towards a fully automated data handling in a clinical environment. *Eur J Nucl Med.* 1989; 15:712-718.

149. Nuyts J, Dupont P, Stroobants S, Benninck R, Mortelmans L, Suetens P. Simultaneous maximum a-posteriori reconstruction of attenuation and activity distributions from emission sinograms. *IEEE Trans Med Imaging.* 1999; 18:393-403.

150. Kass M, Witkin A, Terzopoulos D. Snakes: active contour models. *Int J Comput Vision.* 1988; 321-331.

151. Xu M, Cutler PD, Luk WK. Adaptive, segmented attenuation correction for whole-body PET imaging. *IEEE Trans Nucl Sci.* 1996; 43:331-336.

152. Haralick RM, Shapiro LG. Image segmentation techniques. *Comput Vis Graph Image Proc.* 1985; 29:100-132.

153. Kemp BJ, Kim C, Williams JJ, Ganin A, Lowe VJ. NEMA NU 2-2001 performance measurements of an LYSO-based PET/CT system in 2D and 3D acquisition modes. *J Nucl Med.* 2006; 47:1960-1967.

154. Keereman V, Van Holen R, Mollet P, Vandenberghe S. The effect of errors in segmented attenuation maps on PET quantification. *Med Phys*. 2011; 38:6010-6019.